SANDIA REPORT
SAND2009-8050
Unlimited Release
Printed December, 2009

GEOPHYSICAL REMOTE SENSING OF WATER RESERVOIRS SUITABLE FOR DESALINIZATION

Lewis C. Bartel, David F. Aldridge, Bruce P. Engler, and Nedra Bonal

Prepared by
Sandia National Laboratories
Albuquerque, New Mexico 87185 and Livermore, California 94550

Sandia is a multiprogram laboratory operated by Sandia Corporation,
a Lockheed Martin Company, for the United States Department of Energy's
National Nuclear Security Administration under Contract DE-AC04-94AL85000.

Approved for public release; further dissemination unlimited.

Sandia National Laboratories

Issued by Sandia National Laboratories, operated for the United States Department of Energy by Sandia Corporation.

NOTICE: This report was prepared as an account of work sponsored by an agency of the United States Government. Neither the United States Government, nor any agency thereof, nor any of their employees, nor any of their contractors, subcontractors, or their employees, make any warranty, express or implied, or assume any legal liability or responsibility for the accuracy, completeness, or usefulness of any information, apparatus, product, or process disclosed, or represent that its use would not infringe privately owned rights. Reference herein to any specific commercial product, process, or service by trade name, trademark, manufacturer, or otherwise, does not necessarily constitute or imply its endorsement, recommendation, or favoring by the United States Government, any agency thereof, or any of their contractors or subcontractors. The views and opinions expressed herein do not necessarily state or reflect those of the United States Government, any agency thereof, or any of their contractors.

Printed in the United States of America. This report has been reproduced directly from the best available copy.

Available to DOE and DOE contractors from
U.S. Department of Energy
Office of Scientific and Technical Information
P.O. Box 62
Oak Ridge, TN 37831

Telephone: (865) 576-8401
Facsimile: (865) 576-5728
E-Mail: reports@adonis.osti.gov
Online ordering: http://www.osti.gov/bridge

Available to the public from
U.S. Department of Commerce
National Technical Information Service
5285 Port Royal Rd.
Springfield, VA 22161

Telephone: (800) 553-6847
Facsimile: (703) 605-6900
E-Mail: orders@ntis.fedworld.gov
Online order: http://www.ntis.gov/help/ordermethods.asp?loc=7-4-0#online

SAND2009-8050
Unlimited Release
Printed December, 2009

Geophysical remote sensing of water reservoirs suitable for desalination

Bartel, L. C., Aldridge, D.F., Engler, B. P., and Bonal, N.
Geophysics Department 6734
Sandia National Laboratories
Albuquerque, NM

Abstract

In many parts of the United States, as well as other regions of the world, competing demands for fresh water or water suitable for desalination are outstripping sustainable supplies. In these areas, new water supplies are necessary to sustain economic development and agricultural uses, as well as support expanding populations, particularly in the Southwestern United States. Increasing the supply of water will more than likely come through desalinization of water reservoirs that are not suitable for present use. Surface-deployed seismic and electromagnetic (EM) methods have the potential for addressing these critical issues within large volumes of an aquifer at a lower cost than drilling and sampling. However, for detailed analysis of the water quality, some sampling utilizing boreholes would be required with geophysical methods being employed to extrapolate these sampled results to non-sampled regions of the aquifer. The research in this report addresses using seismic and EM methods in two complimentary ways to aid in the identification of water reservoirs that are suitable for desalinization. The first method uses the seismic data to constrain the earth structure so that detailed EM modeling can estimate the pore water conductivity, and hence the salinity. The second method utilizes the coupling of seismic and EM waves through the seismo-electric (conversion of seismic energy to electrical energy) and the electro-seismic (conversion of electrical energy to seismic energy) to estimate the salinity of the target aquifer. Analytic 1D solutions to coupled pressure and electric wave propagation demonstrate the types of waves one expects when using a seismic or electric source. A 2D seismo-electric/electro-sesismic is developed to demonstrate the coupled seismic and EM system. For finite-difference modeling, the seismic and EM wave propagation algorithms are on different spatial and temporal scales. We present a method to solve multiple, finite-difference physics problems that has application beyond the present use. A limited field experiment was conducted to assess the seismo-electric effect. Due to a variety of problems, the observation of the electric field due to a seismic source is not definitive.

ACKNOWLEDGEMENTS

The authors wish to thank Gregory J. Elbring for his support and encouragement of this work. We wish also to thank the LDRD program for providing the funds for this research.

Contents

1.0 Introduction …… 5
2.0 Electromagnetic and Seismic Data **……** **7**
3.0 Seismic and EM Interactions ……. 16
3.1 Introduction to Electrokinetics …… 16
3.2 EDL Model-First Order 19
4.0 1D Coupled Pressure and EM Waves – Seismoelectric Wave Propagation …….. 23
5.0 2D Seismo-Electric and Electro-Seismic Algorithm …… 29
5.1 Determination of Time Step – 1D Solutions …….. 29
5.2 2D Seismo-Electric and Electro-Seismic **……** 33
5.2.1 Governing Equations …… 33
5,2,2 Finite-Difference Solutions …….. 38
5.2.3 Electrical Conductivity Model Building …… 45
5.2.4 2D Numerical Simulations ……. 49
6.0 Field Experiment …… 55
6.1 Site Description: Geology, Aquifer, and Surface Conditions ……. 55
6.2 Field Acquisition …….. 59
6.3 Seismic and EM Data for Seismo-Electric Study ……. 64
6.4 Seismic Tomography Results for the Tijeras Canyon Site …… 69
7.0 Conclusions …….. 70
References …… 72
Appendix A Coupled Pressure and EM Waves – Seismoelectric Wave Propagation …. 74
Appendix B Analytic Solutions for 1D Plane Waves …….. 84
Appendix C Air-Earth Interface in EM Modeling …… 89
Appendix D Field Notes …… 99
Appendix E Weather Data …… 103
Appendix F GPS Coordinates of Source and Sensor Location for Field Experiment .. 118
Distribution …… 126

Page intentionally left blank

1.0 Introduction

In many parts of the United States and multiple regions of the world, competing demands for fresh water or water suitable for desalination are outstripping sustainable supplies. In these areas, new water supplies are necessary to sustain economic development and agricultural uses, as well as support expanding populations, particularly in the Southwestern United States. One of the primary objectives of the Sandia Water Initiative is to maintain and increase the sustainability of water through creation of new water supplies. New water supplies will more than likely come from water suitable for desalination. Creating usable new water through desalination requires identifying groundwater reservoirs appropriate for desalination. Many factors, including salinity and the pH of the water, affect the water quality. There are many economically valuable New Mexico hydrological reservoirs (*e. g*., in the Tularosa Basin) where the absolute level and spatial distribution of fluid salinity are not well established. Salinity will vary within the reservoir: grading from potable water, to water appropriate for agricultural use only, to water requiring desalinization, to water too saline for economic treatment. Critical issues for managing a desalination water supply are: resource characterization, monitoring production and recharge, and identification of waste-disposal formations. Surface-deployed seismic and electromagnetic (EM) methods have the potential for addressing these critical issues within large volumes of an aquifer at a lower cost than drilling and sampling. However, for detailed analysis of the water quality, some sampling utilizing boreholes would be required with geophysical methods being employed to extrapolate these sampled results to non-sampled regions of the aquifer. Surface-deployed geophysical methods are key technologies that provide necessary information for efficient and sustainable extraction, risk assessment of the withdrawal and injection of waste products, and monitoring the health of an aquifer.

The research in this LDRD addressed two complimentary ways to utilize seismic and EM methods. The first technique uses the seismic data to constrain the geologic structure for interpretation of the EM data, and then performs a joint interpretation of all the data for electrical conductivity, porosity, and hydraulic permeability. The EM response of the aquifer is driven by a complex interaction between the pore water (ionic) conductivity, the geometry and tortuosity of the pore spaces and the lithology of the rock matrix (Pride, 1994). For pore water salinities ranging from 100 to 2000 ppm of NaCl, the pore water conductivity ranges from 0.017 to 0.29 *S*/*m*. Depending upon the characteristics of the aquifer, this could mean a change in the apparent conductivity (that inferred from surface measurements) of the aquifer by an order of magnitude. Near-surface conductivity variations in this range are easily detectable with modern EM mapping technology. Katz and Thompson (1986) have shown a direct relationship between the hydraulic permeability and the ratio of the apparent conductivity to the pore water conductivity. Bartel (1990) used their work, along with borehole data, to infer the transmissivity of the Culebra aquifer at the WIPP site using surface-acquired EM data. For the second, more high-risk, component of this research we intend to utilize the seismo-electric (SE) and/or the electro-seismic (ES) effect. These techniques have not been commonly tried for water quality assessment but, have the potential to provide a better measure of the salinity

and pH of the target water supply (particularly in the low *ppm* ranges of NaCl). When combined with the first method, the assessment of the salinity has a high probability of success for determining the economic utility of the aquifer.

The SE effect converts seismic wave propagation energy to electric field energy by displacing the ion-carrying fluid with respect to the solid matrix resulting in an electrical field. The magnitude of this seismic induced electric field depends on the electrochemical properties of the fluid-solid contact and the mobility of the pore fluid. The ES effect, which also depends on the same properties as the SE effect, converts electric field energy to seismic energy by creating fluid flow leading to a pressure gradient resulting in a seismic wave. When the appropriate coefficients leading to the two effects obey the Onsager reciprocity theorem, they are equal (*e. g*., Pride, 1994). Both the SE and ES methods depend upon the electrokinetics of the pore fluid and host rock. However, there is some recent experimental evidence (Thompson and Gist, 1991 and 1993, Thompson, 2005; Deckman, *et al*., 2005) that the coupling coefficients of the SE and ES effects do not obey the Onsager reciprocity theorem and in fact there is a second-order effect for the ES coupling coefficient, which has proved useful for hydrocarbon detection.

The coupling between the pressure gradient and electrical current or between the electric field and the fluid flow (when the Onsager reciprocity theorem is satisfied) depends directly upon the zeta potential (*e.g*., Pride, 1994). In electrokinetics, the zeta potential is defined as the electric potential at the shear plane that separates the immobile ions from the mobile ions and governs the behavior and magnitude of the SE and ES effect through the dependence on the electrolyte concentration and pH. The zeta potential varies from mineral to mineral as a function of pH, ionic strength, and fluid composition. In geologic situations it is generally negative, becoming more negative at high pH, but decreasing in absolute magnitude with increasing salinity (*e.g.*, Lorne, *et al*., 1999).

This report will be divided into several sections or topics. In Section 2.0, the combination of seismic and EM simulated data will be discussed for two different earth models. We will use reverse-time migration (*e.g*., see, Bartel, *et al*., 2008) to analyze the seimic data and use apparent resistivity to analyze EM data. Seismic and EM interactions due to the electric double layer will be discussed in Section 3.0 where a simple Gouy-Chapman theory will be presented. In order to understand the types of waves that result from the SE and ES effects, a one-dimensional analytic solution to the seismic-EM coupling will be given in Section 4.0. In Section 5.0, a 2D seismo-electric/electro-seismic algorithm will be developed. Generally for finite-difference solutions, the spatial and temporal scales are quite different for seismic and EM simulations. In this section we present our method of interpolating between the two types of physical phenomena. Preliminary to the development of an algorithm, stability of the EM portion of the algorithm will be discussed and a 1D model to decide upon an appropriate time-step for the EM calculations is given. A small-scale field test was conducted as a part of this research, and the test and results will be discussed in Section 6.0. Our conclusions and future directions of any further research are in Section 7.0.

2.0 Electromagnetic and Seismic Data

In this section, we will show how seismic and EM data provide information on porosity and salinity. To illustrate imaging a layer with variable properties within the layer, consider the earth model shown in Figure 2.1. The wave speeds were calculated using effective Lamé parameters for fluid filled pores where there is no relative motion between the solid and fluid as described in Appendix C of Bartel, *et al.*, (2008). The effective Lamé parameters $(\lambda_{effective}\mu_{effective})$ are

$$\begin{aligned} \lambda_{effective} &= (1-\phi)\lambda + \phi K^f \\ \mu_{effective} &= (1-\phi)\mu \end{aligned} , \tag{2.1}$$

and for the mass density we used

$$\rho_{effective} = (1-\phi)\rho^s + \phi\rho^f , \tag{2.2}$$

where ϕ is the porosity, K^f is the bulk modulus of the fluid, and ρ^s and ρ^f are the mass densities of the solid and fluid, respectively. The wave speeds were calculated using equation

$$\begin{aligned} V_p &= \sqrt{\frac{\lambda_{effective} + 2\mu_{effectuve}}{\rho_{effectuve}}} \\ V_s &= \sqrt{\frac{\mu_{effective}}{\rho_{effective}}} \end{aligned} \tag{2.3}$$

The parameters λ and μ were determined from the wave speeds and mass density of the surrounding medium, which is assumed to have minimal porosity. The effects of the changes in porosity on wave speed and mass density are evident in Figure 2.1. It is noteworthy that in Bartel, *et al*., (2008) using the Voigt limit (*cf*., Han and Batzle, 2004) for the dry frame bulk modulus coupled with Gassmann's equation (*cf*., Wang, *et al*., 1998; Han and Batzle, 2004) is equivalent to our derivation of the effective medium parameters. This suggests that there is no relative motion between the solid and fluid when using the Voigt limit in Gassmann's equation.

Two sets of forward numerical simulations were performed, one with the 20 percent porosity slab and one without the 20 percent porosity slab in the 5 percent porosity layer. The background model used for direct arrival subtraction in the reverse-time migration (RTM) (*e. g*., see, Bartel, *et.al*., 2008) method included the shallow layer to a depth of 100 *m* and a basal layer but does not include the variable porosity layer at 280-300 *m*. This background model eliminates direct arrivals, surface waves, head waves, and reflections from the layer at a depth of 100 *m*.

To image the subsurface, the RTM method utilizes the wavefields that are generated by a seismic source and captured by a set of receivers. The measured responses at the receivers consist of direct arrival responses and reflected and/or scattered responses. The traces measured by the receivers are time-reversed and these time-reversed traces are the input waveforms for the receivers acting as sources in a numerical simulation. For example, if the receivers are vertical particle motion geophones, the receivers acting as sources are vertical force sources; if the receivers are pressure receivers, the receivers acting as sources are explosion sources. However, before the traces are time-reversed and played back into the background model, the direct arrivals are generally removed so that only the reflected and/or scattered waves are used for the RTM input waveforms. These time-reversed trace input waveforms applied to the receivers acting as sources produce a time-reversed wavefield that propagates into the background model. A critical part of the RTM process is an imaging condition; *i.e.*, a methodology to produce an image using the time-reversed wavefield. One imaging condition is to take the zero-lag cross-correlation between the time-reversed wavefield emanating from the receivers acting as sources with the source wavefield collapsing onto the source. (Note that one could just as well cross-correlate a collapsing time-reversed wavefield with an expanding source wavefield.) These two wavefields are like two ships passing in the night and have a maximum in the zero-lag cross-correlation when these two wavefields (two ships) are coincident at the reflection or scattering point in time and hence depth. To apply the RTM process requires a background velocity model for the computation of the time-reversed wavefield and the source wavefield; therefore, the image is only as good as the background velocity model. Generally, a uniform or smoothly varying model of wave speeds and mass density is used. In order for the image to be independent of the trace length, the zero-lag cross-correlation of the expanding (or collapsing) time-reversed wavefield with the collapsing (or expanding) source wavefield is the correct procedure.

For the seismic calculations, vertical geophone receivers (buried 1 *m*) were located starting at -300 *m* to 300 *m* in 5 *m* increments for a total of 121 receivers. The vertical body force sources (buried 1 *m*) started at -300 *m* to 300 *m* in 50 *m* increments for a total of 13 sources. (To minimize the number of source calculations, symmetry of the problem was utilized.) The sources and receivers were on a line to simulate a 2D seismic survey. The parallel version of the elastic code was used for the calculations with the built-in Ricker wavelet and executed on the Sandia's Thunderbird parallel computer. The center frequency of the Ricker wavelet used was 25 *Hz*.

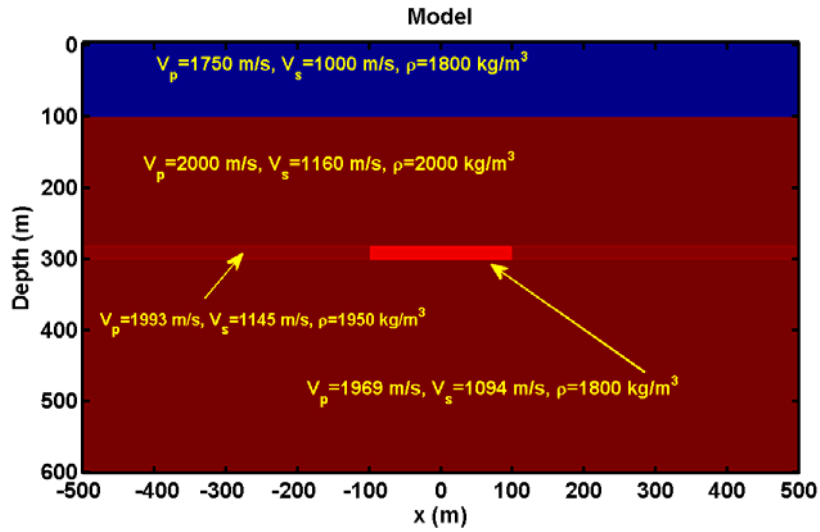

Figure 2.1: Earth model for a 20 *m* thick layer of variable porosity. Shown is a 200 *m* wide 20 percent porosity slab (infinite in the *y*-direction) within a 5 percent porosity layer

Figure 2.2 shows amplitude vs offset (AVO) for the 20 percent porosity slab within the 5 percent porosity layer and when there is only the 5 percent porosity layer. The same plot scale was used for the two AVO figures. The background responses have been removed. The source is located at -300 *m*. The long offset *P-P*, *P-S*, *S-P* and *S-S* reflections show larger amplitudes for the presence of the 20 percent porosity slab than when it is absent. Also note the reflection from the edge of the slab apparent for geophone distance $\sim -300\,m$ to $\sim -200\,m$ and time $\sim 900-1000\,ms$. Although AVO is evident in Figure 2.2, the AVO effects will not be pursued in this report.

The zero-lag cross-correlation RTM images for the 20 percent porosity slab within the 5 percent porosity layer and for only the 5 percent porosity layer are shown in Figure 2.3. Here the expanding time-reversed wavefields were cross-correlated with the collapsing source field. The time-reversed signals with the background response removed were "played back" into the background model, which excludes the porous slab and layer. Each image shown in Figure 2.3 is a composite image from all 13 sources. From an examination of the figure, the 20 percent porosity slab is clearly discernable from the 5 percent layer background. In both figures, there are migration artifacts in the upper 200 *m*. Even for small changes in the wave speeds and the mass density for the 5 percent porosity layer, the RTM method clearly images that layer. Both the images shown in Figure 2.3 were plotted using the same color scale.

In general, the hydraulic permeability and porosity are not independent, however the exact the relationship between porosity and permeability is formation dependent. From work done by Malaver (2004) on the Queen sand formation for a CO_2 sequestration experiment near Hobbs, NM, the statistical relationship between the porosity, x (in percent), and the log of the permeability, y, is

$$y = 0.241x - 2.682$$
$$k = 10^{y} \ \ md \tag{2.4}$$

where k is the permeability and *md* is millidarcies. Note, 1 darcy is equivalent to 9.869233×10^{-13} m^2.

Using the above relationship as a guide, a 20 percent porosity would correspond to a permeability of 137 *md* and a porosity of 5 percent would correspond to a permeability of 0.03 *md*. The results of this numerical RTM simulation are encouraging that seismic surveys can yield useful information about the porosity and permeability of a relative thin layer. The amplitude of the spatial wavelet, due to the cross-correlation, is proportional to the reflection coefficient (Bartel, *et al*., 2008). The ratio of the spatial wavelet for the 20 percent porosity to that of the 5 percent porosity is the same as the ratio of the reflection coefficients calculated using

$$R_{sn} \approx \frac{Z_2 - Z_1}{Z_2 + Z_1}\ , \qquad Z = \rho\alpha \tag{2.5}$$

where ρ is the mass density and α is the P-wave speed.

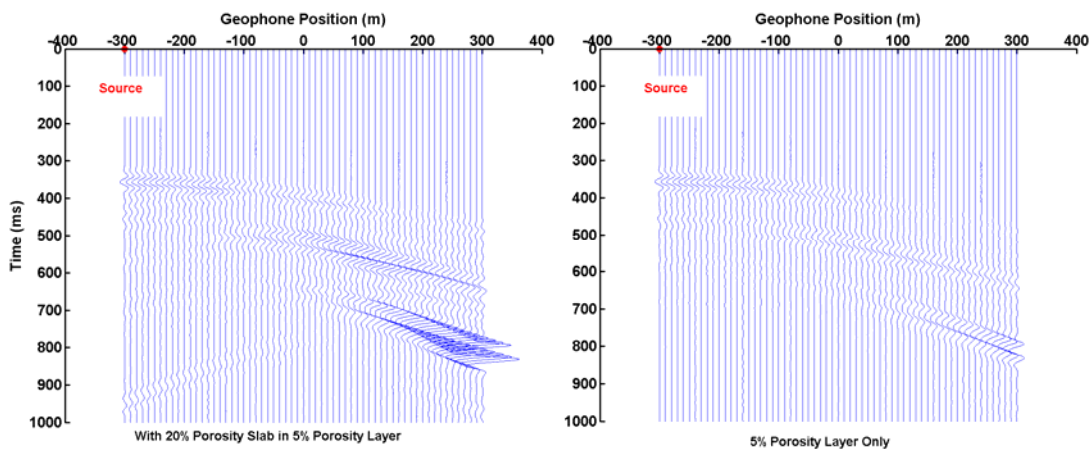

Figure 2.2: Amplitude vs offset (AVO) traces for the 20 percent slab within the 5 percent velocity layer (left-hand-panel) and with only the 5 percent layer (right-hand-panel). The traces have the background response removed. The same plot scale was used for both figures.

For the same earth model, time-domain magnetic field responses were calculated using the Wang and Hohmann code (Wang and Hohmann, 1993). The $dB_z(t)/dt$ with a conductivity of the pore fluid $\sigma_f = 0.29\,S/m$ for the entire layer at 280-300 m (Figure 2.1) is shown in Figure 2.4, along with the background response. From the voltage induced in a small loop of wire inside the transmitter loop, the apparent conductivity (or apparent resistivity) can be determined as a function of time. The resistivity is the

inverse of the conductivity. The earth model is shown in Figure 2.1, along with the electrical parameters shown in Figure 2.4. The formation factor $F = \sigma_f / \sigma = \rho / \rho_f$, σ_f is the pore fluid conductivity and σ is the bulk conductivity that is determined from EM exploration methods. (ρ_f is the pore fluid resistivity and ρ is the bulk resistivity.)

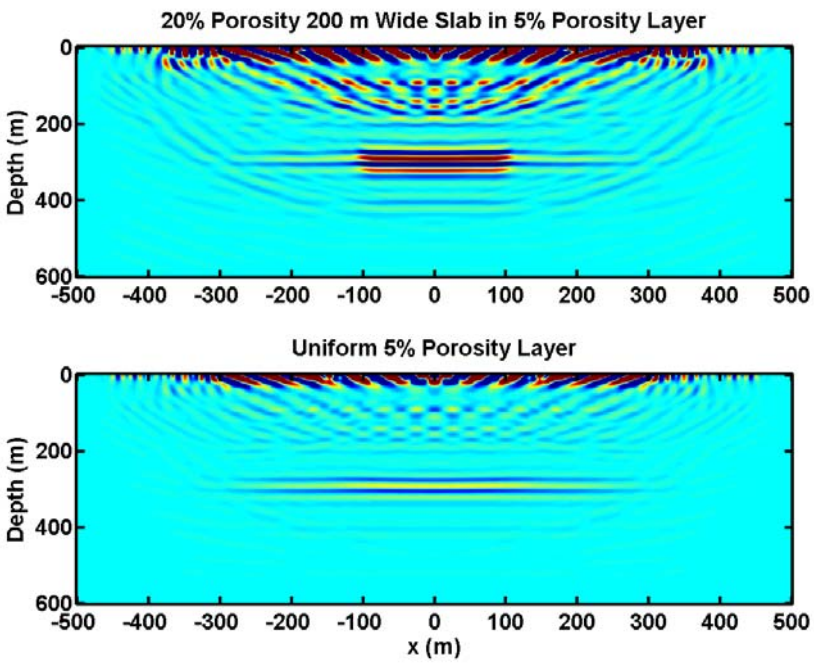

Figure 2.3: RTM zero-lag cross-correlation images of the 20 percent porosity slab within a 5 percent porosity layer (top panel) and the 5 percent porosity layer only (bottom panel). The same color scale was used for both images.

The observed voltage (*emf* induced in a loop of wire with radius *a* is

$$emf = -\frac{\partial}{\partial t}\oint d\mathbf{A}\cdot\mathbf{B}(t) \approx -\pi a^2 \frac{\partial B_z(t)}{\partial t} \tag{2.6}$$

where the transient response for the time-rate-of-change of B_z, $dB_z(t)/dt$ from Ward and Hohmann (1987) is

$$\begin{aligned} \frac{\partial B_z(t)}{\partial t} &= -\frac{I}{\sigma a^3}\left\{3erf(\theta a) - \frac{2}{\sqrt{\pi}}\theta a\left[3 + 2\theta^2 a^2 exp\left(-\theta^2 a^2\right)\right]\right\} \\ \theta &= \left(\frac{\mu_0 \sigma}{4t}\right)^{1/2} \end{aligned} \tag{2.7}$$

Here σ is the conductivity , t is the time , and μ_0 is the magnetic permeability of free space with a value of $4\pi \times 10^{-7}\, henrys/m$. The above equations assume that **B** is

approximately uniform over the area of the small loop of radius a. The solution for the apparent conductivity σ is found iteratively by solving for the conductivity, σ, (or apparent resistivity, 1/σ) in Equation (2.7) that produces the *emf*. $dB_z(t)/dt$ as a function of time for the earth model shown in Figure 2.1 is shown in Figure 2.4**.** The apparent resistivity is shown in Figure 2.5.

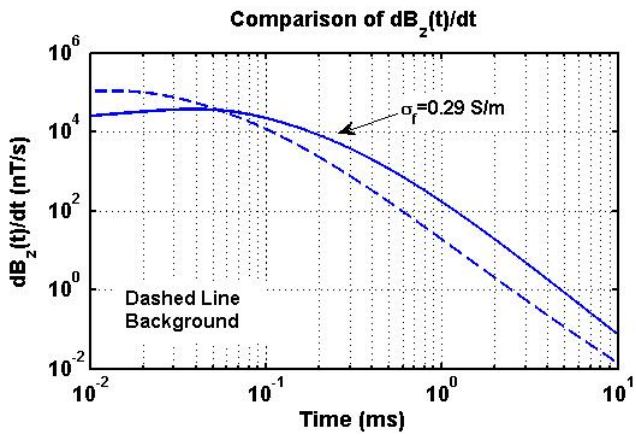

$$Layer\,1\,\phi = 0.3, F = 5.4$$
$$Layers\,2\,\&\,4\,\phi = 0.03,\ F = 136$$
$$Layer\,3\,\phi = 0.05, F = 66.3$$
$$Slab\ \phi = 0.2, F = 9.52$$

$$\sigma_f = 0.29\,S/m\ 2000\ ppm$$
$$= 0.1\,S/m\ 750\ ppm$$
$$= 0.017\,S/m\ 100\ ppm$$

Figure 2.4: $dB_z(t)/dt$ **as a function of time for the earth model shown in Figure 2.1. The dashed line shows response with no conducting layer.**

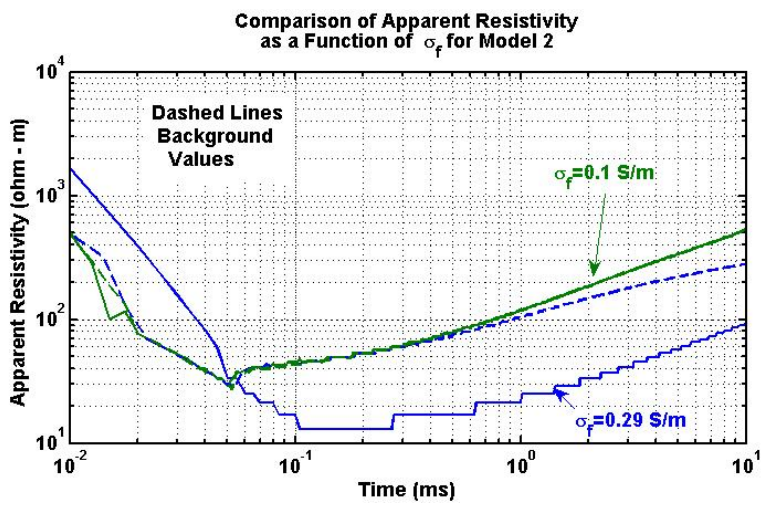

Figure 2.5: Apparent resistivity as a function of time. The dashed lines shows responses with no conducting layers.

From an examination of Figure 2.5, if the entire 20 *m* thick layer has a pore water conductivity of 0.29 *S/m*, the layer is clearly discernable (significant change from background); however for the pore water conductivity of 0.1 *S/m*, the layer is virtually undetectable. The transient EM method will detect a very conducting, thin layer.

Consider another model, which is simpler than the model in Figure 2.1. Figure 2.6 shows the earth model for a 60 m thick layer buried in an otherwise homogeneous half-space, where the depth ranges from 280 *m* to 340 *m*. The porosity of the 60 *m* thick layer

is 0.3; whereas the rest of the half-space has a porosity of 0.03. The RTM image is shown in Figure 2.7. The red "stripe" images the top with the yellow "stripe" imaging the bottom of the high porosity layer.

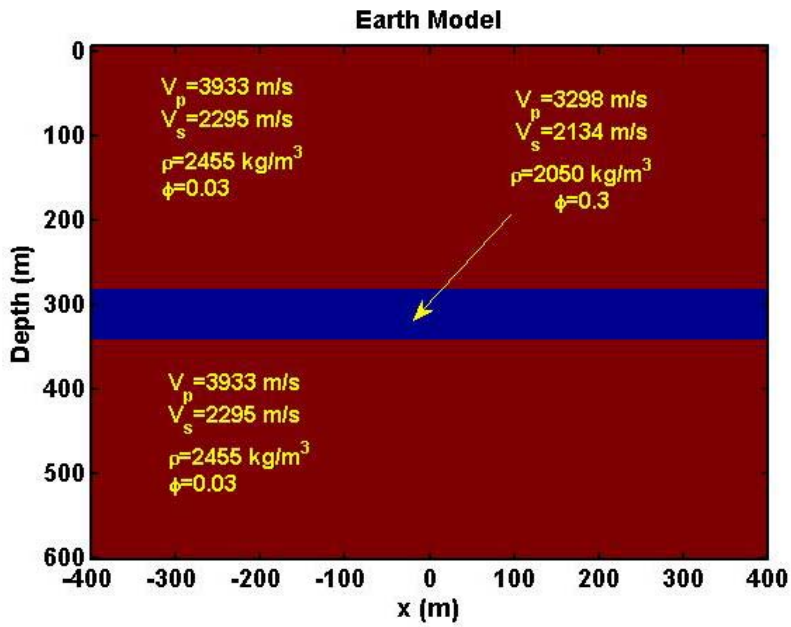

Figure 2.6: Earth model for a single high porosity layer.

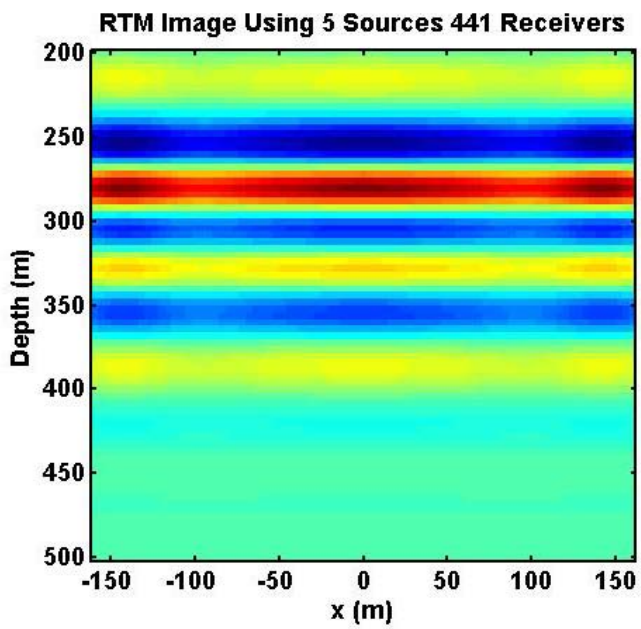

Figure 2.7: Reverse time migration image of the model shown in Figure 2.6. The top (280 *m*) and the bottom (340 *m*) of the high porosity layer are clearly imaged by the RTM method.

Figure 2.8 shows the $dB_z(t)/dt$ response for both the background (homogenous half-space) and the high porosity layer filled with three different pore fluid conductivities

(0.017 *S/m* – 100 *ppm* NaCl, 0.1 *S/m* – 750 *ppm*, and 0.29 *S/m* – 2000 *ppm*). In all cases there is a clear distinction between the fluid filled layer and the background.

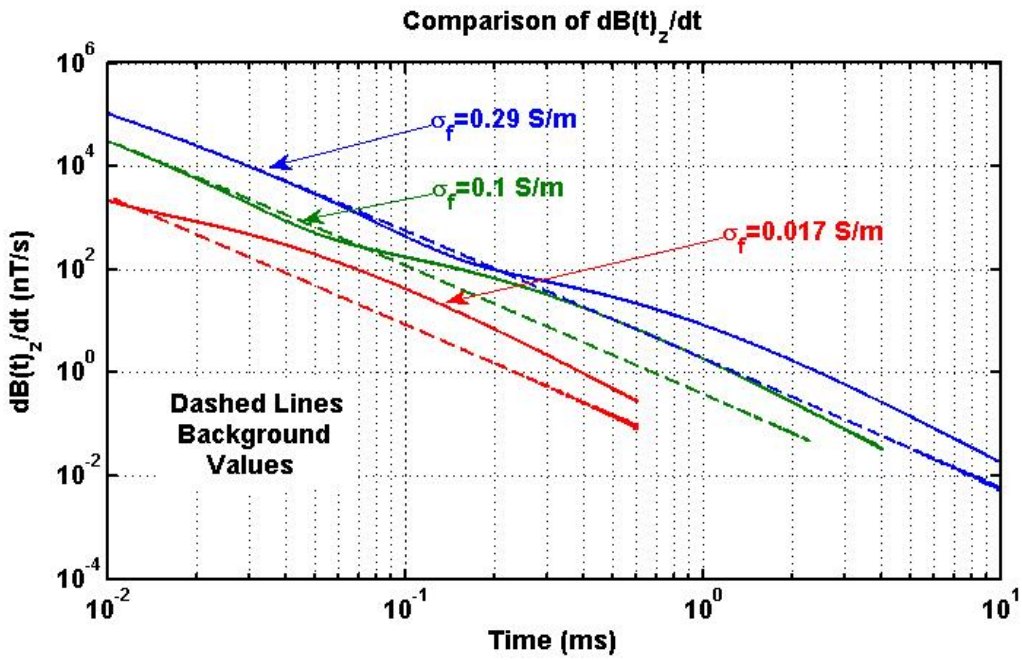

Figure 2.8: $dB_z(t)/dt$ **as a function of time for the model shown in Figure 2.6. The electrical parameters are given in this figure.**

The apparent resistivities as a function of time calculated using equation (2.7) for the three values of pore water conductivity given above are shown in Figure 2.9. From an examination of the figure, the apparent resistivity at early times is that of the background, then for increasing time, there is an "overshoot" of the apparent resistivity before decreasing at later times. The time of the low point in the apparent resistivity increases with time as the pore water conductivity increases. Without the constraint of the seismic image (Figure 2.7), the depth of the of the high porosity zone is not transparent from the EM data alone.

The diffusion Green's function (Ward and Hohmann, 1987) is

$$g(\mathbf{x},t)_d = \frac{\mu I}{4\pi t} exp\left(-\mu\sigma R^2/4t\right) \tag{2.8}$$

where R is the distance and t is the time. With the Green's function $g(\mathbf{x},t)_d$, the maximum in the signal at any distance R arrives at the time

$$t = \frac{\mu\sigma R^2}{4}, \tag{2.9}$$

moreover, the signal at times much before this is exponentially small and can be neglected.

Consider, instead of $g(\mathbf{x},t)_d$ the negative of its radial derivative

$$-\frac{\partial g(x,t)}{\partial R} = \frac{\mu I}{4\pi t}\frac{\mu\sigma R}{2t}\exp\left(-\mu\sigma R^2/4t\right). \tag{2.10}$$

The spatial maximum of the induced electric field $-\partial g_d/\partial R$ moves outward from the origin as time progresses. At time *t* the maximum of $-\partial g_d/\partial R$ is at the radial position

$$R_{\max} = \sqrt{\frac{2t}{\mu\sigma}}\,, \tag{2.11}$$

and moves through the conductor with the velocity of

$$\frac{\partial R_{max}}{\partial t} = \sqrt{\frac{1}{2\mu\sigma t}}\,, \tag{2.12}$$

which decreases with time as the electric field in the conductor becomes very smooth. Equation (2.12) is an expression for the diffusion velocity and can be used to roughly estimate the depth to the top of the conductor.

Using the diffusion velocity, the distance traveled by the maximum in the diffusion electric field is approximately 195 *m* using the time when the apparent resistivity in Figure 2.9 crosses the background value following the overshoot. The actual depth to the top of the high porosity zone is 280 *m*. The diffusion velocity given by equation (2.12) underestimates the distance by a factor of approximately 1.4.

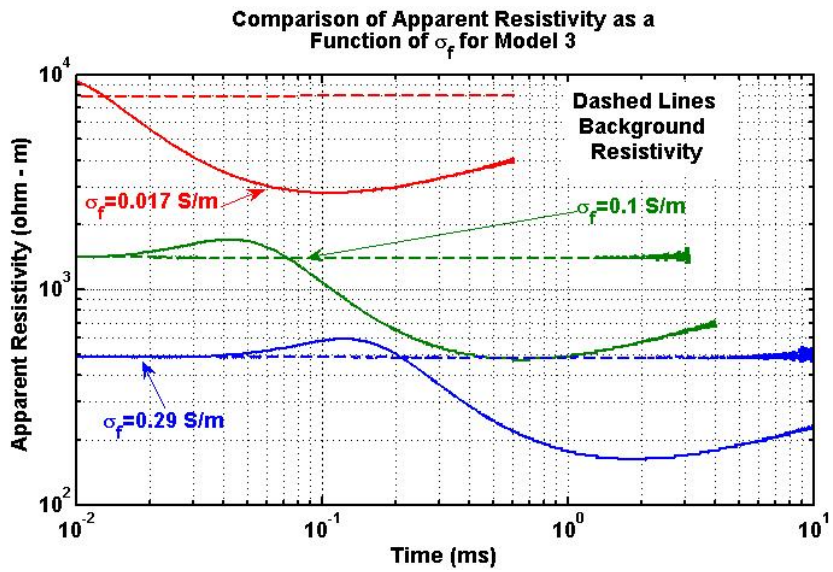

$$Layer\,1\&2\ \phi = 0.03, F = 136$$
$$Layers\,2\ \phi = 0.3,\ F = 5.4$$

$$\sigma_f = 0.29\,S/m\ 2000\ ppm$$
$$= 0.1\,S/m\ 750\ ppm$$
$$= 0.017\,S/m\ 100\ ppm$$

Figure 2.9: Apparent resistivity as a function of time for various pore water conductivities.

3.0 Seismic and EM Interactions

In this section, the interaction of seismic and EM waves will be discussed. These interactions are seismo-electric (SE), conversion of seismic energy to EM energy, and electro-seismic (ES), conversion of EM energy to seismic energy. Both of these effects have their roots in the so-called electric double layer (EDL), which will be discussed briefly below.

3.1 Introduction to Electrokinetics

When a surface is immersed or created in an aqueous solution, a discontinuity is formed at the interface where such physicochemical variables as electric potential and electrolyte concentration change significantly from the aqueous phase to another phase. Because of the different chemical potentials between the two phases, charge separation often occurs at the interfacial region. This interfacial region, together with the charged surface, is usually known as the electrical double layer (EDL). This layer, which can extend as far as 100 *nm* in a very dilute solution to only a few angstroms in a concentrated solution, plays an important role in electrochemistry, colloid science, and surface chemistry (Devasenathipathy and Santiago, 2003; Kirby and Hasselbrink, 2004; Yang *et al.*, 2004). In the context of the water salinity project, it plays an important role in the SE and ES effects because of its dependence upon the salinity of the water.

The phenomenon of electrokinetics may be broadly classified into four types: 1) electroosmosis, 2) electrophoresis, 3) streaming potential, and 4) sedimentation potential. These can be qualitatively described as follows: (Devasemathipathy and Santigo, 2003)

1. Electroosmosis is the motion of the bulk liquid in response to an applied electric field with EDLs on its wetted surfaces.
2. Electrophoresis is the motion (relative to the bulk liquid) of charged colloidal particles or molecules suspended in a solution that results upon the application of an electric field.
3. Streaming potential is the electric potential that develops along a channel with charged walls when a liquid is driven using pressure forces. The electric Joule current associated with this advective charge transport is called the streaming current.
4. Sedimentation potential is the electric potential that develops when charged colloidal particles are set in motion with respect to a stationary liquid. The driving force for this effect is typically gravity.

In this report we will be interested in the streaming potential and electroosmosis.

A simplified picture of the EDL is given in Figure 3.1.1. The net charge density on a pore wall in contact with an aqueous solution gives rise to an EDL. In general protonation, deprotonation, adsorption and other reaction equilibria define a net charge density q'' (units of charge per unit area, e.g., C/m^2), on the surface. This charge density creates an electric field, drawing oppositely charged ions (counterions) towards it and driving like-charged ions (co-ions) away, Figure 3.1.1. For example, in an aqueous KCl solution in contact with silica at pH 7, the H^+ (H_3O^+) and K_+ ions preferentially concentrate near the negatively charged surface. This shielding layer is commonly known as a Debye layer or EDL. Details of the structure of the EDL have historically been of significance to both electrochemistry as well as colloid science.

Most elementary double layer models are variations of the Gouy-Chapman-Stern (GCS) model, wherein the EDL is comprised of a Stern layer and a diffuse layer. The Stern layer of counterions lies at the distance of closest approach from the surface dictated by the size of the ion. Ions in the Stern layer are immobile, while in the diffuse layer the ions are mobile. The diffuse layer gives rise to electroosmosis and streaming potentials.

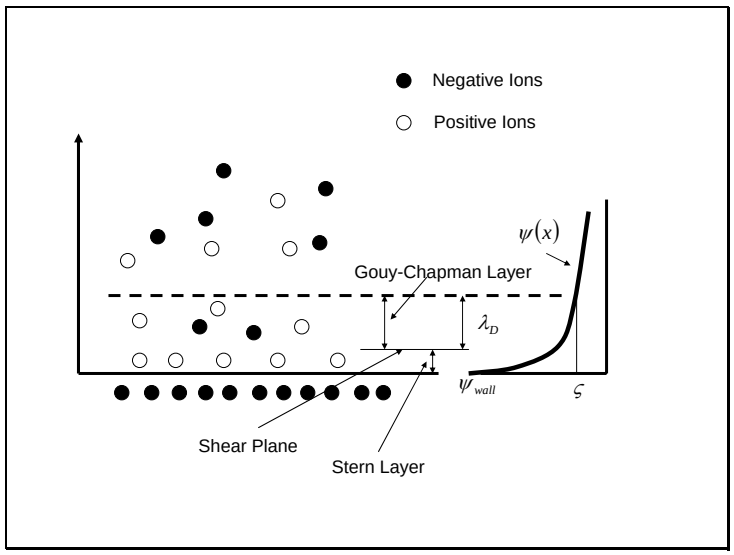

Figure 3.1.1: Schematic of a simple EDL model showing the shielding of the negatively charged wall surface by a stagnant layer of counter-ions (Stern layer) and a layer of mobile ions called the Gouy-Chapman layer. The two layers are separated by the shear plane. There is charge neutrality at large distances from the wall. On the right-hand side of the figure, a plot of the electrical potential as a function of distance from the wall is shown. The potential at the wall falls sharply to the potential at the shear plane, which is called the zeta potential ς, and then falls to zero far from the wall. The Debye screening length λ_D is the thickness of the Gouy-Chapman layer.

In this report we will be interested in the equilibrium condition and not on the dynamics of the system and how the system arrived at the equilibrium condition.

3.2 EDL Model-First Order

We will take a simplified model, which we think captures the essential physics of the problem. We will assume a one-dimensional system with the rock-fluid interface at x=0. The rock occupies the space for x<0 and the fluid occupies the space x>0 with the interface at x=0. Here we assume that the Stern layer is infinitely thin and the shear plane is at x=0. The ions in the Stern layer are immobile. The electric potential at the Stern layer, x=0 is the zeta potential ζ. In the elementary theories, the charges are assumed to be point charges and the fluid is a continuum.

For $x \geq 0$ in what is termed the diffuse layer, consider Poisson's equation for a true charge distribution of ρ^{true}. Poisson's equation is

$$\nabla^2 \psi = -\frac{\rho^{true}}{\kappa^f \varepsilon_0} \tag{3.2.1}$$

In one dimension we have

$$\frac{d^2\psi}{dx^2} = -\frac{\rho^{true}}{\varepsilon^f}, \quad \varepsilon^f = \kappa^f \varepsilon_0 \tag{3.2.2}$$

where ε_0 is the electric permittivity of free space, κ^f is the dielectric constant of the fluid, and the product ε^f is the electric permittivity of the fluid. Here the *x*-direction is perpendicular to the pore wall.

The concentration profile in the diffuse ion region of the electric double layer (EDL) can be described by the Boltzmann distribution and is a result of the balance between electromigration and diffusive fluxes. For the EDL on a flat plate such as a rock-fluid interface, the Boltzmann distribution of ions of species *i* and concentration c_i is

$$c_i(x) = c_{\infty,i}\, exp\left(-\frac{z_i e\psi(x)}{k_B T}\right) \tag{3.2.3}$$

where $c_{\infty,i}$ is the concentration of ion *i* in the liquid far from the wall, $\psi(x)$ is the electrical potential associated with the EDL charges of the Gouy-Chapmann layer, z_i is the valence number of ion *i*, *e* is the elemental charge, and *T* is the absolute temperature of the liquid. k_B is Boltzmann's constant. The net charge density in the electric double layer (EDL), ρ^{true}, is related to the molar concentrations of *N* species by

$$\rho^{true} = F\sum_{i=1}^{N} z_i c_i \tag{3.2.4}$$

where *F* is Faraday's constant 96485.306 *coulombs/gm equivalent*. (Note: $F=N_A e$, where N_A is Avogadro's number and *e* is the charge of an electron.) Thus we have

$$\frac{d^2\psi}{dx^2} = -\frac{\rho^{true}}{\varepsilon^f} = \frac{-F}{\varepsilon^f}\sum_{i=1}^{N} z_i c_{\infty,i} \exp\left(-\frac{z_i e\psi(x)}{k_B T}\right) \tag{3.2.5}$$

For a single, symmetric electrolyte (equal number of positive and negative ions), we can obtain a well-known form of the non-linear Poisson-Boltzmann equation

$$\frac{d^2\psi(x)}{dx^2} = \frac{2Fzc_\infty}{\varepsilon^f}\sinh\left(\frac{ze\psi(x)}{k_B T}\right) \tag{3.2.6}$$

For small arguments, the sinh function is equal to its argument. Thus we have

$$\frac{d^2\psi(x)}{dx^2} = \frac{2Fzc_\infty}{\varepsilon^f}\frac{ze\psi(x)}{k_BT} = \frac{1}{\lambda_D^2}\psi(x)$$
$$\lambda_D = \sqrt{\frac{\varepsilon^f k_B T}{2Fz^2ec_\infty}} = \sqrt{\frac{\varepsilon^f k_B T}{2N_A z^2 e^2 c_\infty}} \tag{3.2.7}$$

where λ_D is the Debye screening length and depends inversely as the square root of the concentration – the higher the concentration of the electrolyte the shorter the screening length. Solutions to equation (3.2.7) are of the form

$$\psi(x) = a\exp(kx) + b\exp(-kx)$$
$$k = 1/\lambda_D \tag{3.2.8}$$

where *a* and *b* are constants and *x* is still distance. In order for the potential to remain finite far from the pore wall, it must be that *a*=0. The potential at the shear plane (*x*=0) is ζ . Thus equation (3.2.8) becomes

$$\psi(x) = \zeta\, exp(-x/\lambda_D)$$
$$\left.\frac{d\psi(x)}{dx}\right|_{x=0} = -\frac{\zeta}{\lambda_D} \tag{3.2.9}$$

The charge density becomes

$$\rho^{true}(x) = -\frac{\varepsilon^f}{\lambda_D^2}\psi(x) = -\frac{\varepsilon^f}{\lambda_D^2}\varsigma\, exp(-x/\lambda_D)$$
$$\rho_{total}^{true} = -\frac{\varepsilon^f}{\lambda_D^2}\varsigma\int_0^\infty dx\, exp(-x/\lambda_D) = -\frac{\varepsilon^f\varsigma}{\lambda_D^2}(-\lambda_D)exp(-x/\lambda_D)\Big|_0^\infty \tag{3.2.10}$$
$$q'' = -\frac{\varepsilon^f\varsigma}{\lambda_D}\ \frac{coulombs}{unit\ area}$$

If the surface charge density q'' is unaffected by counterion strength (Kirby and Hasselbrink; 2004), and all the shielding is performed by the diffuse portion of the double layer, then the dependence of ς on counterion concentration (given constant temperature and dielectric constant) can be shown to be from equations (3.2.7 and 3.2.10)

$$\varsigma \sim \lambda_D \sim c_\infty^{-1/2} z^{-1}. \tag{3.210a}$$

The ς-potential decreases as the concentration of the electrolyte increases. In the context of the problem being addressed in this report, the ς-potential decreases as the salinity of the water increases.

The introduction of an electric field results in the flow of charged ions. The governing equation for this is a simplified form of the Navier-Stokes equations in which the flow is presumed steady, low Reynolds number, and the non-linear advective term is assumed negligible. Thus we have (*e.g.*, Devasenathipathy and Santiago, 2003; Kirby and Hasselbrink, 2004)

$$\nabla P = \eta \nabla^2 \mathbf{v} + \rho^{true} \mathbf{E}$$
$$\nabla^2 \left(\mathbf{v} - \frac{\varepsilon_f}{\eta} \mathbf{E} \right) = \frac{\nabla P}{\eta} \tag{3.2.11}$$

Here P is the pressure, η is the dynamic viscosity, ρ^{true} is the charge density, and $\mathbf{v}$ and $\mathbf{E}$ are the velocity and electric field, respectively. The charge density is related to the Laplacian of the potential, equation (3.2.1), and for a constant pressure, equation (3.2.11) becomes

$$\nabla^2 \mathbf{v} = \frac{\varepsilon_f \mathbf{E}}{\eta} \nabla^2 \psi \tag{3.2.12}$$

For unidirectional flow in the direction parallel to the pore wall (y-direction), we have the velocity as a function of the electric potential where now the boundary conditions are $v_y(x=0)=0$ and $v_y(x \to \infty) = \bar{v}_y$ where $\bar{v}_y$ is the flow far from the pore wall. We have then in terms of the potential ψ $v(\psi = \varsigma) = 0$ and $v(\psi \to 0) \to \bar{v}$. In general we can write for the velocity component parallel to the pore wall as a function of the distance from the wall

$$v_y = -\frac{\varepsilon_f \varsigma}{\eta} E_y \left(1 - \frac{\psi}{\varsigma} \right). \tag{3.2.13}$$

For thin EDL, the electric potential throughout most of the cross-sectional area of a pore is zero and equations (3.2.12 and 3.2.13) for the case of zero pressure gradient, reduces to

$$v_y = -\frac{\varepsilon_f \varsigma}{\eta} E_y \tag{3.2.14}$$

which is the Helmholtz-Smoluchowski relation for electroosmotic flow (Devasemathipathy and Santiago, 2003).

The ion mobility is defined as the velocity $\mathbf{v}$ divided by the electric field. Thus the mobility μ_{ion} is

$$\begin{aligned} \mu_{ion} &= -\frac{\varepsilon_f \varsigma}{\eta}\left(1-\frac{\psi}{\varsigma}\right) \\ \mu_{ion}\Big|_{x=0} &= 0 \\ \mu_{ion}\Big|_{x\to\infty} &= -\frac{\varepsilon_f \varsigma}{\eta} \end{aligned} \quad . \tag{3.2.15}$$

This mobility governs the electroosmosis and streaming current effects.

The transport of ions in pore structure is described in terms of convection and migration resulting from the pressure difference and electric potential gradient, respectively. Diffusion is neglected. The accumulation of ions sets up and electric field *E*, with the streaming potential difference $\Delta\varphi(= EL)$. This causes the conduction current I_C to flow back in the opposite direction. In steady state, the net current *I* should be zero.

$$I \equiv I_S + I_C = 0 \tag{3.2.16}$$

The streaming current, I_s, can be given by the ion mobility, equation (3.2.15), times a pressure gradient and the countering conduction current, I_c, is given by the electrical conductivity of the fluid times the electric potential gradient. Thus

$$\begin{aligned} I_S &= -\frac{\varepsilon_f \varsigma}{\eta} A \frac{\Delta P}{L} \\ I_C &= \sigma_f A \frac{\Delta\varphi}{L} \end{aligned} \quad , \tag{3.2.17}$$

where σ_f is the pore fluid conductivity and L and A are a length and area, respectively. This leads to the Smoluchowski equation (Kirby and Hasselbrink, 2004)

$$\frac{\Delta\varphi}{\Delta P} = \frac{\varepsilon_f \varsigma}{\eta \sigma_f} \, . \tag{3.2.18}$$

Equation (3.2.18) leads to the electrokinetic coefficients discussed below.

4.0 1D Coupled Pressure and EM Waves – Seismoelectric Wave Propagation

The purpose of this section of the report paper is to examine the seismoelectric effect in one dimension so that an analytic solution can be obtained. These analytical solutions give insight to the SE and ES effects.

For the fluid, the 1D equations of motion are

$$\begin{aligned} \rho\frac{\partial v}{\partial t} &= -\frac{\partial p}{\partial z} + f \\ \frac{\partial p}{\partial t} &= -K_f\frac{\partial v}{\partial z} - \frac{1}{3}\frac{\partial m}{\partial t} \end{aligned}, \tag{4.1}$$

where f is a body force and m is a moment source. Taking the time derivative of the pressure equations and using the velocity equation, we get

$$\frac{\partial^2 p}{\partial z^2} - \frac{1}{\alpha^2}\frac{\partial^2 p}{\partial t^2} = \frac{\partial f}{\partial z} + \frac{1}{3\alpha^2}\frac{\partial^2 m}{\partial t^2}. \tag{4.2}$$

where α is the compressional wave speed in the fluid medium ($\alpha = \sqrt{K_f/\rho}$). Taking the time derivative of the velocity equation and using the pressure equation, we get

$$\frac{\partial^2 v}{\partial z^2} - \frac{1}{\alpha^2}\frac{\partial^2 v}{\partial t^2} = -\frac{1}{K_f}\frac{\partial f}{\partial t} + \frac{1}{3K_f}\frac{\partial^2 m}{\partial t\partial z} \tag{4.3}$$

The electrokinetic equations are (Moore, *et al*., 2004)

$$\begin{aligned} \mathbf{q} &= -L_{11}\nabla p + L_{12}\mathbf{e} \\ \mathbf{j} &= -L_{21}\nabla p + L_{22}\mathbf{e} \\ L_{21} &= L_{12} = -\frac{\varepsilon\varsigma}{\eta F} \\ L_{11} &= \frac{k_h}{\eta} \\ L_{22} &= \sigma \end{aligned}, \tag{4.4}$$

where **q** is the fluid flow due to a pressure gradient and an electric field, **j** is the electric current density due to a pressure gradient and an electric field. In the expressions for the coupling coefficients, ς is the zeta potential (which is a function of salinity and water quality), η is fluid viscosity, F is the formation factor, and k_h is the hydraulic

permeability. The formation factor is the ratio of the pore water conductivity to the bulk apparent conductivity. Note that the L_{12} coefficient is the bulk conductivity times the Smoluchowski equation (Kirby and Hasselbrink, 2004), equation (3.2.18). For the static case where there is no fluid flow, the gradient of the pressure body force term is counterbalanced by the charge density times the electric field. Thus following Neev and Yeatts (1989) the body force term is

$$\mathbf{f} = \nabla p = \frac{L_{12}}{L_{11}}\mathbf{e} = \rho_c \mathbf{e}\,. \tag{4.5}$$

For the EM fields, Maxwell's equations that includes the electokinetic effects gives rise to an electrical current as a source term. Thus

$$\begin{aligned}
&\nabla \times \mathbf{e} = -\frac{\partial \mathbf{b}}{\partial t} \\
&\nabla \times \mathbf{h} = \frac{\partial \mathbf{d}}{\partial t} + \mathbf{j} \\
&\mathbf{j} = \sigma\,\mathbf{e} - L_{21}\nabla p + \mathbf{j}_{imp} \\
&\nabla \times \mathbf{b} = \varepsilon\mu\frac{\partial \mathbf{e}}{\partial t} + \mu\sigma\,\mathbf{e} - \mu\,L_{21}\nabla p + \mu\,\mathbf{j}^{imp} \\
&\mathbf{b} = \mu\,\mathbf{h} \\
&\mathbf{d} = \varepsilon\,\mathbf{e}
\end{aligned} \quad , \tag{4.6}$$

where μ is the magnetic permeability (usually taken to be that of free space $\mu_0 = 4\pi \times 10^{-7}\ henrys/m$), ε is the electric permittivity of the medium, σ is the electrical conductivity of the medium (L_{22} coefficient), and $\mathbf{j}^{imp}$ is the external impressed current density. Solving for a second order differential equation for the electric field we have

$$\begin{aligned}
&\nabla \times \frac{\partial \mathbf{b}}{\partial t} = \varepsilon\mu\frac{\partial^2 \mathbf{e}}{\partial t^2} + \mu\sigma\frac{\partial \mathbf{e}}{\partial t} - \mu\,L_{21}\nabla\frac{\partial p}{\partial t} + \mu\frac{\partial \mathbf{j}^{imp}}{\partial t} \\
&\nabla \times \mathbf{e} = -\frac{\partial \mathbf{b}}{\partial t} \\
&-\nabla \times \nabla \times \mathbf{e} - \varepsilon\mu\frac{\partial^2 \mathbf{e}}{\partial t^2} - \mu\sigma\frac{\partial \mathbf{e}}{\partial t} = -\mu\,L_{21}\nabla\frac{\partial p}{\partial t} + \mu\frac{\partial \mathbf{j}^{imp}}{\partial t} \\
&\nabla^2\mathbf{e} - \nabla(\nabla \cdot \mathbf{e}) - \varepsilon\mu\frac{\partial^2 \mathbf{e}}{\partial t^2} - \mu\sigma\frac{\partial \mathbf{e}}{\partial t} = -\mu\,L_{21}\nabla\frac{\partial p}{\partial t} + \mu\frac{\partial \mathbf{j}^{imp}}{\partial t}
\end{aligned} \quad , \tag{4.7}$$

In 1D we have for the electric field in the *z*-direction (the direction of the pressure gradient) we have

$$\frac{\partial^2 e_z}{\partial z^2} - \varepsilon\mu \frac{\partial^2 e_z}{\partial t^2} - \mu\sigma \frac{\partial e_z}{\partial t} - = -\mu L_{21} \frac{\partial^2 p}{\partial z \partial t} + \mu \frac{\partial j_z^{imp}}{\partial t}. \tag{4.8}$$

The coupled equations are (dropping the z subscript)

$$\begin{aligned}
&\frac{\partial^2 e}{\partial z^2} - \frac{1}{c^2}\frac{\partial^2 e}{\partial t^2} - \mu\sigma \frac{\partial e}{\partial t} = -\mu L_{21} \frac{\partial^2 p}{\partial z \partial t} + \mu \frac{\partial j^{imp}}{\partial t} \\
&\frac{\partial^2 p}{\partial z^2} - \frac{1}{\alpha^2}\frac{\partial^2 p}{\partial t^2} = \frac{\partial f}{\partial z} + \frac{1}{3\alpha^2}\frac{\partial^2 m}{\partial t^2} \\
&\frac{\partial^2 v}{\partial z^2} - \frac{1}{\alpha^2}\frac{\partial^2 v}{\partial t^2} = -\frac{1}{K_f}\frac{\partial f}{\partial t} + \frac{1}{3K_f}\frac{\partial^2 m}{\partial t \partial z} \\
&\rho_c = \frac{L_{12}}{L_{11}},\ c = \frac{1}{\sqrt{\varepsilon\mu}},\ \alpha = \sqrt{\frac{K_f}{\rho}}
\end{aligned} \tag{4.9}$$

The above equations can be solve in pairs $e(z,t)$ and $p(z,t)$ or $e(z,t)$ and $v(z,t)$. For simplicity, we will show the solution for the electric field and pressure. Assume 1D solutions of the type

$$\begin{aligned}
p(z,t) &= \frac{1}{2\pi}\int_{-\infty}^{\infty} d\omega \frac{1}{2\pi}\int_{-\infty}^{\infty} dk P(k,\omega) exp(-ikz + i\omega t) \\
e(z,t) &= \frac{1}{2\pi}\int_{-\infty}^{\infty} d\omega \frac{1}{2\pi}\int_{-\infty}^{\infty} dk E(k,\omega) exp(-ikz + i\omega t)
\end{aligned} \tag{4.10}$$

The moment source is of the form,

$$\begin{aligned}
m(z,t) &= s(t)\delta(z - z_0) \\
&= \frac{1}{2\pi}\int_{-\infty}^{\infty} d\omega \frac{1}{2\pi}\int_{-\infty}^{\infty} dk S(k,\omega) exp[-ikz + i\omega t] \\
S(k,\omega) &= \frac{1}{2\pi}\int_{-\infty}^{\infty} dt \int_{-\infty}^{\infty} dz s(t)\delta(z - z_0) exp[ikz - i\omega t], \\
&= \int_{-\infty}^{\infty} dt s(t) exp(ikz_0 - i\omega t) = S(\omega) exp(ikz_0)
\end{aligned} \tag{4.11}$$

where the strength of the source is included in S. For now we will set the impressed current density equal to zero, we will examine a non zero current later.

Development of the appropriate equations is given in Appendix A In the frequency and k-space domain, the solutions for the electric field and pressure are

$$E(k,\omega)=\frac{\omega^3\mu L_{21}}{3\alpha^2}\frac{kS(\omega)exp(ikz_0)}{(k-M_1)(k+M_1)(k-M_2)(k+M_2)}$$
$$P(k,\omega)=\frac{\omega^2}{3\alpha^2}\frac{(k-\vartheta)(k+\vartheta)S(\omega)exp(ikz_0)}{(k-M_1)(k+M_1)(k-M_2)(k+M_2)} \tag{4.12}$$

where

$$M_1=\sqrt{A+B},\ \ M_2=\sqrt{A-B}$$
$$A=\frac{\vartheta^2+\varphi^2+i\rho_c\omega\mu L_{21}}{2},B=\frac{\sqrt{\left(\vartheta^2+\varphi^2+i\rho_c\omega\mu L_{21}\right)^2-4\vartheta^2\varphi^2}}{2} \tag{4.13}$$
$$\varphi=\frac{\omega}{\alpha},\ \ \vartheta=\frac{\omega}{c}\sqrt{1-ic^2\mu_0\sigma/\omega}$$

The coupled particle velocity and electric field equations can be derived in a similar manner. For both the electric field and the pressure there are four poles. These poles correspond to two solutions for positive *z* propagation and two solutions for negative *z* propagation. To identify the modes, as $\rho_c\to 0$, $M_1\to\vartheta$ which is associated with the EM field propagation and the $M_2\to\varphi$ which is associated with seismic wave propagation. Moving the poles off the real axis and performing the contour integration in *k*-space, we get

$$e(z,t)=\frac{i\mu L_{21}}{4\pi}\int_{-\infty}^{\infty}d\omega\left(\frac{\omega^3}{3\alpha^2}S(\omega)\right)$$
$$\times\left[\frac{exp\left[-i\,sgn(z-z_0)M_1|z-z_0|+i\omega t\right]-exp\left[-i\,sgn(z-z_0)M_2|z-z_0|+i\omega t\right]}{(M_1-M_2)(M_1+M_2)}\right]$$
$$p(z,t)=-i\frac{1}{4\pi}\int_{-\infty}^{\infty}d\omega\frac{\omega^2}{3\alpha^2}S(\omega)\frac{1}{(M_1-M_2)(M_1+M_2)} \tag{4.14}$$
$$\times\left[\begin{array}{c}\dfrac{(M_1-\vartheta)(M_1+\vartheta)exp\left[-i\,sgn(z-z_0)M_1|z-z_0|+i\omega t\right]}{M_1}\\ -\dfrac{(M_2-\vartheta)(M_2+\vartheta)exp\left[-i\,sgn(z-z_0)M_2|z-z_0|+i\omega t\right]}{M_2}\end{array}\right]$$

For a band limited source $S(\omega)$ we can use FFT methods to perform the indicated integrals. Since $M_1\approx\vartheta$ and $M_2\approx\varphi$, there are two electric field solutions one traveling at EM wave speeds dictated by M_1 and one traveling at seismic wave speeds dictated by M_2. Since $M_1\approx\vartheta$ there is only one solution of the pressure, a wave traveling at seismic wave speeds.

For an electric current source similar to a moment source we have

$$
\begin{aligned}
\bar{j}(z,t) &= j(t)\delta(z-z_0) \\
&= \frac{1}{2\pi}\int_{-\infty}^{\infty} d\omega \frac{1}{2\pi}\int_{-\infty}^{\infty} dk J(k,\omega) exp[-ikz+i\omega t] \\
J(k,\omega) &= \frac{1}{2\pi}\int_{-\infty}^{\infty} dt \int_{-\infty}^{\infty} dz s j(t)\delta(z-z_0) exp[ikz-i\omega t] \\
&= \int_{-\infty}^{\infty} dt\, j(t) exp(ikz_0 - i\omega t) = J(\omega) exp(ikz_0)
\end{aligned}
\tag{4.15}
$$

$$
\begin{aligned}
E(k,\omega) &= -i\omega\mu \frac{(k-\varphi)(k+\varphi)J(\omega)exp(ikz_0)}{(k-M_1)(k+M_1)(k-M_2)(k+M_2)} \\
P(k,\omega) &= -\mu\rho_c \frac{\omega k J(\omega) exp(ikz_0)}{(k-M_1)(k+M_1)(k-M_2)(k+M_2)}
\end{aligned}
\tag{4.16}
$$

Similar to the moment source, for both the electric field and the pressure there are four poles. Again these poles correspond to two solutions for positive *z* propagation and two solutions for negative *z* propagation. Moving the poles off the real axis and performing the contour integration in *k*-space, we get

$$
\begin{aligned}
e(z,t) &= -sgn(z-z_0)\mu \frac{1}{4\pi}\int_{-\infty}^{\infty} d\omega\omega \frac{J(\omega)}{(M_1-M_2)(M_1+M_2)} \\
&\times \left[\frac{(M_1-\varphi)(M_1+\varphi)exp[-iM_1(z-z_0)+i\omega t]}{M_1} - \frac{(M_2-\varphi)(M_2+\varphi)exp[-iM_2(z-z_0)+i\omega t]}{M_2} \right] \\
p(z,t) &= i\mu\rho_c \frac{1}{4\pi}\int_{-\infty}^{\infty} d\omega\omega J(\omega) \\
&\times \left[\frac{exp[-i\,sgn(z-z_0)M_1|z-z_0|+i\omega t] - exp[-i\,sgn(z-z_0)M_2|z-z_0|+i\omega t]}{(M_1-M_2)(M_1+M_2)} \right]
\end{aligned}
\tag{4.17}
$$

Since $M_1 \approx \vartheta$ and $M_2 \approx \varphi$, there are two pressure solutions one traveling at EM wave speeds dictated by M_1 and one traveling at seismic wave speeds dictated by M_2. Since $M_2 \approx \varphi$ there is only one solution for the electric field, a wave traveling at EM wave speeds.

Figure 4.1 illustrates the effects of varying the ς-potential and the pore water electrical conductivity σ_f, which is related to the pore water salinity. From Lorne, *etal.* (1999) we estimate the relation between ς and σ_f as a function of pore water salinity. We have for our estimate

$$100\ ppm\ NaCl\ \ \varsigma = -20\,mv,\ \sigma_f = 0.017\,S/m$$
$$750\ ppm\ NaCl\ \ \varsigma = -6\,mv,\ \sigma_f = 0.1\ S/m$$
$$2000\ ppm\ NaCl\ \ \varsigma = -2\,mv,\ \sigma_f = 0.29\,S/m$$

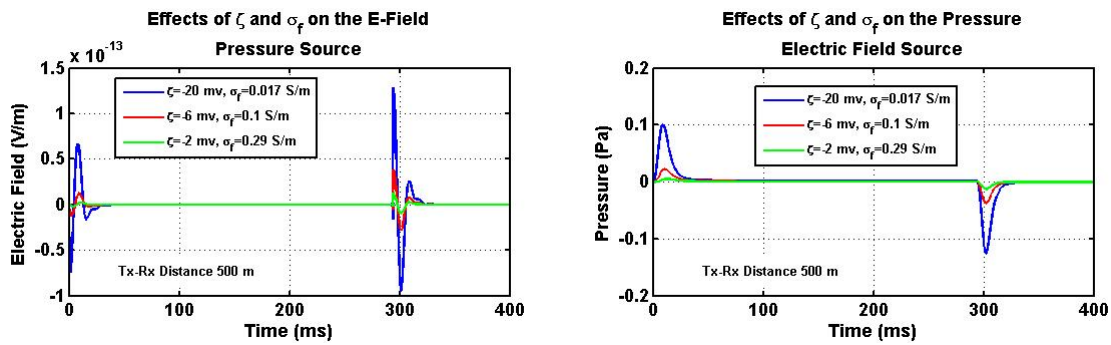

Figure 4.1: 1D analytic solutions to the coupled electric field and the pressure. Right-hand panel shows the electric field due to a pressure source and the left-hand panel show the pressure for an electric field source.

The SE and ES effects are illustrated in Figure 4.1. Salinity differences cause a significant detectable change in the SE and ES responses. For a pressure source, two electric field waves are initiated and propagated. In the left-hand panel, the wave near *t*=0 is the electric field traveling at EM wave speeds for the medium and the response near *t*=300 *ms* is an electric field traveling along with the pressure wave at seismic wave speeds due to the traveling pressure disturbance. In the right-hand panel, two pressure waves are generated by an electric field source. The pressure wave nearest *t*=0 is a pressure wave traveling along with the EM disturbance at EM wave speeds for the medium. The pressure wave near *t*=300 *ms* is traveling at seismic wave speeds. Both of the electric field wave depicted in the left-hand panel have been observed; *e.g.* see Mikhailov, *et.al.*, 2000).. The pressure wave traveling at seismic wave speeds initiated by an electric field source has been observed; *e.g.*, Thompson (2005). However to our knowledge, the pressure or seismic wave traveling at EM wave speeds has not been reported. In our 2D calculations discussed below, the amplitude of the seismic wave traveling at EM wave speeds is much smaller than the amplitude of the seismic wave traveling at seismic wave speeds.

The 1D solutions given in this section gives us insight into the seismo-electric and electro-seismic effect. The solutions predict the behavior of the electric field for a seismic source and the pressure and/or particle velocity for an electric field source. The modes expressed in Figure 4.1 will be demonstrated below in the development and simulations for a 2D poroacoustic – EM coupled system..

5.0 2D Seismo-Electric and Electro-Seismic Algorithm

Prior to embarking on the development of a fully 3D coupled poroelastic and EM wavefields, we chose to develop a much simpler 2D algorithm. In the time domain, the poroelastic and EM time-stepping finite-difference algorithms would have different time steps and different spatial gridding. Typically, a poroelastic algorithm would have a time step on the order of 0.1 *ms* and a spatial grid of 1-5 *m*. On the other hand, for an EM algorithm the time step is on the order of $1-10\mu s$ and a spatial grid of 10-20 *m*. If one tries to put the poroelastic and EM algorithms on the same time and spatial scale, the time steps for the seismic calculations would be exceeding small leading to unnecessarily long computer runs.

5.1 Determination of Time Step – 1D Solutions

Wang and Hohmann (1993) used a fictitious electric permittivity γ to stabilize the solutions the EM finite-difference solutions. From the Courant-Friedrichs-Levy (CFL) stability condition with an EM wave speed of $v = \sqrt{1/\mu\gamma}$ they obtained for their 3D algorithm

$$\gamma \geq \frac{4}{\mu_{min}}\left(\frac{\Delta t}{\Delta_{min}}\right)^2 \tag{5.1.1}$$

In order to accurately represent the diffusion limit of EM "wave" propagation there are restrictions on the maximum value of γ. In the following, we will show how the maximum can be estimated using analytical 1D solutions for the electric and magnetic fields.

Maxwell's equations for an electrically conducting medium are:

$$\begin{aligned} \nabla \times \mathbf{e} &= -\frac{\partial \mathbf{b}}{\partial t} \\ \nabla \times \mathbf{h} &= \frac{\partial \mathbf{d}}{\partial t} + \mathbf{j} \end{aligned} \tag{5.1.2}$$

where constitutive relations are:

$$\begin{aligned}\mathbf{b} &= \mu_0 \mathbf{h} \\ \mathbf{d} &= \varepsilon \mathbf{e}\end{aligned} \quad . \tag{5.1.3}$$

where $\mu_0 = 4\pi \times 10^{-7}\, henrys/m$, the magnetic permeability of free space. The displacement current term comes from $\partial \mathbf{d}/\partial t$. In the following we will restrict the magnetic permeability to that of free space. The current consists of Ohm's law conduction and the impressed current (here we are ignoring the seismo-electric effect)

$$\mathbf{j} = \sigma \mathbf{e} + \mathbf{j}^{imp} \,. \tag{5.1.4}$$

Thus we have from equations (5.2-5.4)

$$\begin{aligned}\varepsilon \frac{\partial \mathbf{e}}{\partial t} + \sigma \mathbf{e} - \nabla \times \mathbf{h} &= -\mathbf{j}^{imp} \\ \mu_0 \frac{\partial \mathbf{h}}{\partial t} + \nabla \times \mathbf{e} &= 0\end{aligned} \quad . \tag{5.1.5}$$

Consider the plane-wave approximation for orthogonal **e** and **h**, e_x and h_y.

$$\begin{aligned}\varepsilon \frac{\partial e_x}{\partial t} + \sigma e_x - (\nabla \times \mathbf{h})_x &= j_x^{imp} \\ \varepsilon \frac{\partial e_x}{\partial t} + \sigma e_x - \left[\frac{\partial h_z}{\partial y} - \frac{\partial h_y}{\partial z}\right] &= j_x^{imp} \\ \varepsilon \frac{\partial e_x}{\partial t} + \sigma e_x + \frac{\partial h_y}{\partial z} &= j_x^{imp} \\ \mu_0 \frac{\partial h_y}{\partial t} + (\nabla \times \mathbf{e})_y &= 0 \\ \mu_0 \frac{\partial h_y}{\partial t} + \left[\frac{\partial e_x}{\partial z} - \frac{\partial e_z}{\partial x}\right] &= 0 \\ \mu_0 \frac{\partial h_y}{\partial t} + \frac{\partial e_x}{\partial z} &= 0\end{aligned} \quad . \tag{5.1.6}$$

Assume solutions of the form

$$\sim \exp(-ikz + i\omega t)$$

$$
\begin{aligned}
e_x(z,t) &= \frac{1}{2\pi}\int_{-\infty}^{\infty} d\omega \frac{1}{2\pi}\int_{-\infty}^{\infty} dk E(k,\omega)\exp(-ikz+i\omega t) \\
h_y(z,t) &= \frac{1}{2\pi}\int_{-\infty}^{\infty} d\omega \frac{1}{2\pi}\int_{-\infty}^{\infty} dk H(k,\omega)\exp(-ikz+i\omega t) \quad . \\
j_x^{imp}(z_0,t) &= \frac{1}{2\pi}\int_{-\infty}^{\infty} d\omega \frac{1}{2\pi}\int_{-\infty}^{\infty} dk J(k,\omega)\exp(-ikz_0+i\omega t)
\end{aligned}
\tag{5.1.7}
$$

Thus we have using equations (5.1.6) and (5.1.7)

$$
\begin{aligned}
E(k,\omega) &= \frac{i\mu\omega\, J(k,\omega)}{(k-\vartheta)(k+\vartheta)} \\
\vartheta &= \sqrt{\varepsilon\mu_0\omega^2 - i\mu_0\omega\sigma} \\
v &= 1\big/\sqrt{\varepsilon\mu_0} \\
H(k,\omega) &= \frac{ik\, J(k,\omega)}{(k-\vartheta)(k+\vartheta)}
\end{aligned}
\tag{5.1.8}
$$

The poles in equation (5.1.8) show that there are positive and negative going waves whose wave vector is given by ϑ. The $\varepsilon\mu_0\omega^2$ term in ϑ is the so-called displacement current term arising from $\partial\mathbf{d}/\partial t$ and it dominates at high frequency. At low frequencies the induction limit $\vartheta \to \sqrt{-i\omega\mu_0\sigma}$ dominates. A more complete derivation of the equations for the 1D electric and magnetic fields is given in Appendix B.

To solve for the electric and magnetic fields, we move the poles off the axis

$$
\begin{aligned}
e(z,t) &= \frac{1}{2\pi}\int_{-\infty}^{\infty} d\omega \frac{1}{2\pi}\int_{-\infty}^{\infty} dk E(k,\omega) exp(-ikz+i\omega t) \\
&= \frac{1}{2\pi}\int_{-\infty}^{\infty} d\omega \frac{1}{2\pi}\int_{-\infty}^{\infty} dk \frac{i\mu\omega J(k,\omega) exp(ikz_0)}{(k-\vartheta+i\delta)(k+\vartheta-i\delta)} exp(-ikz+i\omega t)
\end{aligned} \quad .
\tag{5.1.9}
$$

$$
\begin{aligned}
e(z,t) &= \frac{\mu_0}{4\pi}\int_{-\infty}^{\infty} d\omega \frac{\omega J(\omega)}{\vartheta} exp\left[-i\, sgn(z-z_0)\Theta|z-z_0| + i\omega t\right] \\
h(z,t) &= \frac{sgn(z-z_0)}{4\pi}\int_{-\infty}^{\infty} d\omega J(\omega) exp\left[-i\, sgn(z-z_0)\Theta|z-z_0| + i\omega t\right]
\end{aligned}
\tag{5.1.10}
$$

where $J(\omega)$ is assumed to be band limited.

Here

$$
\vartheta = \sqrt{\varepsilon\mu_0\omega^2 - i\mu_0\omega\sigma} \to \sqrt{\gamma\mu_0\omega^2 - i\mu_0\omega\sigma}
\tag{5.1.11}
$$

We can use the 1D solutions for the electric and magnetic fields to place an upper limit on $\gamma = \kappa_{eff}\varepsilon_0$ where κ_{eff} is an effective dielectric constant and $\varepsilon_0 = 8.854\times10^{-12}\ farads/m$ the electric permittivity. The diffusion limit is when the displacement current term is much smaller than $\mu_0\omega\sigma$.

Figures 5.1.1 and 5.1.2 illustrate the results of 1D calculations of the wave form of diffusion electric field ($\gamma = 0$) compared to the wave form for an effective dielectric constant. The purpose is to demonstrate how large of a fictitious dielectric constant is acceptable. A time step of $75\mu s$ with a spatial grid spacing of 10 m, equation (5.1.1) yields an effective dielectric constant of 2.02×10^7. The left-hand panel of Figure 5.1.1 shows the comparison of the 1D calculated electric fields for $\kappa_{eff} = 0$ and $\kappa_{eff} = 2.02\times10^7$ with a conductivity of 0.1 *S/m*. The difference between the diffusion solution and the solution with an effective dielectric constant may or may not be acceptable. The right-hand panel shows the comparison for a time step of $40\mu s$ yielding very little difference in the purely diffusion wave form and the wave form for an effective dielectric constant of 5.75×10^6 where the conductivity is 0.1 *S/m*. The situation for when the conductivity is 0.01 *S/m* is shown in Figure 5.1.2. The left-hand panel shows the comparison when the time step is $75\mu s$ where the difference would not be acceptable. The right-hand panel shows the comparison for a time step of $20\mu s$ where the difference would be acceptable. Determination of the appropriate effective dielectric constant depends upon the time-step chosen and the earth conductivity.

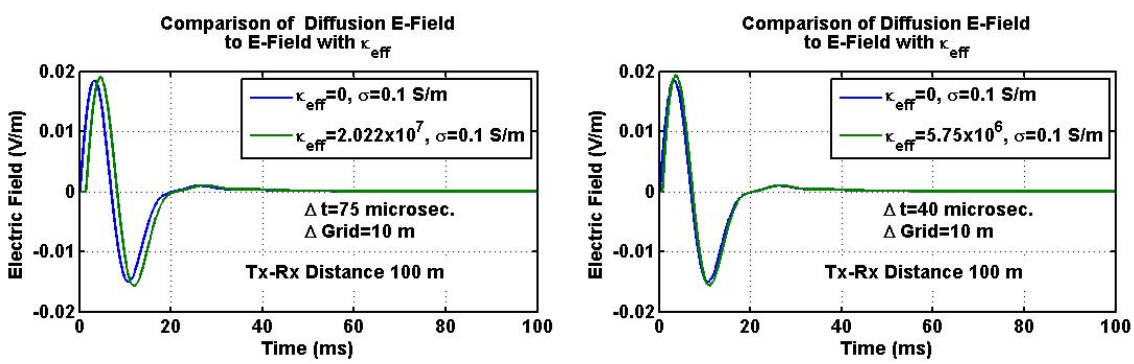

Figure 5.1.1: 1D solutions for the electric field for various fictitious dielectric constants and time steps $75\mu s$ left-hand panel and $40\mu s$ right-hand panel. Grid spacing is 10 *m*. The electrical conductivity is 0.1 *S/m*.

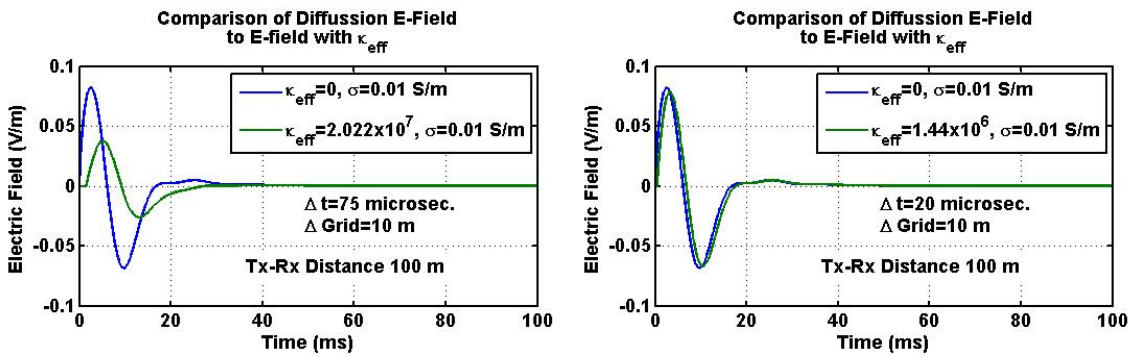

Figure 5.1.2: 1D solutions for the electric field for various fictitious dielectric constants and time steps $75\mu s$ left-hand panel and $20\mu s$ right-hand panel. Grid spacing is 10 *m*. The electrical conductivity is 0.01 *S*/*m*.

5.2 2D Seismo-Electric and Electro-Seismic

As part of this project, a 2D coupled acoustic poroelastic and EM algorithm has been developed, although all facets of the algorithm have not been entirely tested. At present, this 2D algorithm is for a layered media and requires sources and receivers to be located at grid nodes. The algorithm is second order in time derivatives and fourth order in spatial derivatives.

5.2.1 Governing Equations

Here the poroelastic equations, from Aldridge (2007), for an acoustic medium (no shear) are:

$$\begin{aligned}
&\left\{\left[1-\phi(\mathbf{x})\right]\bar{\rho}^{s}(\mathbf{x})+a(\mathbf{x})\right\}\frac{\partial \bar{v}_i^{s}(\mathbf{x},t)}{\partial t}-a(\mathbf{x})\frac{\partial \bar{v}_i^{f}(\mathbf{x},t)}{\partial t} \\
&\qquad = -\left[1-\phi(\mathbf{x})\right]\frac{\partial \bar{p}^{s}}{\partial x_i}-b(\mathbf{x})\left[\bar{v}_i^{s}(\mathbf{x},t)-\bar{v}_i^{f}(\mathbf{x},t)\right] \\
&\qquad\qquad +\left[1-\phi(\mathbf{x})\right]\bar{f}_i^{s}(\mathbf{x},t) \\
&-a(\mathbf{x})\frac{\partial \bar{v}_i^{s}(\mathbf{x},t)}{\partial t}+\left\{\phi(\mathbf{x})\bar{\rho}^{f}(\mathbf{x})+a(\mathbf{x})\right\}\frac{\partial \bar{v}_i^{f}(\mathbf{x},t)}{\partial t} \\
&\qquad = -\phi(\mathbf{x})\frac{\partial \bar{p}^{f}}{\partial x_i}+b(\mathbf{x})\left[\bar{v}_i^{s}(\mathbf{x},t)-\bar{v}_i^{f}(\mathbf{x},t)\right] \\
&\qquad\qquad +\phi(\mathbf{x})\bar{f}_i^{f}(\mathbf{x},t)
\end{aligned} \tag{5.2.1.1}$$

where ϕ is the porosity and the superscripts *s* and *f* refer to solid and fluid, respectively. The bar over the variable indicates a phase average. The $\overline{\mathbf{v}}^s, \overline{\mathbf{v}}^f$ are the solid and fluid particle velocities and the $\tilde{p}^s, \tilde{p}^f$ are the volume averaged solid and fluid pressures. The **f**'s are the body force sources. These sources include an active source and, as will be shown, a body force that comes from the coupling to the electric field. The terms involving the *a* and *b* coefficients are the inertial force (arising from volume averaging) and Rayleigh dissipation terms, respectively. We can rewrite the above equations in terms of Biot's (Biot, 1956) mass densities as

$$\begin{aligned}
&\rho_{11}(\mathbf{x})\frac{\partial \overline{v}_i^s(\mathbf{x},t)}{\partial t} - \rho_a(\mathbf{x})\frac{\partial \overline{v}_i^f(\mathbf{x},t)}{\partial t} \\
&\qquad = -[1-\phi(\mathbf{x})]\frac{\partial \overline{p}^s}{\partial x_i} - b(\mathbf{x})\left[\overline{v}_i^s(\mathbf{x},t) - \overline{v}_i^f(\mathbf{x},t)\right] \\
&\qquad\quad + [1-\phi(\mathbf{x})]\overline{f}_i^s(\mathbf{x},t) \\
&-\rho_a(\mathbf{x})\frac{\partial \overline{v}_i^s(\mathbf{x},t)}{\partial t} + \rho_{22}(\mathbf{x})\frac{\partial \overline{v}_i^f(\mathbf{x},t)}{\partial t} \\
&\qquad = -\phi(\mathbf{x})\frac{\partial \overline{p}^f}{\partial x_i} + b(\mathbf{x})\left[\overline{v}_i^s(\mathbf{x},t) - \overline{v}_i^f(\mathbf{x},t)\right] \\
&\qquad\quad + \phi(\mathbf{x})\overline{f}_i^f(\mathbf{x},t)
\end{aligned} \tag{5.2.1.2}$$

where

$$\begin{aligned}
\rho_{11} &= (1-\phi)\rho^s + \rho_a \\
\rho_{22} &= \phi\rho^f + \rho_a \\
\rho_a &= \rho^f (1-\phi)/2 \\
b &= \phi^2\eta/k
\end{aligned} \quad . \tag{5.2.1.3}$$

η is the fluid viscosity and *k* is the hydraulic permeability. We can solve the coupled equations [equation (5.2.1.2)] and get

$$\frac{\partial \bar{v}_i^s(\mathbf{x},t)}{\partial t} = \rho_{22}(\mathbf{x})\left\{(1-\phi)\frac{\partial \bar{p}^s}{\partial x_i} - b(\mathbf{x})\left[\bar{v}_i^s(\mathbf{x},t) - \bar{v}_i^f(\mathbf{x},t)\right] + (1-\phi)\bar{f}_i^s(\mathbf{x},t)\right\}\Big/ Den$$

$$+ \rho_a(\mathbf{x})\left\{-\phi\frac{\partial \bar{p}^f}{\partial x_i} + b(\mathbf{x})\left[\bar{v}_i^s(\mathbf{x},t) - \bar{v}_i^f(\mathbf{x},t)\right] + \phi\bar{f}_i^f(\mathbf{x},t)\right\}\Big/ Den$$

$$Den = \rho_{11}(\mathbf{x})\rho_{22}(\mathbf{x}) - \rho_a(\mathbf{x})^2 \tag{5.2.1.4}$$

$$\frac{\partial \bar{v}_i^f(\mathbf{x},t)}{\partial t} = \rho_{11}(\mathbf{x})\left\{-\phi\frac{\partial \bar{p}^f}{\partial x_i} + b(\mathbf{x})\left[\bar{v}_i^s(\mathbf{x},t) - \bar{v}_i^f(\mathbf{x},t)\right] + \phi\bar{f}_i^f(\mathbf{x},t)\right\}\Big/ Den$$

$$+ \rho_a(\mathbf{x})\left\{-(1-\phi)\frac{\partial \bar{p}^s}{\partial x_j} - b(\mathbf{x})\left[\bar{v}_i^s(\mathbf{x},t) - \bar{v}_i^f(\mathbf{x},t)\right] + (1-\phi)\bar{f}_i^s(\mathbf{x},t)\right\}\Big/ Den$$

The pressure equations are (Aldridge, 2007)

$$\frac{\partial \bar{p}^s(\mathbf{x},t)}{\partial t} = \left\{-P(\mathbf{x})\frac{\partial \bar{v}_k^s(\mathbf{x},t)}{\partial x_k} - Q(\mathbf{x})\frac{\partial \bar{v}_k^f(\mathbf{x},t)}{\partial x_k}\delta_{ij}\right\}\Big/(1-\phi) - \frac{1}{3}\frac{\partial \bar{m}_{ii}^{s-sym}(\mathbf{x},t)}{\partial t}$$

$$\frac{\partial \bar{p}^f(\mathbf{x},t)}{\partial t} = \left\{-Q(\mathbf{x})\frac{\partial \bar{v}_k^s(\mathbf{x},t)}{\partial x_k} - R(\mathbf{x})\frac{\partial \bar{v}_k^f(\mathbf{x},t)}{\partial x_k}\right\}\Big/\phi - \frac{1}{3}\frac{\partial \bar{m}_{kk}^{f-sym}(\mathbf{x},t)}{\partial t} \tag{5.2.1.5}$$

where terms involving the spatial derivative of the porosity have been neglected. The moduli are (Aldridge, 2007)

$$P = \frac{\phi(1-\alpha)\bar{K}^s\bar{K}^s + (1-\phi)(\alpha-\phi)\bar{K}^s\bar{K}^f}{\phi\bar{K}^s + (\alpha-\phi)\bar{K}^f}$$

$$Q = \frac{\phi(\alpha-\phi)\bar{K}^s\bar{K}^f}{\phi\bar{K}^s + (\alpha-\phi)\bar{K}^f} \tag{5.2.1.6}$$

$$R = \frac{\phi^2\bar{K}^s\bar{K}^f}{\phi\bar{K}^s + (\alpha-\phi)\bar{K}^f}$$

$$\alpha = 1 - \frac{K}{\bar{K}^s}$$

where K is the dry frame bulk modulus. The $\bar{K}$'s are average values of the bulk moduli. Here we used

$$\bar{K}^s = \left(V_p^s\right)^2\rho^s$$

$$\bar{K}^f = \left(V_p^f\right)^2\rho^f \tag{5.2.1.7}$$

Starting from Maxwell's equations we have for the phase averaged Faraday's equation

$$\mu \frac{\partial \hat{h}_i(\mathbf{x},t)}{\partial t} + \varepsilon_{ijk} \frac{\hat{e}_k(\mathbf{x},t)}{\partial x_j} = 0$$
$$\hat{h}_i = (1-\phi)h_i^s + \phi h_i^f \qquad (5.2.1.8)$$
$$\hat{e}_k = (1-\phi)e_k^s + \phi e_k^f$$

where $\hat{e}_k$ and $\hat{h}_i$ are the components of the composite or total electric and magnetic fields, respectively. For the so-called "curl **h**" equation we have from volume averaging

$$\varepsilon \frac{\partial \hat{e}_i(\mathbf{x},t)}{\partial t} - \varepsilon_{ijk} \frac{\partial \hat{h}_k(\mathbf{x},t)}{\partial x_j} + \sigma(\mathbf{x})\hat{e}_i(\mathbf{x},t) = -\hat{j}_i^{source}(\mathbf{x},t)$$
$$+ L_{21}\left[\phi \frac{\partial \overline{p}^f(\mathbf{x},t)}{\partial x_i} + \int_{S_w} dS' n_i^f \, p^f(\mathbf{x}',t)\Gamma\left(\frac{\mathbf{x}-\mathbf{x}'}{\Delta}\right)\right] \qquad (5.2.1.9)$$

ε is the electric permittivity obtained through volume averaging, σ is the bulk electrical conductivity, and ϕ is the porosity. In the above equations and the following equations the spatial dependence of ϕ is suppressed. The function $\Gamma(\mathbf{x}-\mathbf{x}'/\Delta)$ is an averaging filter, which can be thought of as a product of Heaviside step functions (DesJardin, *et al.*, 2001). The source term for the electric field (right-hand-side of equation (5.2.1.9)) contains two terms $\hat{j}^{source}$ from "real" impressed currents and the electrokinetic source term (discussed below) where the gradient of the fluid pressure gives rise to an electrical current. From the volume averaging of the pressure gradient we have

$$L_{21}\left[\phi \frac{\partial \overline{p}^f(\mathbf{x},t)}{\partial x_i} + \int_{S_w} dS' n_i^f \, p^f(\mathbf{x}',t)\Gamma\left(\frac{\mathbf{x}-\mathbf{x}'}{\Delta}\right)\right]. \qquad (5.2.1.9a)$$

The surface integral gives rise to a term much like the $a(\mathbf{x})$ term in equation (5.2.1.9); *i.e.*, this is an inertial force term (Geerits, 1996). We will neglect this term as being small since it is multiplied by a parameter on the order of 10^{-9} or less.

Now if we include the seismic and electromagnetic coupling (SE or ES) we have terms involving fluid and electrical current flow (Moore, *et al*, 2004). In the fluid filled pores the fluid and current flows are given by

$$\mathbf{q}^f(\mathbf{x},t) = -L_{11}(\mathbf{x})\nabla p^f(\mathbf{x},t) + L_{12}(\mathbf{x})\mathbf{e}^f(\mathbf{x},t)$$
$$\mathbf{j}^f(\mathbf{x},t) = -L_{21}(\mathbf{x})\nabla p^f(\mathbf{x},t) + L_{22}(\mathbf{x})\mathbf{e}^f(\mathbf{x},t) \qquad (5.2.1.10)$$

where $\mathbf{q}^f$ is the volumetric fluid flow units of (*meters*/*second*)
$\mathbf{j}^f$ is the electric current density $(amperes/meter^2)$
$p^f(\mathbf{x},t)$ is the fluid pressure $(newtons/meter^2)$

$L_{11} = k/\eta^f$ hydraulic permeability divided by fluid viscosity

$L_{22} = \sigma^f$ the electrical conductivity of the fluid

$L_{12} = L_{21} = -\dfrac{\varepsilon^f \varsigma}{\eta^f F}$, (Onsager reciprocity) where ς is the zeta potential (which depends upon the salinity and pH of the pore water as well as other fluid and rock properties), F is the electrical formation factor (a pore topology term) and was defined in Section 2.0, and ε^f is the electrical permittivity of the pore fluid. It is noteworthy that Deckman, *etal*., (2005) measured a distinct difference in L_{12} and L_{21}.

The current flow term $-\left(\varepsilon^f \varsigma / \eta^f F\right)\nabla p^f$ is added to the total current that produces an electric field. Thus the pressure gradient term acts as a sourcing mechanism for the electric field and produces an electric field in the direction of the gradient. If there is no fluid flow, from equation (5.2.1.10) we have, following Neev and Yeatts, (1989)

$$\begin{aligned} \mathbf{q} &= -L_{11}\nabla p^f + L_{12}\mathbf{e}^f = 0 \\ \nabla p^f &= \frac{L_{12}}{L_{11}}\mathbf{e}^f = -\frac{\varepsilon^f \varsigma}{kF}\mathbf{e}^f \end{aligned} \qquad (5.2.1.11)$$

The pressure gradient term in equation (5.2.1.11) is a body force term and the coefficients multiplying the electric field have the units *coulombs*/m^3. In the fluid-filled pores, we have a body force source term that is due to the electrokinetic effect. Upon volume averaging, the body force term for the poroelastic equations arising from electrokinetic effects is

$$\frac{\partial \overline{p}^f}{\partial x_i} = -\frac{L_{12}}{L_{11}}\overline{e}_i^f = -\frac{L_{12}}{\phi L_{11} F}\hat{e}_i = \frac{\varepsilon^f \varsigma}{\phi k F^2}\hat{e}_i \qquad (5.2.1.12)$$

where $\hat{e}_i = \phi F \overline{e}_i^f$. Thus the body force acting in the fluid is

$$\tilde{f}_i^f(\mathbf{x},t) = \phi \frac{\varepsilon^f \varsigma}{\phi k F^2}\hat{e}(\mathbf{x},t) = \frac{\varepsilon^f \varsigma}{k F^2}\hat{e}(\mathbf{x},t) \qquad (5.2.1.13)$$

and is the direction of the electric field. There is no body force acting in the solid from the electrokinetic effects except as exerted by the fluid. It is note worthy that as the formation factor increases (porosity decreases) the force term gets smaller and as the hydraulic permeability k increases the force term gets smaller as well.

In summary, the coupled equations of motion for the seismo-electric and electro-seismic are

$$\frac{\partial \bar{v}_i^s(\mathbf{x},t)}{\partial t} = \rho_{22}(\mathbf{x})\left\{-\frac{\partial \tilde{p}^s}{\partial x_i} - b(\mathbf{x})\left[\bar{v}_i^s(\mathbf{x},t) - \bar{v}_i^f(\mathbf{x},t)\right] + \tilde{f}_i^s(\mathbf{x},t)\right\}\Big/ Den$$

$$+ \rho_a(\mathbf{x})\left\{-\frac{\partial \tilde{p}^f}{\partial x_i} + b(\mathbf{x})\left[\bar{v}_i^s(\mathbf{x},t) - \bar{v}_i^f(\mathbf{x},t)\right] + \tilde{f}_i^f(\mathbf{x},t) + \frac{\varepsilon^f \varsigma}{kF^2}\hat{e}_i(\mathbf{x},t)\right\}\Big/ Den$$

$$Den = \rho_{11}(\mathbf{x})\rho_{22}(\mathbf{x}) - \rho_a(\mathbf{x})^2$$

$$\frac{\partial \bar{v}_i^f(\mathbf{x},t)}{\partial t} = \rho_{11}(\mathbf{x})\left\{-\frac{\partial \tilde{p}^f}{\partial x_i} + b(\mathbf{x})\left[\bar{v}_i^s(\mathbf{x},t) - \bar{v}_i^f(\mathbf{x},t)\right] + \tilde{f}_i^f(\mathbf{x},t) + \frac{\varepsilon^f \varsigma}{kF^2}\hat{e}_i(\mathbf{x},t)\right\}\Big/ Den$$

$$+ \rho_a(\mathbf{x})\left\{\frac{\partial \tilde{\sigma}_{ij}^s}{\partial x_j} - b(\mathbf{x})\left[\bar{v}_i^s(\mathbf{x},t) - \bar{v}_i^f(\mathbf{x},t)\right] + \tilde{f}_i^s(\mathbf{x},t)\right\}\Big/ Den$$

(5.2.1.14a)

$$\frac{\partial \tilde{p}^s(\mathbf{x},t)}{\partial t} = -P(\mathbf{x})\frac{\partial \bar{v}_k^s(\mathbf{x},t)}{\partial x_k} - Q(\mathbf{x})\frac{\partial \bar{v}_k^f(\mathbf{x},t)}{\partial x_k}\delta_{ij} - \frac{1}{3}\frac{\partial \hat{m}_{ii}^{s-sym}(\mathbf{x},t)}{\partial t}$$

$$\frac{\partial \tilde{p}^f(\mathbf{x},t)}{\partial t} = -Q(\mathbf{x})\frac{\partial \bar{v}_k^s(\mathbf{x},t)}{\partial x_k} - R(\mathbf{x})\frac{\partial \bar{v}_k^f(\mathbf{x},t)}{\partial x_k} - \frac{1}{3}\frac{\partial m_{kk}^{f-sym}(\mathbf{x},t)}{\partial t}$$

(5.2.1.14b)

$$\varepsilon\frac{\partial \hat{e}_i(\mathbf{x},t)}{\partial t} - \varepsilon_{ijk}\frac{\partial \hat{h}_k(\mathbf{x},t)}{\partial x_j} + \sigma(\mathbf{x})\hat{e}_i(\mathbf{x},t) = -\hat{j}_i^{source}(\mathbf{x},t) + L_{21}\phi\frac{\partial \bar{p}^f(\mathbf{x},t)}{\partial x_i}$$

$$\mu\frac{\partial \hat{h}_i(\mathbf{x},t)}{\partial t} + \varepsilon_{ijk}\frac{\partial \hat{e}_k(\mathbf{x},t)}{\partial x_j} = 0$$

(5.2.1.15)

We shall restrict the solutions to two dimensions. For the poroacoustic equations, we will solve for $\bar{v}_x^s$, $\bar{v}_z^s$, $\bar{v}_x^f$, $\bar{v}_z^f$, $\tilde{p}^s$, $\tilde{p}^f$ and for the EM equations we will solve for $\hat{e}_x$, $\hat{e}_z$, $\hat{h}_y$.

5.2.2 Finite-Difference Solutions

The finite-difference solutions we used for the poroacoustic equations are similar to those of Aldridge (2007). We have from equation (5.2.1.14) updating from time t_n to t_{n+1} at grid node i,j (here we suppress the node point)

$$\bar{v}_i^{s\,n+1} = \Delta t \left\langle \begin{array}{l} \rho_{22}\left\{ -\dfrac{\partial \tilde{p}^{s\,n}}{\partial x_i} - b\left[\bar{v}_i^{s\,n} - \bar{v}_i^{f\,n}\right] + \tilde{f}_i^{s\,n} \right\} \Big/ Den \\ \quad + \rho_a \left\{ -\dfrac{\partial \tilde{p}^{f\,n}}{\partial x_i} + b\left[\bar{v}_i^{s\,n} - \bar{v}_i^{f\,n}\right] + \tilde{f}_i^{f\,n} + \dfrac{\varepsilon^f \varsigma}{kF^2}\hat{e}_i^{\,n} \right\} \Big/ Den \end{array} \right\rangle$$

$$Den = \rho_{11}\rho_{22} - \rho_a^{\,2}$$

$$\bar{v}_i^{f\,n+1} = \Delta t \left\langle \begin{array}{l} \rho_{11}\left\{ -\dfrac{\partial \tilde{p}^{f\,n}}{\partial x_i} + b\left[\bar{v}_i^{s\,n} - \bar{v}_i^{f\,n}\right] + \tilde{f}_i^{f\,n} \right\} \Big/ Den \\ \quad + \rho_a \left\{ -\dfrac{\partial \tilde{p}^{s\,n}}{\partial x_j} - b\left[\bar{v}_i^{s\,n} - \bar{v}_i^{f\,n}\right] + \tilde{f}_i^{s\,n} + \dfrac{\varepsilon^f \varsigma}{kF^2}\hat{e}_i^{\,n} \right\} \Big/ Den \end{array} \right\rangle \tag{5.2.2.1}$$

$$\begin{aligned} \tilde{p}^{s\,n+1} &= \tilde{p}^{s\,n} + \Delta t\left\{ -P\frac{\partial \bar{v}_k^{s\,n}}{\partial x_k} - Q\frac{\partial \bar{v}_k^{f\,n}}{\partial x_k}\delta_{ij} - \frac{1}{3}\frac{\partial \hat{m}_{ii}^{s-sym\,n}}{\partial t} \right\} \\ \tilde{p}^{f\,n+1} &= \tilde{p}^{f\,n} + \Delta t\left\{ -Q\frac{\partial \bar{v}_k^{s\,n}}{\partial x_k} - R\frac{\partial \bar{v}_k^{f\,n}}{\partial x_k} - \frac{1}{3}\frac{\partial m_{kk}^{f-sym\,n}}{\partial t} \right\} \end{aligned} \tag{5.2.2.2}$$

If one applied the finite-difference to the electric field equation [equation (5.2.1.15)], the solutions become unstable when the conductivity term is included. Furthermore, the time steps required would be exceeding small, sub micro-seconds. In this work we are interested in a finite electrical conductivity and our interest lies in what is called the induction limit or diffusion limit. In this report, a modified form of the Du Fort-Frankel method (Du Fort and Frankel 1953) to time step the electric field in equation (5..2.1.15) as outlined by Wang and Hohmann (1993). The essence of the Du Fort-Frankel method is the implicit introduction of a hyperbolic term to the parabolic equations. All that is needed is to keep the velocity of the fictitious wavefield to be no slower than the diffusion wavefield in the induction limit. The velocity of the fictitious wavefield is governed by replacing the electric permittivity by a fictitious electric permittivity γ. For the electric field equation (5.2.1.15) becomes

$$\gamma \frac{\partial e_i(\mathbf{x},t)}{\partial t} - \varepsilon_{ijk} \frac{\partial h_k(\mathbf{x},t)}{\partial x_j} + \sigma(\mathbf{x}) e_i(\mathbf{x},t) = -j_i^{source}(\mathbf{x},t) + L_{21}\phi \frac{\partial \overline{p}^f(\mathbf{x},t)}{\partial x_i}$$

$$\gamma \left[\frac{e_i^{n+1} - e_i^n}{\Delta t} \right] + \sigma \left(\frac{e_i^{n+1} + e_i^n}{2} \right) = \varepsilon_{ijk} \frac{\partial h_k(\mathbf{x},t)}{\partial x_j} - j_i^{source}(\mathbf{x},t) + L_{21}\phi \frac{\partial \overline{p}^f(\mathbf{x},t)}{\partial x_i}$$

$$2\gamma \left[e_i^{n+1} - e_i^n \right] + \Delta t \sigma \left[e_i^{n+1} + e_i^n \right] = 2\Delta t \left[\varepsilon_{ijk} \frac{\partial h_k(\mathbf{x},t)}{\partial x_j} + L_{21}\phi \frac{\partial \overline{p}^f(\mathbf{x},t)}{\partial x_i} - j_i^{source}(\mathbf{x},t) \right]$$

$$\left[2\gamma + \Delta t \sigma \right] e_i^{n+1} - \left[2\gamma - \Delta t \sigma \right] e_i^n = 2\Delta t \left[\varepsilon_{ijk} \frac{\partial h_k(\mathbf{x},t)}{\partial x_j} + L_{21}\phi \frac{\partial \overline{p}^f(\mathbf{x},t)}{\partial x_i} - j_i^{source}(\mathbf{x},t) \right]$$

$$e_i^{n+1} = \left[\frac{2\gamma - \Delta t \sigma}{2\gamma + \Delta t \sigma} \right] e_i^n + \frac{2\Delta t}{\left[2\gamma + \Delta t \sigma \right]} \left[\varepsilon_{ijk} \frac{\partial h_k(\mathbf{x},t)}{\partial x_j} + L_{21}\phi \frac{\partial \overline{p}^f(\mathbf{x},t)}{\partial x_i} - j_i^{source}(\mathbf{x},t) \right] \tag{5.2.2.3}$$

The fictitious wave speed can be determined by solving Maxwell's equations in the frequency domain. From Maxwell's equations,

$$\begin{aligned} \varepsilon_{ijk} \frac{e_k(\mathbf{x},t)}{\partial x_j} &= -\mu_0 \frac{h_i(\mathbf{x},t)}{\partial t} \\ \varepsilon_{ijk} \frac{\partial h_k(\mathbf{x},t)}{\partial x_j} &= \varepsilon \frac{e_i(\mathbf{x},t)}{\partial t} + \sigma\, e_i(\mathbf{x},t) + j_i(\mathbf{x},t) \end{aligned} \tag{5.2.2.4}$$

where we assume the electric permittivity ε is independent of time, but may have spatial variations. Here μ_0 is the magnetic permeability of free space and has the value of $\mu_0 = 4\pi \times 10^{-7}\ henries/m$. ε is the electric permittivity and is given by $\varepsilon = \kappa \varepsilon_0$ where κ is the dielectric constant and $\varepsilon_0 = 8.854 \times 10^{-12}\ farads/m$ the electrical permittivity of free space. Taking the time derivative of the second equation in equation (5.2.2.4) and combining the two equations

$$\begin{aligned} \varepsilon\mu_0 \frac{\partial^2 e_i(\mathbf{x},t)}{\partial t^2} + \sigma\, \mu_0\, e_i(\mathbf{x},t) - \varepsilon_{ijk}\varepsilon_{k\ell m} \frac{e_m(\mathbf{x},t)}{\partial x_j \partial x_\ell} &= -\mu_0\, j_i(\mathbf{x},t) \\ \varepsilon\mu_0 \frac{\partial^2 e_i(\mathbf{x},t)}{\partial t^2} + \sigma\, \mu_0\, e_i(\mathbf{x},t) - \nabla^2 e_i(\mathbf{x},t) &= -\mu_0\, j_i(\mathbf{x},t) \end{aligned} \tag{5.2.2.5}$$

where we assume $\nabla \cdot \mathbf{e} = 0$. (For 1D plane-wave solutions the divergence of the electric field is zero.) For solutions a time dependence of $exp(i\omega t)$ is assumed. We have for a frequency domain solution

$$\frac{-\omega^2}{c^2}\mathbf{E}(\mathbf{x},\omega)+i\omega\sigma\mu_0\mathbf{E}(\mathbf{x},\omega)-\nabla^2\mathbf{E}(\mathbf{x},\omega)=-\mu_0\mathbf{J}(\mathbf{x},\omega)$$
$$c=\frac{1}{\sqrt{\mu_0\kappa\varepsilon_0}} \qquad (5.2.2.6)$$

In equation (5.2.2.6), c is the EM wave speed in the particular medium characterized by κ. In free space $\kappa=1$ and $\sigma=0$ giving $c=3\times10^8\ m/s$. Rewriting equation (5.2.2.6)

$$-\gamma\omega^2\mathbf{E}(\mathbf{x},\omega)+i\omega\sigma\mathbf{E}(\mathbf{x},\omega)-\frac{1}{\mu_0}\nabla^2\mathbf{E}(\mathbf{x},\omega)=-\mathbf{J}(\mathbf{x},\omega) \qquad (5.2.2.7)$$

where γ is an effective electric permittivity with an associate wave speed of

$$c_{eff}=\frac{1}{\sqrt{\mu_0\gamma}}=\frac{1}{\sqrt{\mu_0\kappa_{eff}\varepsilon_0}} \qquad (5.2.2.8)$$

In the finite-difference approximation, the CFL criterion for 2D is

$$\Delta t\le\frac{\Delta x}{\sqrt{2}\ c_{eff}}$$
$$\le\frac{\Delta x\,\mu_0\gamma}{\sqrt{2}} \qquad (5.2.2.9)$$

Giving a lower limit on γ of

$$\gamma\ge\frac{2}{\mu_0}\left(\frac{\Delta t}{\Delta x}\right)^2 \qquad (5.2.2.10)$$

Note that this γ is different than that given by equation (5.1.1) for 3D calculations. Experience has shown that solutions go unstable when the equality holds in equation (5.2.2.10). One needs to multiply this minimum value by a factor ≥ 2 in order to maintain stability. For example, stable solutions are obtained for $\Delta t=0.025\,ms$ and $\Delta x=10\,m$ that gives $\gamma=1.99\times10^{-5}$ when the inequality, equation (5.2.2.10), is multiplied by 2. The associated effective dielectric constant is $\kappa_{eff}=2.25\times10^6$. Figure 5.2.2.1 compares the 1D analytic solutions for electric and magnetic fields in the induction limit, $\kappa_{eff}=0$, to the solutions with $\kappa_{eff}=2.25\times10^6$ where the conductivity is 0.1 *S*/*m*. There is excellent agreement between the two solutions. Figure 5.2.2.2 shows the comparison when the conductivity is 0.001 *S*/*m*. Besides the peak in the electric field being off, the magnitude with the fictitious dielectric constant is about half as the induction limit. However, for the magnetic field, the agreement is excellent. Since we

are interested in the electric field in the SE and ES effects, we must use a time step small enough or grid spacing large enough such that there would be agreement between the two solutions. Figure 5.2.2.3 shows the comparison for a time step of 0.01 *ms* where acceptable agreement for the electric field is obtained by increasing κ_{eff} .to 3.6×10^5.

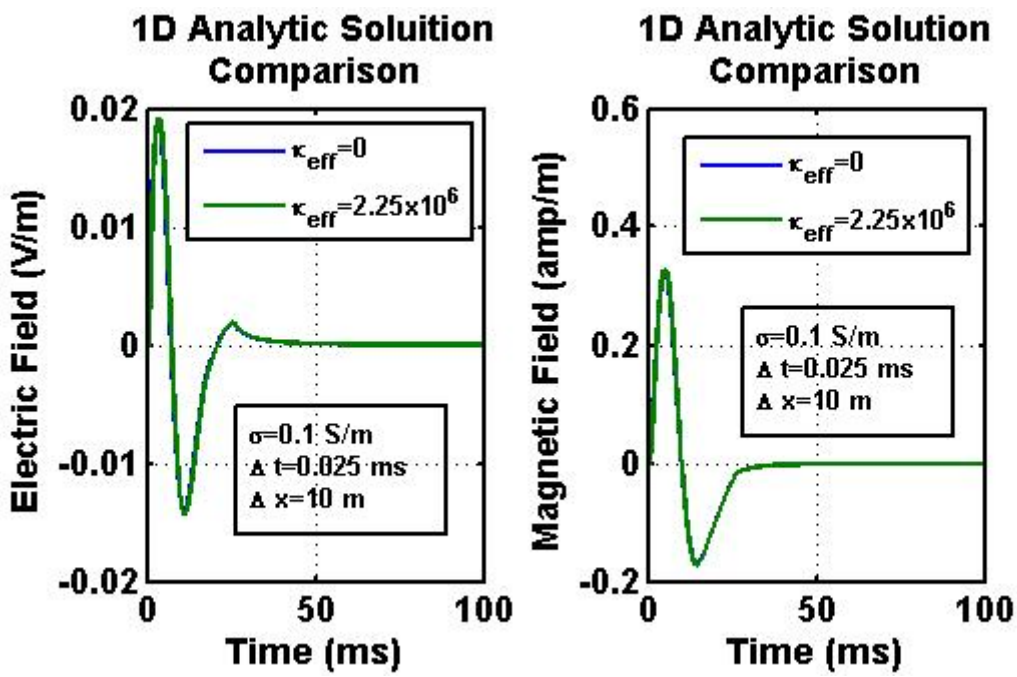

Figure 5.2.2.1: 1D analytic solutions for the electric and magnetic fields. Comparison of the induction limit solution, $\kappa_{eff} = 0$, and for $\kappa_{eff} = 2.25\times10^6$ in a medium with a conductivity of 0.1 *S/m*. Time step 0.025 *ms*, grid spacing 10 *m*.

For seismic data the spatial grid spacing Δx is governed by

$$\Delta x = \frac{V_{slowest}}{5\, f_{max}} \qquad (5.2.2.11)$$

where $V_{slowest}$ is the slowest wave speed in the earth model and f_{max} is the frequency at which spectrum of the input wavelet is at 1% of the maximum value. Equation (5.2.2.11) gives the grid spacing such that there are five wavelengths within the grid for frequencies less than f_{max}. The time step is given by

$$\Delta t = \frac{\Delta x}{\sqrt{3}\, V_{fastest}} \qquad (5.2.2.12)$$

where $V_{fastest}$ is the fastest wave speed in the model and Δx is calculated using equation (5.2.2.11). For example, if the slowest and fasted wave speeds are 1500 *m*/s and 2500 *m*/*s* with a f_{max} of 150 *Hz*, then equations (5.2.2.11) and (5.2.2.12) give $\Delta x = 2.0\, m$ and

$\Delta t = 0.046\,ms$. Figure 5.2.2.4 (left-hand panel) shows the electric field for a time step of 0.01 *ms* and a grid spacing of 2 *m*. Note the severe disagreement. The right-hand panel shows the comparison for a time step of 0.001 *ms* again a spatial grid of 2 m.

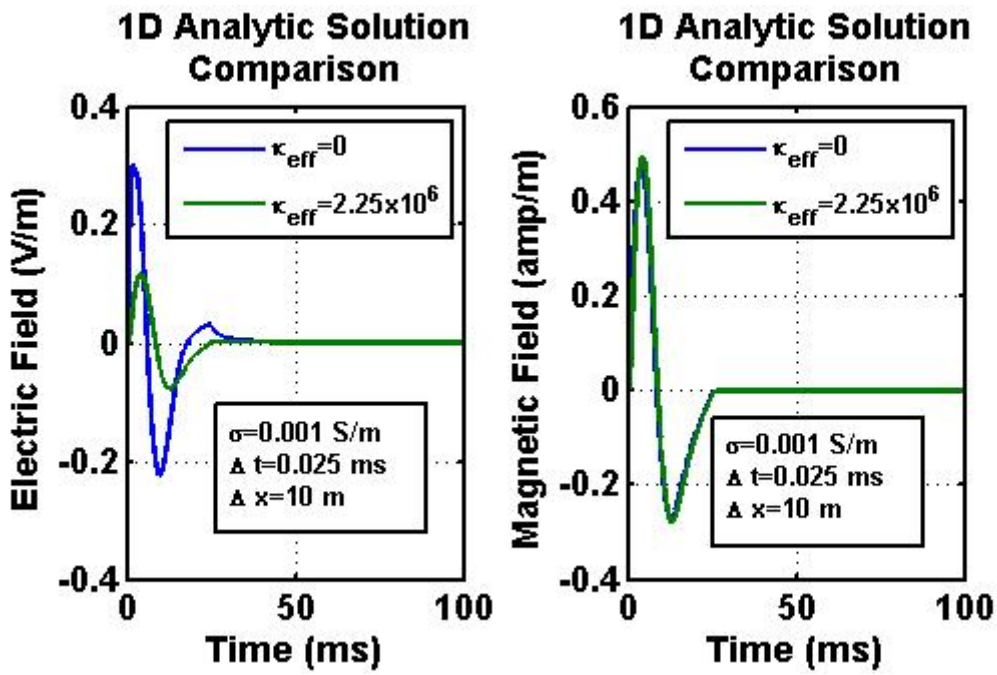

Figure 5.2.2.2: 1D analytic solutions for the electric and magnetic fields. Comparison of the induction limit solution, $\kappa_{eff} = 0$, and for $\kappa_{eff} = 2.25 \times 10^6$ in a medium with a conductivity of 0.001 *S/m*. Time step 0.01 *ms*, grid spacing 10 *m*.

Figure 5.2.2.4 points out that to put the poroacoustic and EM on the same spatial scales, the time step would be on the order of a microsecond, leading to one million iterations for a trace length of one second. From Figures 5.2.2.3 and 5.2.2.4 it is clear that by increasing the size of the EM spatial grid to 10 m, the time step is 0.01 *ms*, which is smaller than the seismic time step of 0.046 ms for this example.

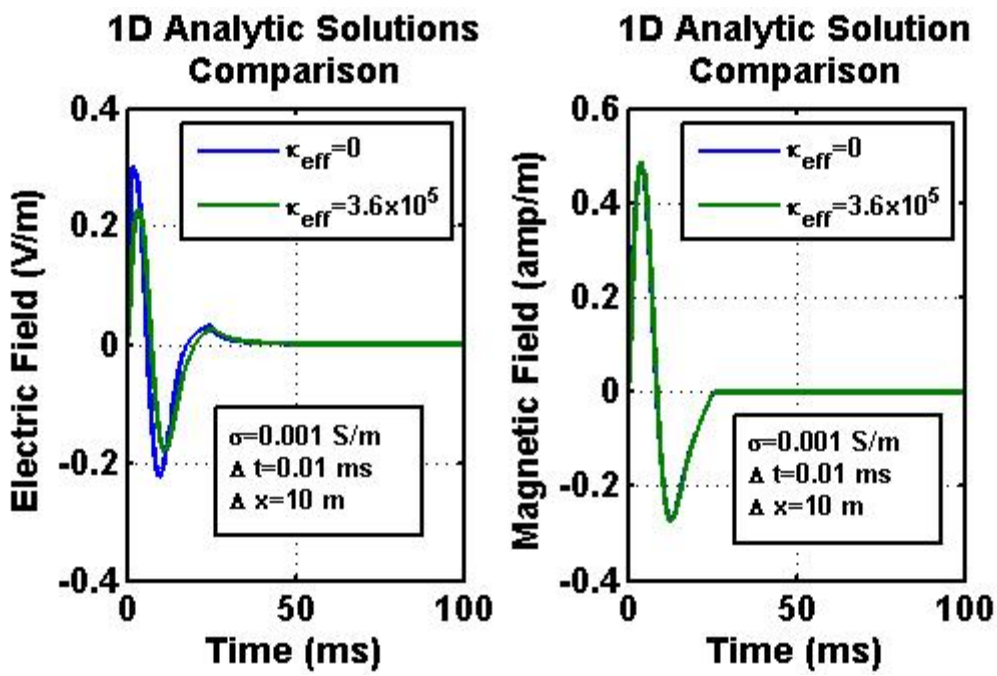

Figure 5.2.2.3: 1D analytic solutions for the electric and magnetic fields. Comparison of the induction limit solution, $\kappa_{eff} = 0$, and for $\kappa_{eff} = 3.6\times10^5$ in a medium with a conductivity of 0.001 *S/m*. Time step 0.01 *ms*, grid spacing 10 *m*.

The coupling terms between the poroacoustic equations (5.2.2.1 and 5.2.2.2) and the EM equations (5.2.2.3) requires that the electric field be known on the seismic grid and the pressure gradient be known on the EM grid. In the time-stepping algorithm, the electric field is interpolated onto the seismic grid and the pressure is interpolated onto the EM grid before the gradient is taken. However, when different time steps are used between the seismic and EM finite-difference algorithms, the interpolation must be made onto the EM grid at the appropriate EM time. For example, if the seismic time step is 0.1 *ms* and the EM time step is 0.01 *ms*, then there are 10 EM time steps between seismic times t_n and t_{n+1}. The solid and fluid pressures using their values at t_n are time stepped to t_{n+1}. The electric field has been calculated at t_n . This electric field is interpolated onto the seismic grid to provide a body force term. The pressure is interpolated onto the EM grid at times t_n+dt_{em}, $t_n+2dt^{em}+\ldots t_{n+1}$. Then the EM fields are then calculated between the times $_{tn}$ and t_{n+1} using the appropriate pressure gradients. This methodology has been checked against using a single time step with different spatial grids and found to be in complete agreement.

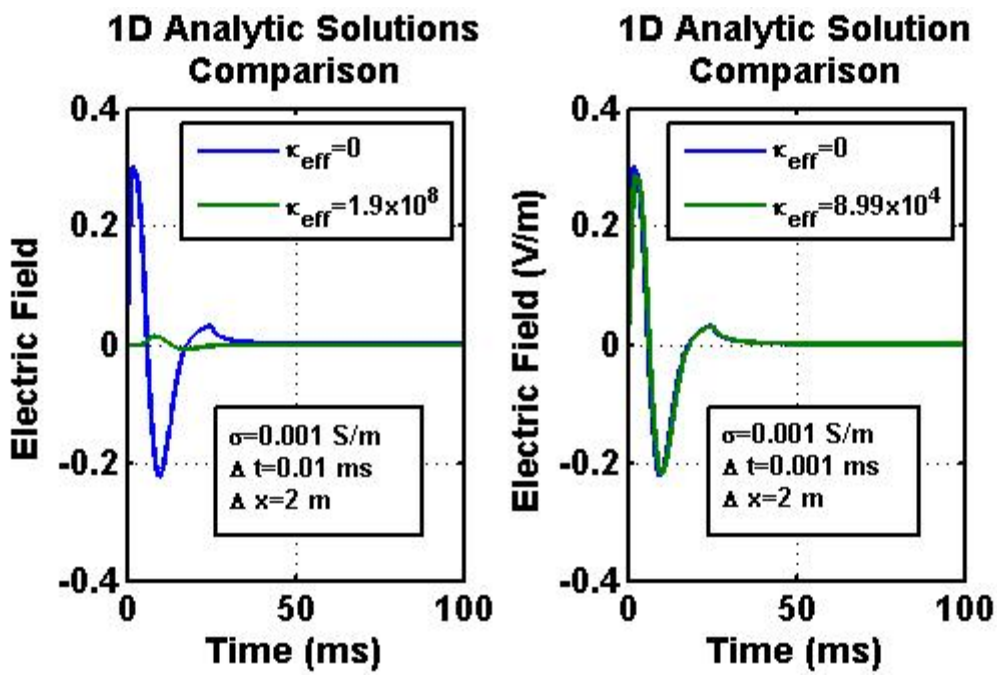

Figure 5.2.2.4: 1D analytic solutions for the electric and magnetic fields. Comparison of the induction limit solution, $\kappa_{eff} = 0$, and for $\kappa_{eff} = 1.9 \times 10^8$, $\Delta t = 0.01 ms$ (left-hand panel) and the induction limit, $\kappa_{eff} = 0$, and for $\kappa_{eff} = 8.99 \times 10^4$, $\Delta t = 0.001 ms$. Both panels are for a medium with a conductivity of 0.001 *S/m*. The spatial grid was 2 *m* for both panels.

For both the seismic and EM grids we use a simple sponge at the grid boundaries. Using 20 grid nodes for the seismic grid where a 5% attenuation at each node as the wave traverses the sponge boundary does a reasonable job of suppressing grid boundary reflections. For the EM grid, 5 nodes with a 2% attenuation does a reasonable job of suppressing the grid boundary reflections.

The air-earth interface for the poroacoustic part of the algorithm is treated as a stress-free surface by forcing the solid and fluid pressures to be zero for nodes above the air-earth interface. For the EM grid, we have only one node above the air-earth interface. Depending upon the seismic and EM grid spacings, there are several seismic nodes above the interface.

The EM boundary conditions are that the tangential components of the electric and magnetic fields are continuous. For the finite difference grid, $\hat{e}_x$ and $\hat{e}_z$ lie on the elemental grid boundaries and $\hat{h}_y$ lies on the elemental grid face. Since $\hat{e}_x$ and $\hat{h}_y$ are continuous, we linearly extrapolate the values at the surface to one node above the earth. Thus

$$\hat{e}_x(i,1) = 2\hat{e}_x(i,2) - \hat{e}_x(i,3)$$
$$\hat{h}_y(i+1/2,1/2) = 2\hat{h}_y(i+1/2,3/2) - \hat{h}_y(i+1/2,5/2) \qquad (5.2.2.13)$$

where i is the x-direction index. The z-component of the electric field, $\hat{e}_z$ is not necessarily continuous. We will follow the treatment by Wang and Hohmann (1993) for their 3D algorithm for the upward continuation of $\hat{b}_z$. If we assume that there are no charge density in the air, then the divergence and the Laplacian of the electric field are zero in the air. From Appendix C we have

$$\hat{e}_z(\mathbf{x}) = -\int dS' g(\mathbf{x},\mathbf{x}')\partial_{z'}\hat{e}_z(\mathbf{x}') = \int dS' g(\mathbf{x},\mathbf{x}')\partial_x \hat{e}_x(\mathbf{x}')$$
$$\hat{e}_z(\mathbf{x}) = \int dx' \frac{1}{2\pi}\int dk_x \left.\frac{e^{-k_x|z-z'|}}{k_x}\right|_{z'=0} e^{ik_x(x-x')} \frac{1}{2\pi}\int dk'_x ik'_x E_x(k'_x, z'=0)e^{ik'_x x'}$$
$$\frac{1}{2\pi}\int dk_x E_z(k_x,z)e^{ik_x x} = \frac{1}{2\pi}\int dk_x \frac{e^{-k_x|z|}}{k_x} ik_x E_x(k_x, z'=0)e^{ik_x x} \qquad (5.2.2.14)$$
$$E_z(k_x,z) = ie^{-k_x|z|}E_x(k_x,z'=0)$$
$$\hat{e}_z(i,1/2) = \frac{1}{2\pi}\int dk_x E_z(k_x,z)e^{ik_x x} = i\frac{1}{2\pi}\int dk_x E_x(k_x,z=0)e^{ik_x x}$$

where $E_x(k_x, z=0)$ is the spatial Fourier transform of $\hat{e}_x$ at the earth's surface. Note, this air-earth interface part of the 2D algorithm is not fully operational at this time.

5.2.3 Electrical Conductivity Model Building

An experimental relationship exists between the pore water resistivity (reciprocal of the electrical conductivity) and the electrical resistivity that would be measured by an electric/EM log or using surface electric/EM methods. Usually, this is given by some form of Archie's law and is often written as

$$\rho_a = \frac{a\rho_f}{\phi^m S_w^n}, \qquad (5.2.3.1)$$

where ρ_a is the apparent resistivity, ρ^f is the pore water resistivity, ϕ is the porosity, S_w is the water saturation, m and n are on the order of 2, and a is a constant on the order 1. For electric/EM well logging, the formation factor F is defined as,

$$F = \frac{\rho_a}{\rho_f}. \qquad (5.2.3.2)$$

Depending upon whether one uses Archie's law or some other relationship, the formation factors for 100 percent saturation is given by (from Gearhart-Owen Formation Evaluation Data Handbook)

$$\begin{aligned} F &= \phi^{-m}, \quad Archie \\ &= 0.62/\phi^{2.15}, \quad Humble. \\ &= a/\phi^{m}, \quad General \end{aligned} \tag{5.2.3.3}$$

The so-called cementation exponent *m* models how much the pore network increases the resistivity. The rock itself is assumed to be non-conductive. If the pore network were to be modeled as a set of parallel capillary tubes, a cross-section average of the rock's resistivity would yield porosity dependence equivalent to a cementation exponent of 1; *i.e.*, straight through current flow. The tortuosity (actual flow path divided by the straight line distance) of the rock will increase this to a higher number than 1. The cementation exponent is related to the tortuosity and the permeability. Increasing the permeability (lowering the tortuosity) would in effect decrease the cementation exponent *m*. Unconsolidated sands cementation factor *m* has been observed to be near 1.3; where as, common values for consolidated sandstones are $1.8 < m < 2.0$. Figure 5.2.3.1 shows representative plots of the porosity ϕ as a function of formation factor *F*. The Humble model was experimentally determined for certain Oklahoma oil-bearing sandstones.

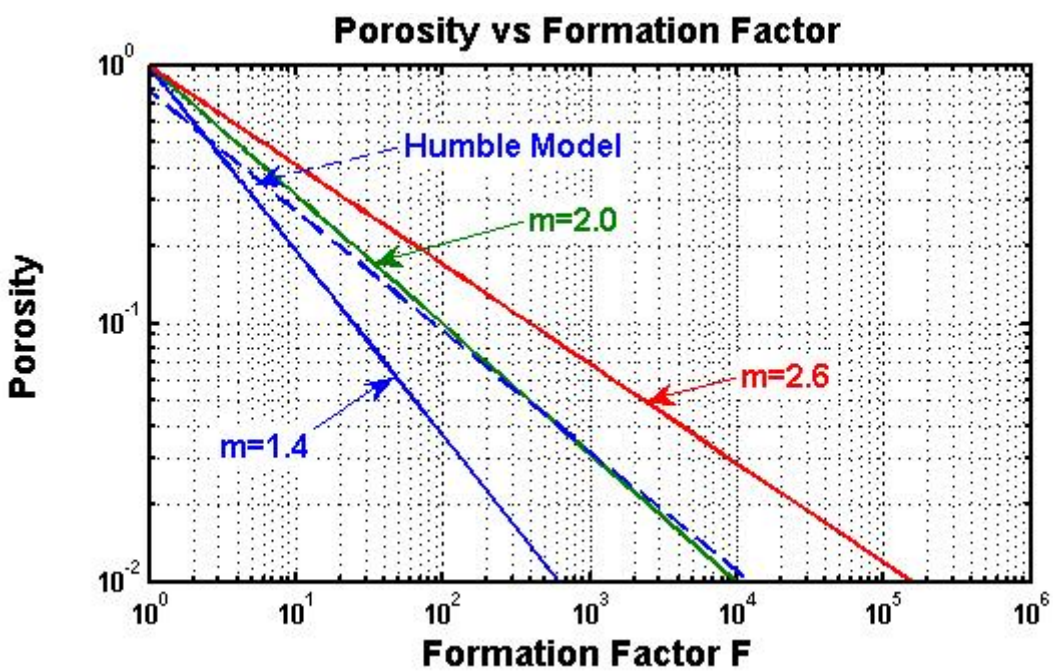

Figure 5.2.3.1: Porosity as a function of formation factor for various models. Here m is the cementation factor where the formation factor $F = \phi^{-m}$. The Humble model is $F = 0.62\phi^{-2.15}$.

From equation (5.2.3.3) the relationship for the electrical conductivity is

$$F = \frac{\sigma_f}{\sigma_a}, \tag{5.2.3.4}$$

where σ_f is the pore water conductivity and σ_a is the apparent conductivity or composite conductivity.

For the water salinity project, the interest lies in NaCl concentrations less that approximately 2000 *ppm*. This limit is "imposed" by present economical technologies. From the Figure 5.2.3.2, this suggests interest in pore water resistivities of greater than approximately $3.4\,\Omega \cdot m$ corresponding to a conductivity of $0.29\,S/m$ for a water temperature of 50 deg. *F*. On the other end of the spectrum, a 100 *ppm* of NaCl corresponds to a conductivity of approximately 0.017 *S*/*m*. For reference, sea water on average has a salinity of 3.5% or 35 parts per thousand yielding 35000 *ppm* of NaCl. The electrical resistivity of sea water at 50 deg. *F* is approximately $0.3\Omega \cdot m$ ($3.3S/m$).

In building a consistent earth model for the SE and/or ES effects, we are not at liberty to assign parameters at will. For example, assigning a porosity to a layer affects both the electrical conductivity, equations (5.2.3.3 and 5.2.3.4) and the mass densities and poroacoustic moduli, equations (5.2.1.3 and 5.2.1.6). If we have a good model for the relationship between porosity and permeability (*e.g.*, equation (2.4)), then the permeability is determined as well.

From equation (5.2.3.3), as the cementation factor *m* increases, the apparent resistivity increases and one expects that the dry frame modulus *K* in $\alpha = 1 - K/\overline{K}^s$, equation (5.2.1.6) to increase such that the better the cementation, the parameter α decreases. Figure 5.2.3.2 shows a plot of the *P* modulus, equation (5.2.1.6), as a function of α at two different porosity values, 0.3 and 0.05. For a well cemented formation, we expect a small value of the α parameter and for a not-well cemented formation we expect a larger value of α. To our knowledge, a one-to-one correspondence of the cementation factor *m* to the α parameter has not been firmly established. In the numerical simulations discussed below, we assume $m = 1.4$ and $\alpha = 0.5$.

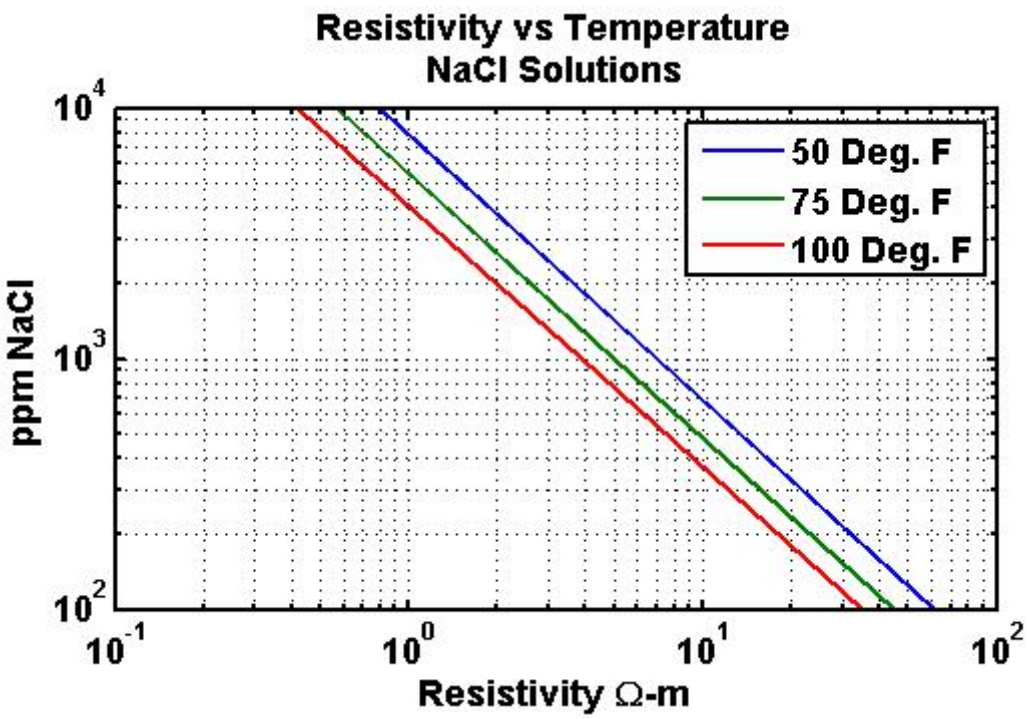

Figure 5.2.3.2: Water resistivity as a function of NaCl concentration at various temperatures.

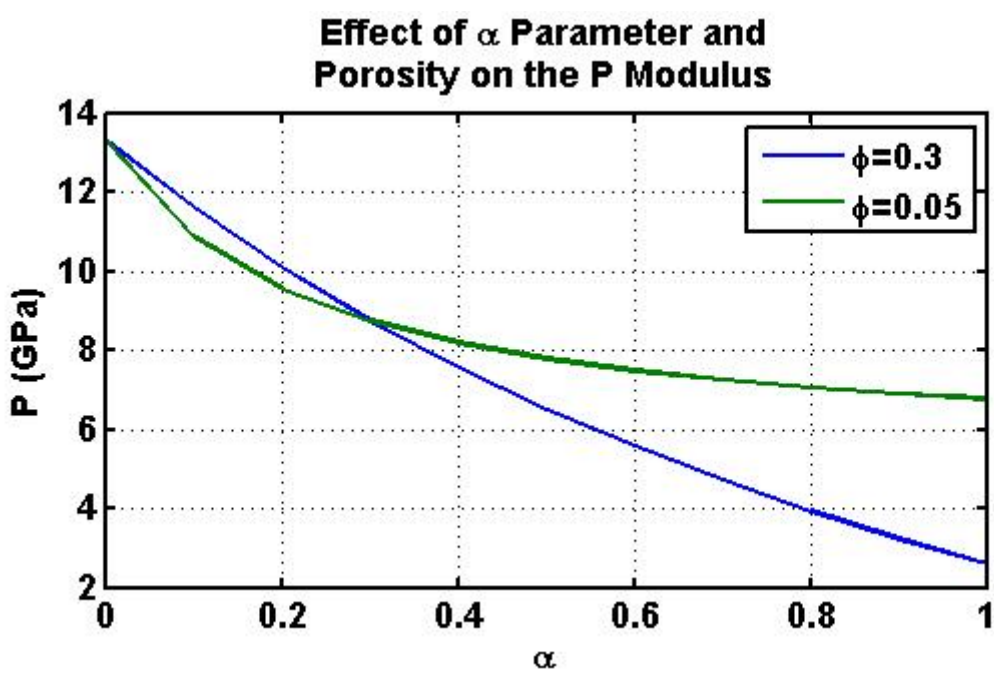

Figure 5.2.3.3: *P* modulus as a function of $\alpha = K/\overline{K}^s$ at two different porosities. In equation (5.18) we used $\overline{K}^s = 12.5 GPa$ and $\overline{K}^f = 2.25 GPa$.

5.2.4 2D Numerical Simulations

The earth model for illustrative numerical simulations is shown in Figure 5.2.4.1. The earth model considers the end members for NaCl concentrations of 100 *ppm* and 2000 *ppm*, with pore water conductivities of 0.017 *S*/*m* and 0.29 *S*/*m*, respectively. From Lorne, *et.al*. (1999), we estimate ς-potential values of -20 *mv* and -2 *mv*, respectively. Figures 5.2.4.2 5.2.4.3, 5.2.4.4, and 5.2.4.5 show trace images of 2D numerical simulations for the SE and ES effects. In these figures, the seismic response is measured using a vertical axis geophone at the surface and the electric field response is measured also at the surface. The SE and ES effects have opposite polarity when measured on opposite sides of the seismic and electric source, respectively, on the other hand, the seismic or electric responses generated by the seismic or electric source, respectively have the same polarity. Since the SE and ES effects have opposite polarity when measured on opposite sides of the source, then for a layered environment we can subtract the response on say the right side of the source from the responses on the left side of the source. The desired signal will add while noise will generally cancel. It is noteworthy that since the air-earth interface part of the 2D algorithm was not fully operational, that for the numerical simulations discussed below, a uniform, non-electrokinetic layer having the properties of water was used to simulate an air-earth interface.

The nearly plane *x*-component of the electric field, E_x, wave at approximately 85 *ms* in Figures 5.2.4.2 and 5.2.4.4 are traveling at EM wave speeds in the medium. This wave is generated when the seismic wave contacts the porous layer at a depth of 200 *m* (Figure 5.2.4.1) and then travels to the surface as shown by the time slices in Figure 5.2.4.6. The other electric field waves are traveling along with the seismic disturbance and are a consequence of electrokinetic behavior of Layer 1 in Figure 5.2.4.1. Comparing Figures 5.2.4.2 and 5.3.4.4 for the *x*-directed electric field generated by a seismic vertical force source, it is apparent that the nearly plane electric field wave at approximately 85 *ms* is weaker with respect to the electric field traveling with the seismic wave for the -20 *mv* value of the ς-potential. The seismic trace images generated by an electric field source are shown in Figures 5.2.4.3 and 5.2.4.5 for the two values of the ς-potential. Figure 5.2.4.7 shows time slices when the electric field "lights up" the porous layer at a depth of 200 *m* and when the nearly plane-wave seismic response traveling at seismic wave speed contacts the earth's surface. The plane-wave first arrival in Figures 5.2.4.3 and 5.2.4.5 were generated at the top and bottom of the porous layer. Note that the response from the bottom of the layer is larger than from the top of the layer. The amplitudes of the nearly plane seismic wave at approximately 85 *ms* are approximately the same as the seismic wave that appears at the same time as that generated by a seismic source, Figure 5.2.4.6. In Figure 5.2.4.6 there appears to be some evidence of grid boundary reflections.

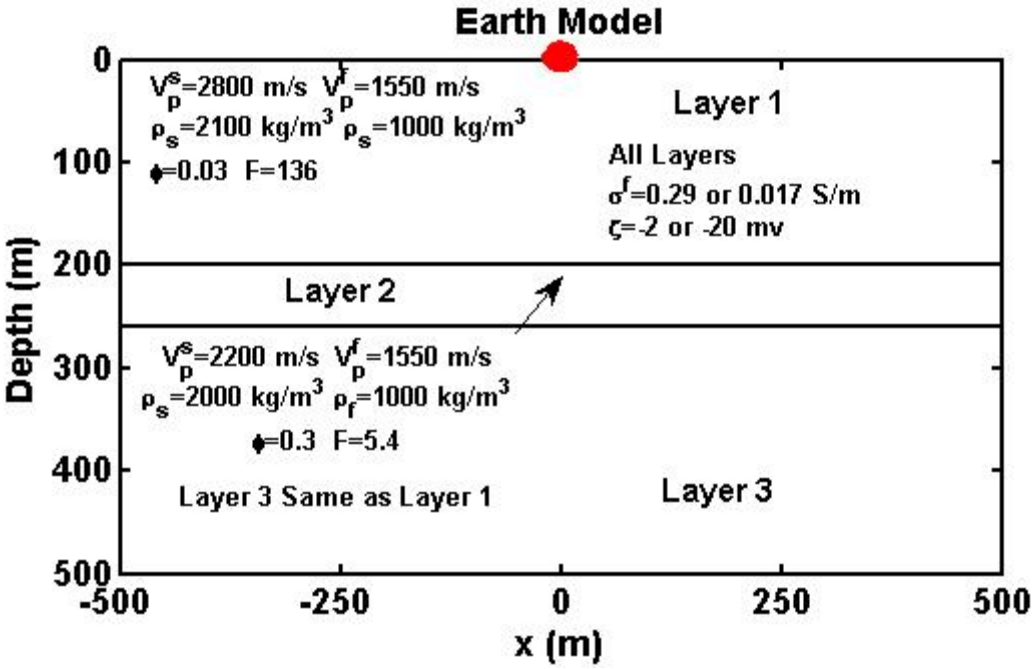

Figure 5.2.4.1: Earth model for SE and ES numerical simulations. The red dot denotes the position of either the vertical force source or the electric field source. Note that all layers have the same pore water conductivity and ς -potential.

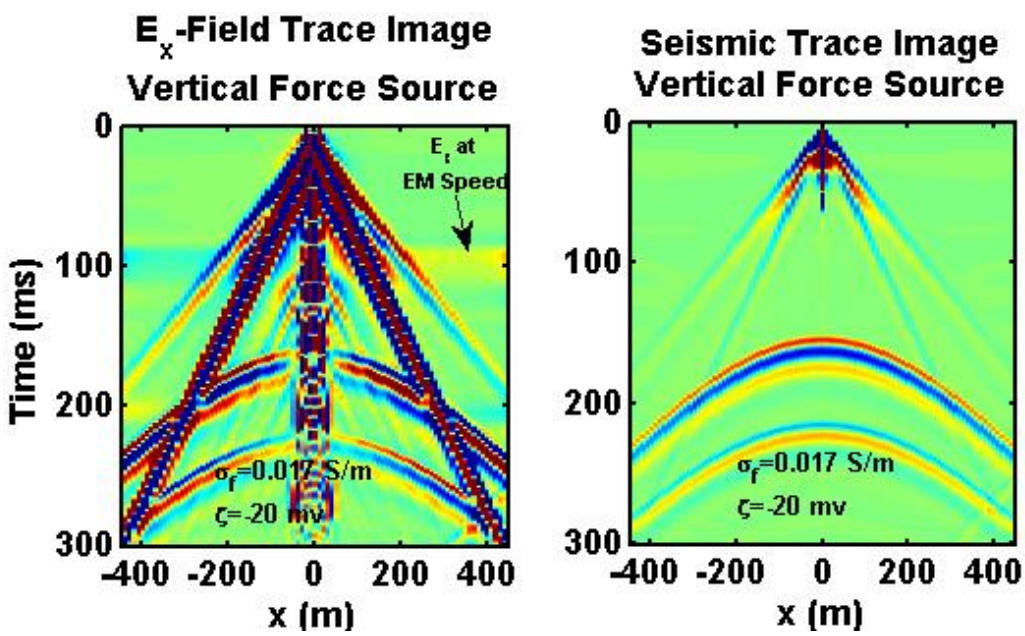

Figure 5.2.4.2: Electric field trace image generated by a seismic vertical force source, left-hand panel. Right-hand panel shows the seismic trace image generated by the vertical force source. The pore water conductivity is 0.017 S/m and $\varsigma = -20\,mv$.

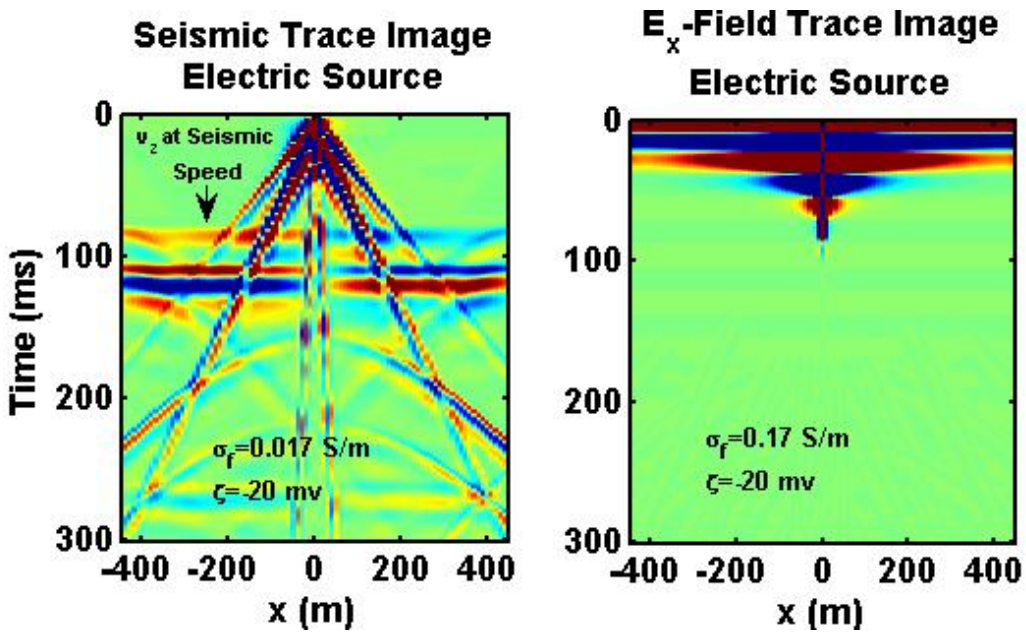

Figure 5.2.4.3: Seismic trace image generated by and electric field source, left-hand panel. The *x*-directed electric field trace image for the electric source is shown in the right-hand panel. The pore water conductivity is 0.017 S/m and $\varsigma = -20\,mv$.

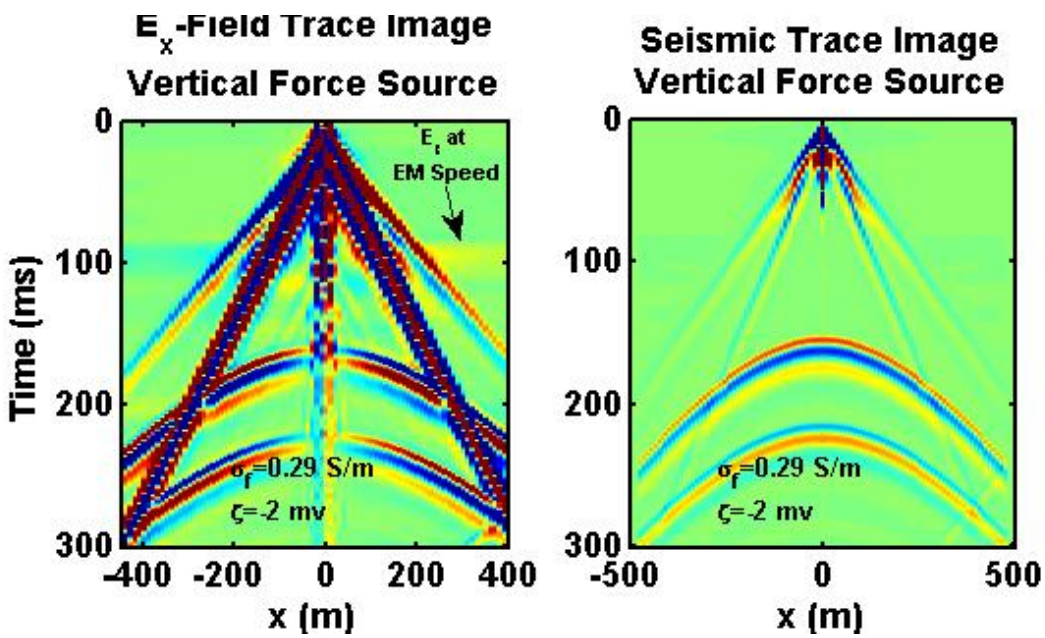

Figure 5.2.4.4: Electric field trace image generated by a seismic vertical force source, left-hand panel. Right-hand panel shows the seismic trace image generated by the vertical force source. The pore water conductivity is 0.29 S/m and $\varsigma = -2\,mv$.

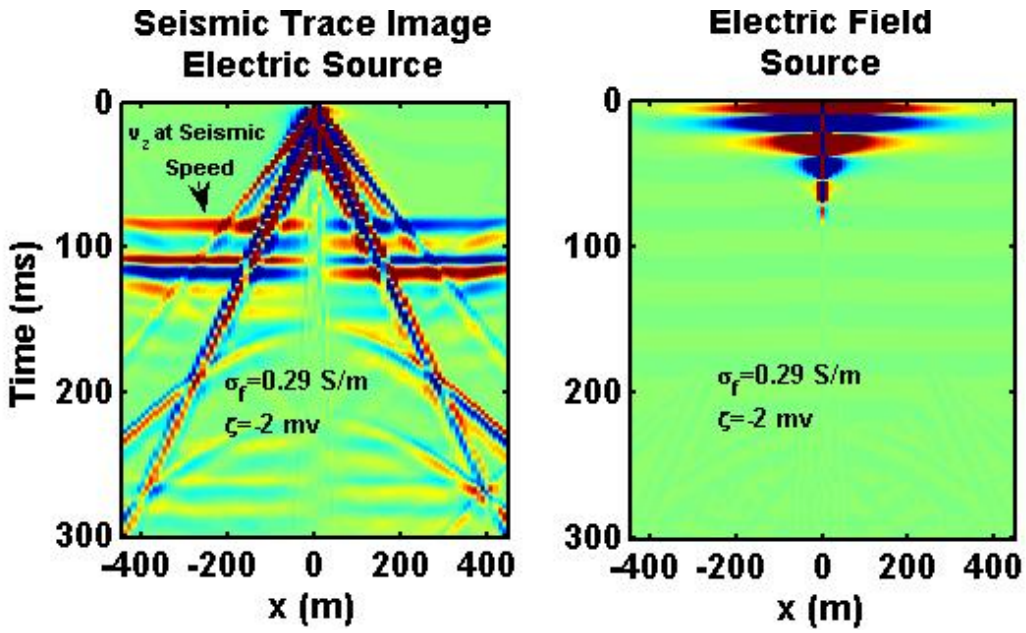

Figure 5.2.4.5: Seismic trace image generated by and electric field source, left-hand panel. The x-directed electric field trace image for the electric source is shown in the right-hand panel. The pore water conductivity is 0.29 S/m and $\varsigma = -2\,mv$.

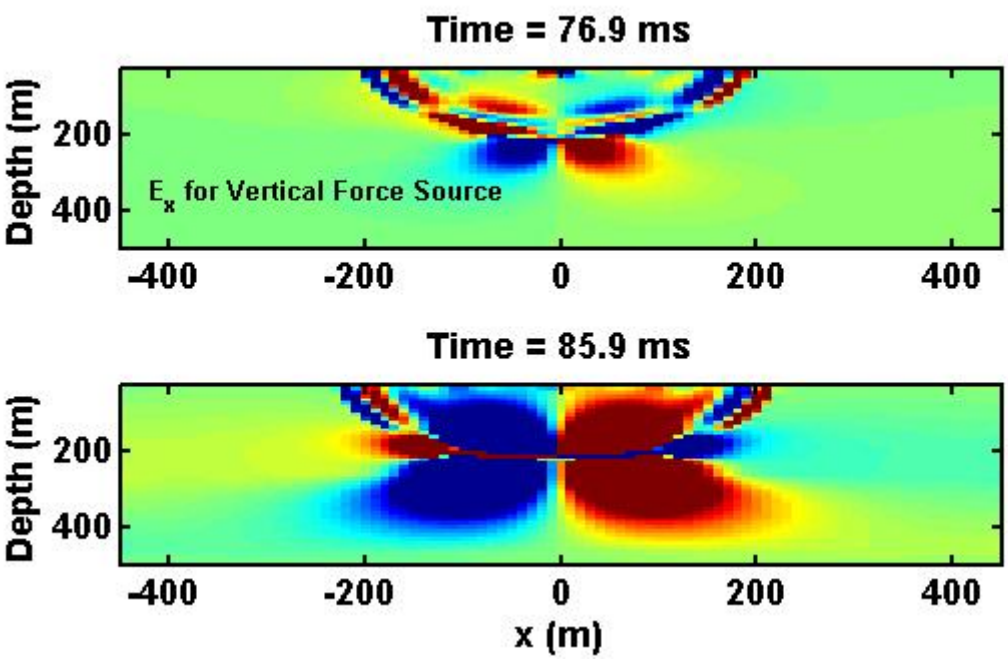

Figure 5.2.4.6: Time slices showing when the seismic wave contacts the porous layer at 200 m (upper panel) and when E_x contacts the earth's surface (lower panel). Here $\sigma_f = 0.017\,S/m$ and $\varsigma = -20\,mv$.

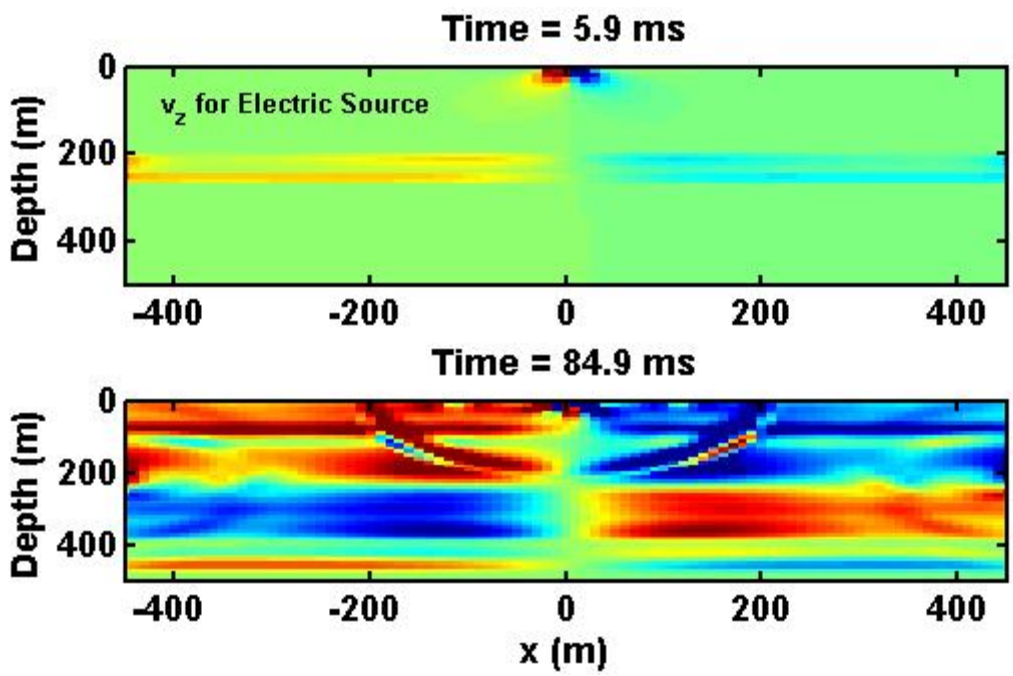

Figure 5.2.4.7: Time slices showing when the electric field contacts the porous layer (upper panel) and when the seismic wave traveling at seismic wave speed contacts the earth's surface. Here $\sigma_f = 0.017\,S/m$ and $\varsigma = -20\,mv$.

To illustrate the effect of the consequences of the pore water conductivity and the ς-potential, traces for a vertical force source and an electric field source are shown in Figure 5.2.4.8. The blue traces are for $\sigma_f = 0.017\,S/m$, $\varsigma = -20\,mv$ and the green traces are for $\sigma_f = 0.29\,S/m$, $\varsigma = -2\,mv$ multiplied by $10 \times 0.29/0.017$. We give the ratio of pore water conductivities since the models have the same formation factor. We could have used the ratio of apparent conductivities. Note for clarity of the trace, we plot dv_z/dt rather than v_z. One expects from the ratio of the ς-potentials a factor of 10 between the traces; however the strength of the electric field that is generated depends upon the pore water conductivity whether it is a seismic or electric source.. Figure 5.2.4.9 shows traces for $\sigma_f = 0.1\,S/m$, $\varsigma = -6\,mv$, blue trace, and $\sigma_f = 0.29\,S/m$, $\varsigma = -2\,mv$, green trace, multiplied by $3 \times 0.29/0.1$ for a vertical force source and an electric field source. Figures 5.2.4.8 and 5.2.4.9 illustrate that the amplitude ratios for various ς-potentials is not just the ratio of the ς-potentials but must include the ratios of the pore water conductivities.

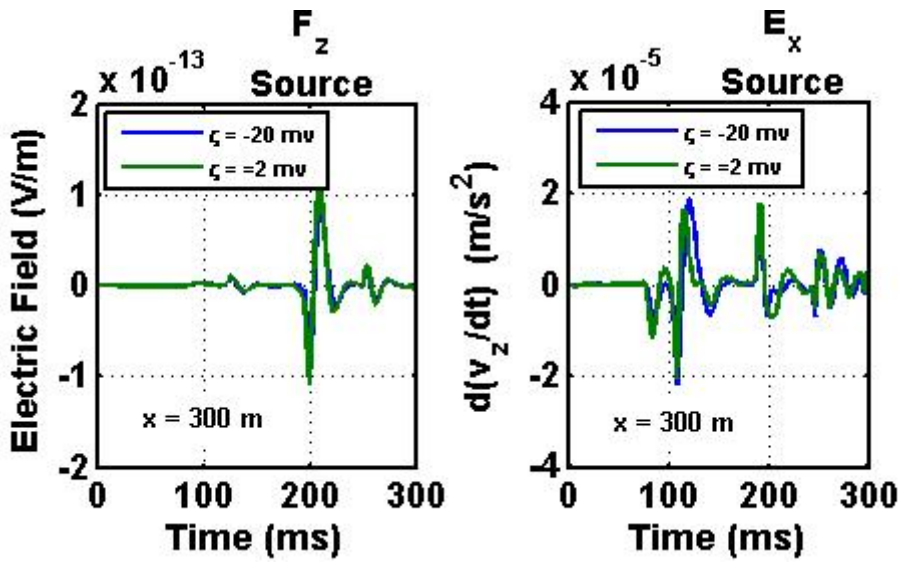

Figure 5.2.4.8: Comparison of electric field and seismic traces for two different ξ-potentials. Blue traces are for $\varsigma = -20\,mv, \sigma_f = 0.017\,S/m$ and the green traces are for $\varsigma = -2\,mv, \sigma_f = 0.29\,S/m$ multiplied by $10 \times 0.29/0.017$. Note for clarity of the traces, we plot dv_z/dt rather than v_z.

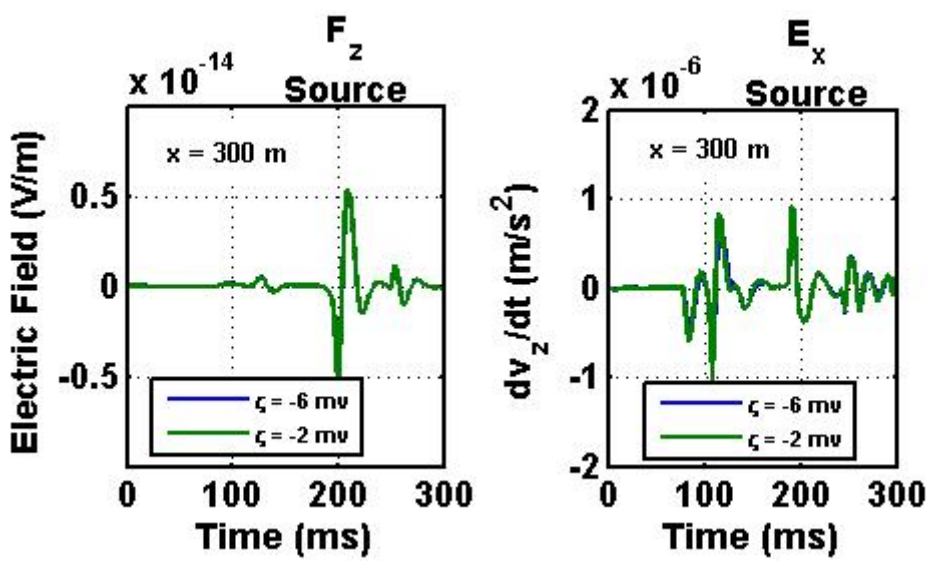

Figure 5.2.4.9: Comparison of electric field and seismic traces for two different ξ-potentials. Blue traces are for $\varsigma = -6\,mv, \sigma_f = 0.1\,S/m$ and the green traces are for $\varsigma = -2\,mv, \sigma_f = 0.29\,S/m$ multiplied by $3 \times 0.29/0.1$. Note for clarity of the traces, we plot dv_z/dt rather than v_z.

6.0 Field Experiment

6.1 Site Description: Geology, Aquifer, and Surface Conditions

The site for the field experiment to observe SE effects was located on the floodplain of the Tijeras Arroyo in Tijeras canyon on Kirtland Air Force Base in Albuquerque, New Mexico. This site was chosen because it is relatively free of structures (e.g. buildings) and distant from noise sources (e.g. vehicle traffic and power lines) that may affect seismic and electromagnetic data. Additionally, the depth to groundwater is relatively shallow and within the range expected to generate an electromagnetic field from the seismic waves induced for this project. Figure 6.1.1 is an aerial photograph of the approximate location of the survey lines in Tijeras canyon. Details of the survey acquisition are given in the section (6.2) of this report.

Geology and aquifer information of this site are described in the SAND reports by Witt *et. al*, (2005) and Sanchez *et al*, (2008). The Tijeras canyon site is composed of coarse-grained alluvial fan sediments from the Manzanita Mountains. These sediments are underlain by relatively impermeable alluvial fan lenses composed of fine-grained clay- and silt-rich sediments, which function as the perching layer for the Perched Ground Water System of the Tijeras Arroyo Groundwater (TAG). Depth to the perched water table is approximately 67 to 100 *m* below ground surface and is within the range expected to generate an electromagnetic field from the seismic waves induced for this project. Thickness of the perched aquifer is 3 to 10 *m*. The conceptual model of TAG from Witt et. al, (2005) is shown in Figure 6.1.2. The effective porosity of the site was reported to be 25%. Pore water salinity varies laterally with values decreasing to the south and was measured between 0.0434 and 0.1729 *S*/*m* in 2006 and 2007. Specific conductivity values measured at wells in the TAG from Sanchez *et. al*, (2008) and a map of well locations are shown in Figure 6.1.3. Figure 6.1.3 is map of the water table elevations (Sanchez *et al*, 2008).

Due to the proximity of study site to the active channel of the Tijeras Arroyo (Figure 6.1.1), the data acquired for this project were influenced by these local fluvial effects in addition to the more regional geology described above. The surface of the study site was composed of loose, fine-grained dry sand, which was slightly moist just below the surface. Vegetation at the site was minimal and composed of short, dry or dead dessert scrub.

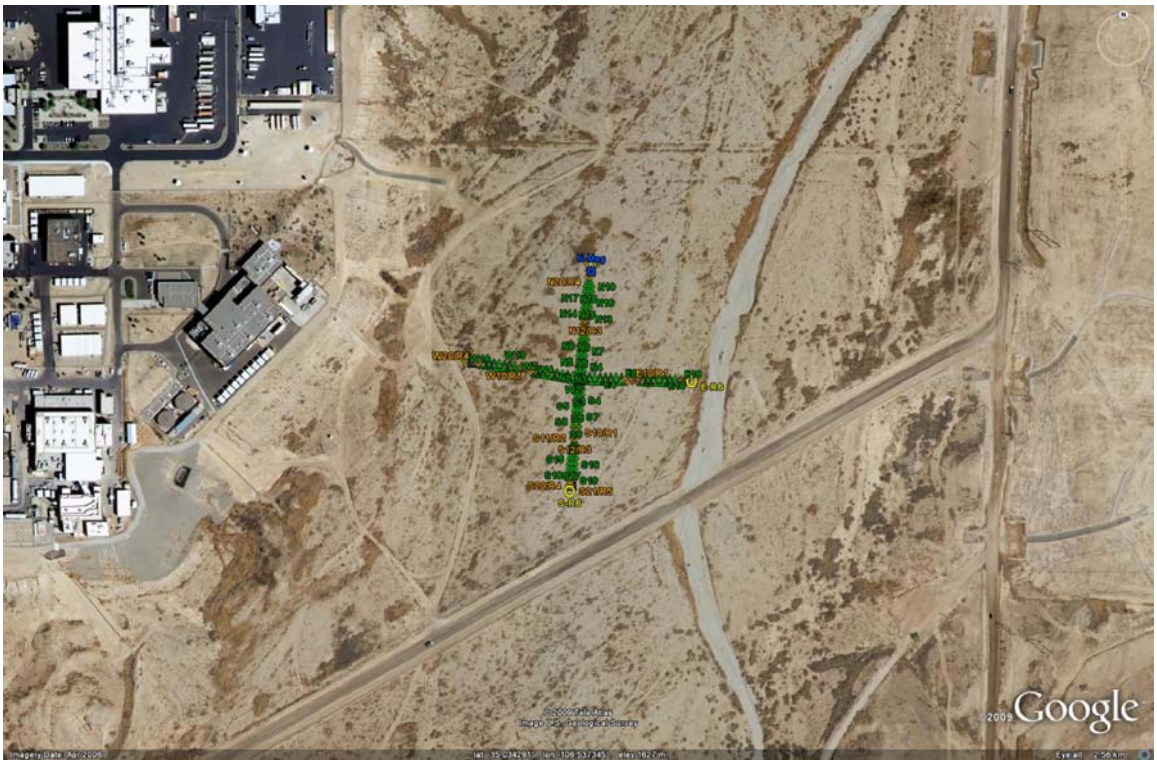

Figure 6.1.1: Aerial photograph of the survey lines. The East segment was not collected due equipment failure.

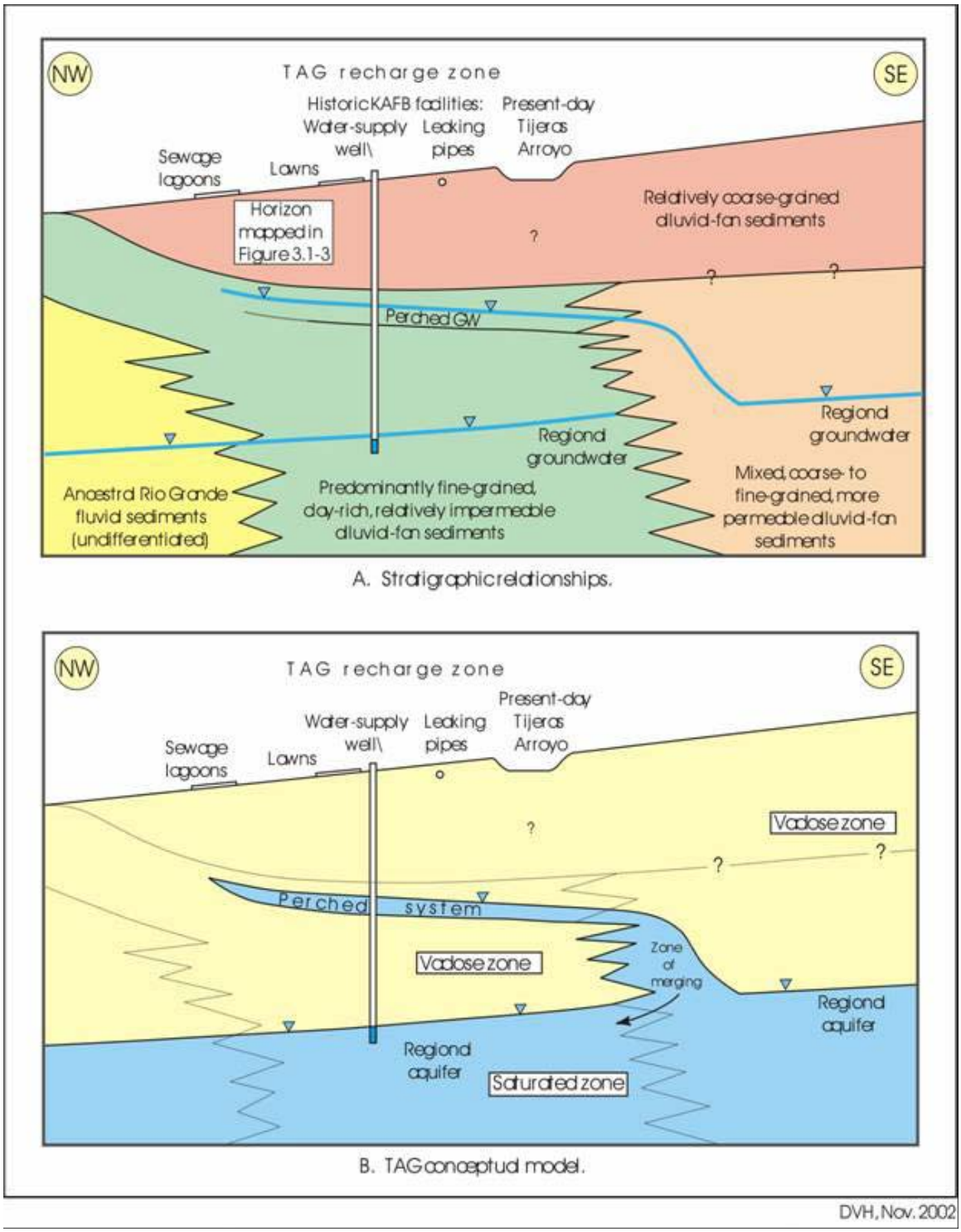

Figure 6.1.2: The conceptual model of Tieras Arroy Groundwater perched aquifer (Witt et. al, 2005).

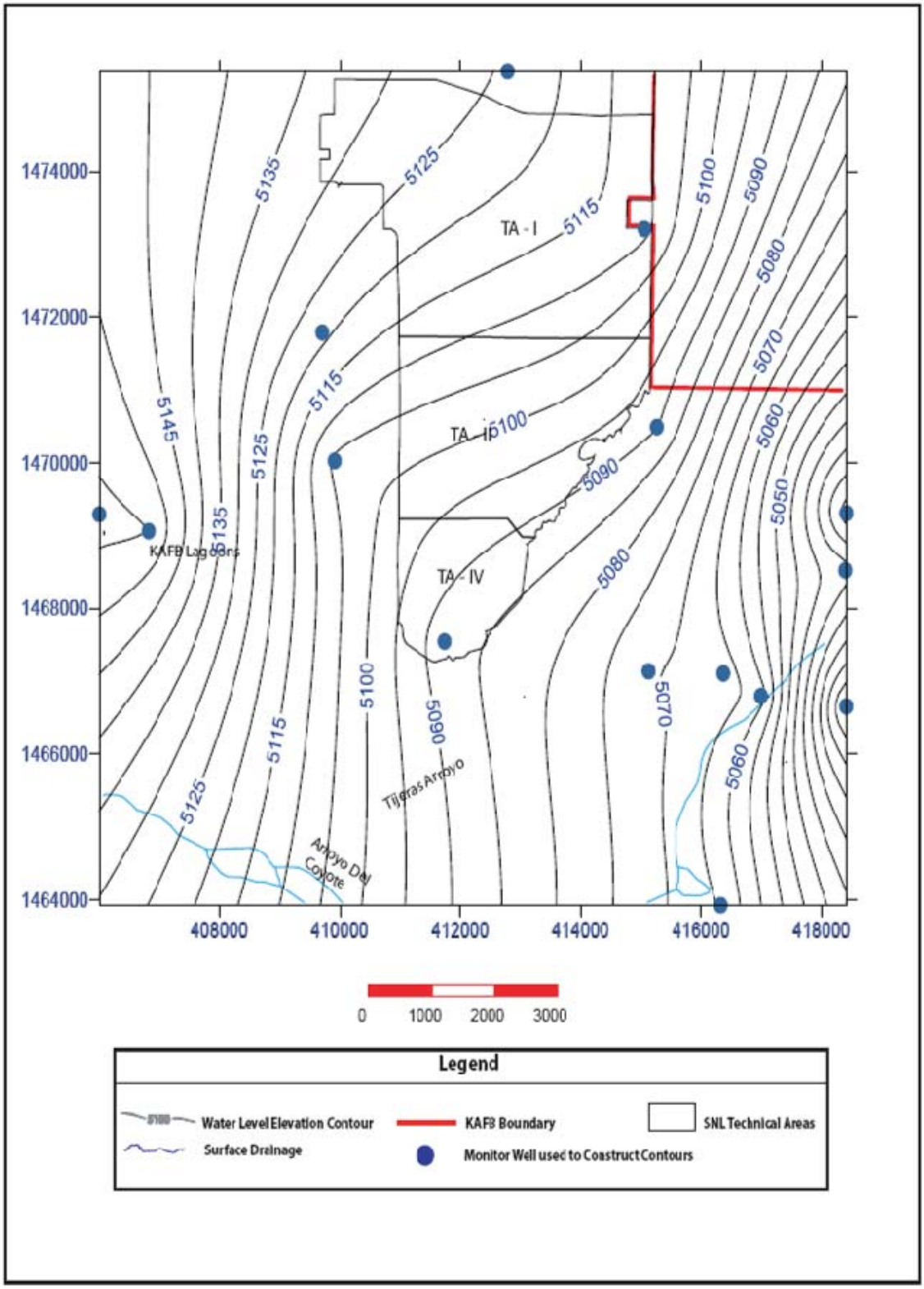

Figure 6.1.3: Map of water table elevations for the Tijeras Arroyo Groundwater perched aquifer (Sanchez *et. al*, 2008).

6.2 Field Acquisition

Field data acquisition began on March 31, 2009 and ended on April 2, 2009. Nedra Bonal, Bruce Engler, Randy Everett, Sean Hollister, and Bill Holub acquired the data on all three days. Scanned copies of field notes are included in Appendix D.

Weather conditions at the site were sunny, cool (< 60°C), and very windy. Strong winds in Tijeras canyon covered everything, including equipment and personnel, with a thin layer of sand but did not seem to adversely effect the quality of the data being collected. Detailed weather conditions from station C0082 near the site but outside the canyon are given in Appendix E.

Seismic and electromagnetic data were collected for analysis of water salinity. Two, orthogonal arrays of geophones and electrodes were proposed as in Figure 6.1.1 with an accelerated weight drop (AWD) source at the intersection of the two lines. Due to equipment constraints, only half of each line could be collected at once totaling four line segments: the North segment, the South segment, the West segment, and the East segment. However, the AWD failed on the last line segment, so the East segment was not collected.

Geophones and electrodes were both connected to a Geometrics Geode recording instrument, which acquired the data in SEG2 format. Data were recorded with a -0.1*s* delay to retain data just prior to the time the source waves were generated. Record lengths were 1.1*s* at 0.125*ms* sampling rate for each file. The recording instrument had 24 channels that were used during acquisition of each line segment: 21 channel had geophone sensors and 3 had electromagnetic sensors. A diagram of the survey arrangement for each line segment is shown in Figure 6.2.1 with details of each channel given in Table 6.2.1. Geophones were vertical, 4.5 *Hz* resonant frequency by Mark Products and were spaced 5m apart for a total line length of 100*m*. Electromagnetic sensors were co-located with geophones at 50 *m* and 100 *m* from the intersection of each line. The electromagnetic sensors consisted of two E-field (electric) and one H-field (magnetic) sensors. The E-field sensors (Figure 6.2.2) were composed of 3 metal stakes (dipole antenna - one positive, one negative, and a ground stake in between), which were driven into the ground inline with the line segment at 5 *m* spacing. The E-field sensors also included Zonge preamps and RC filters (Figure 6.2.3). The H-field sensor was a Zonge EM antenna (Figure 6.2.4) oriented for H-field measurements.

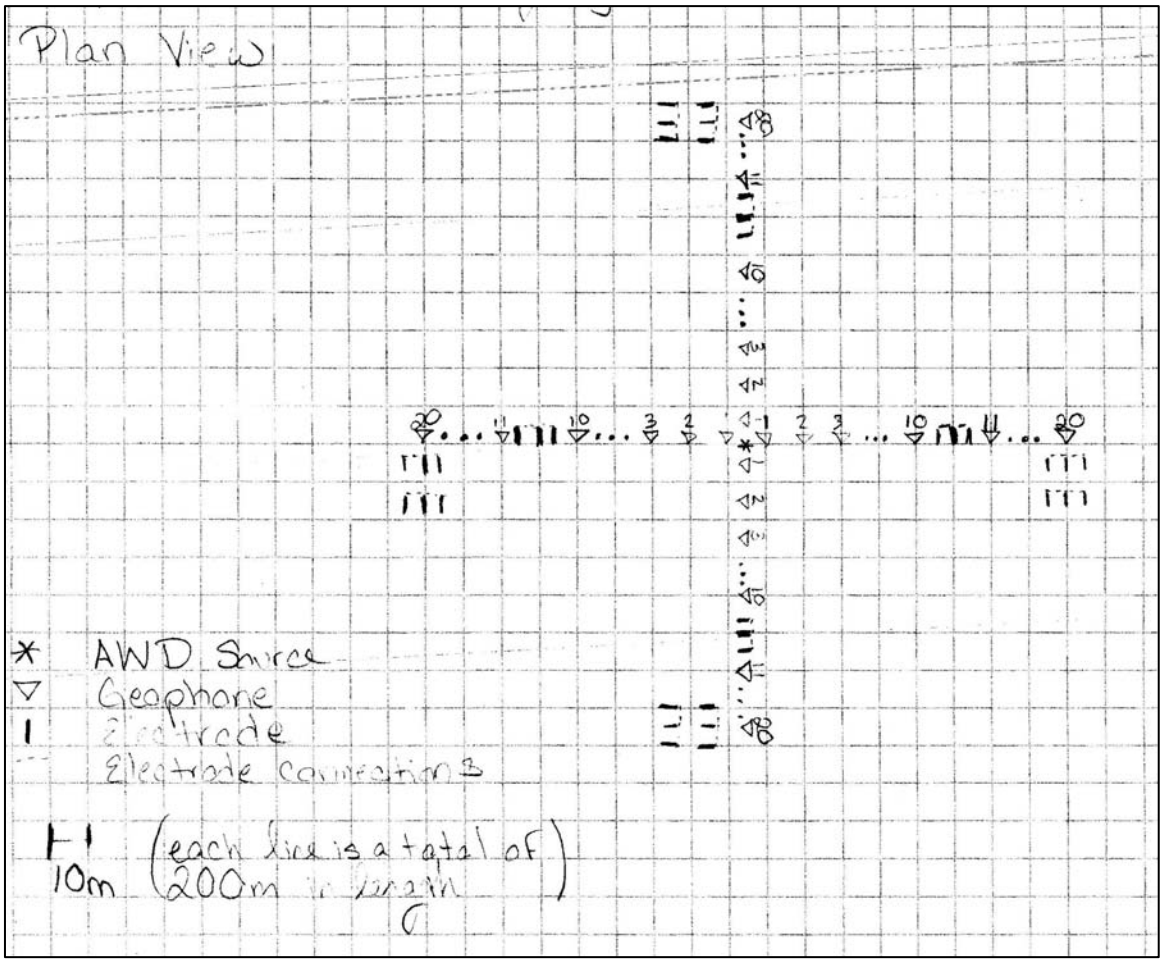

Figure 6.2.1: A diagram of the survey arrangement for each line segment. The East segment was not collected due to failure of the AWD source. The AWD was located at 0m for each segment, at the intersection of the lines. The AWD was also moved outward along each line segment for seismic tomography analysis.

Table 6.2.1: Channel descriptions and locations of each sensor for each line segment acquired.

Channel	Sensor	Rcv Loc (m)
1	Geophone	0
2	Geophone	5
3	Geophone	10
4	Geophone	15
5	Geophone	20
6	Geophone	25
7	Geophone	30
8	Geophone	35
9	Geophone	40
10	Geophone	45
11	Geophone	50
12	E-field (center stake)	50
13	Geophone	55

14	Geophone	60
15	Geophone	65
16	Geophone	70
17	Geophone	75
18	Geophone	80
19	Geophone	85
20	Geophone	90
21	Geophone	95
22	Geophone	100
23	E-field (center stake)	100
24	H-field	100

Rcv Loc is the receiver location – directed outward from the intersection of the lines).

Figure 6.2.2: Array setup for each line segment. E-field stake for dipole antenna is visible in the foreground.

Figure 6.2.3: Zonge preamp (white box) and RC filter (on top of preamp) used for the E-filed sensor.

Figure 6.2.4: Zonge EM antenna used for H-field measurements. Sandbags were packed around the sensor to reduce noise.

Several shots from the AWD source were collected at the 0*m* location (intersection of lines) for each line segment. These data were used for analysis of the seismoelectric effect for water salinity and also for seismic tomography analysis. Additionally, the

AWD was moved along each line segment at 10 *m* increments starting at 7.5 *m* from the intersection of the lines up to 117.5 *m* to collect data for seismic tomography analysis. Files for the seismic tomography included a stack of 10 shots to increase the signal-to-noise ratio of the data.

6.3 Seismic and EM Data for Seismo-Electric Study

Several seismic shot gathers were done to determine the electric field associated with the seismic source, SE effect. For the south line, Figure 6.2.1, these gathers are 106.dat, 107.dat, 108.dat, and 109.dat (Appendix D) where these records represent a stack of 10 vertical force sources. For the north line (Appendix D), the appropriate shot gathers are 207.dat, 208.dat, 209.dat, 210.dat, and 211.dat again each shot gather represents a stack of 10 shots. The seismic trace shown in Figure 6.3.1 represents the combined shot gathers 106.dat to 109.dat and 207.dat to 210.dat. Note these shot gathers were shot on consecutive days (see Appendix D). Note that the long offsets for the south line have a larger amplitude than the long offsets for the north line.

The measured electric field components along the geophone line are shown in Figure 6.3.2 for offsets on the south line of 50 and 100 *m* and the magnetic field component along the geophone line for an offset of 100 *m*. Note, that the fields are in arbitrary units, since neither the electric or magnetic fields have been calibrated. It is evident that there is a large power line noise, 60 *Hz* plus harmonics. In addition, the electric field shows a low frequency noise of approximately 4.5 *Hz*., whose origin is unknown.

Since these noise patterns are predictable, we used a prediction error filter to remove this periodic noise. A prediction filter predicts the signal at a specified lag. A lag of one means predicting the signal at the next time step. MATLAB® has an algorithm for linear predictive coding "lpc". The calling sequence is

$$a = lpc(data, n) \tag{6.3.1}$$

where *a* are the filter coefficients and *n* is the length of the data sequence to determine the coefficients *a*. The predicted data, using MATLAB® "*filter*" routine, oddly enough is

$$predSignal = filter([0 - a(2:end)], 1, data) \tag{6.3.2}$$

and the predicted error signal is

$$predErrorSignal = data - predSignal \tag{6.3.3}$$

or

$$. predErrorSignal = filter(a, 1, data). \tag{6.3.4}$$

The prediction error filter yields that part of the signal that is not predictable. Predictable signals are multiples or any repetitive signal, such as 60 *Hz* and harmonics power line noise. Thus for the electric field, the unpredictable part of the signal is the sought after electric fields generated by the SE effect. It should be mentioned that the prediction filter applied to a signal cannot predict random noise and this random noise is included in the error signal.

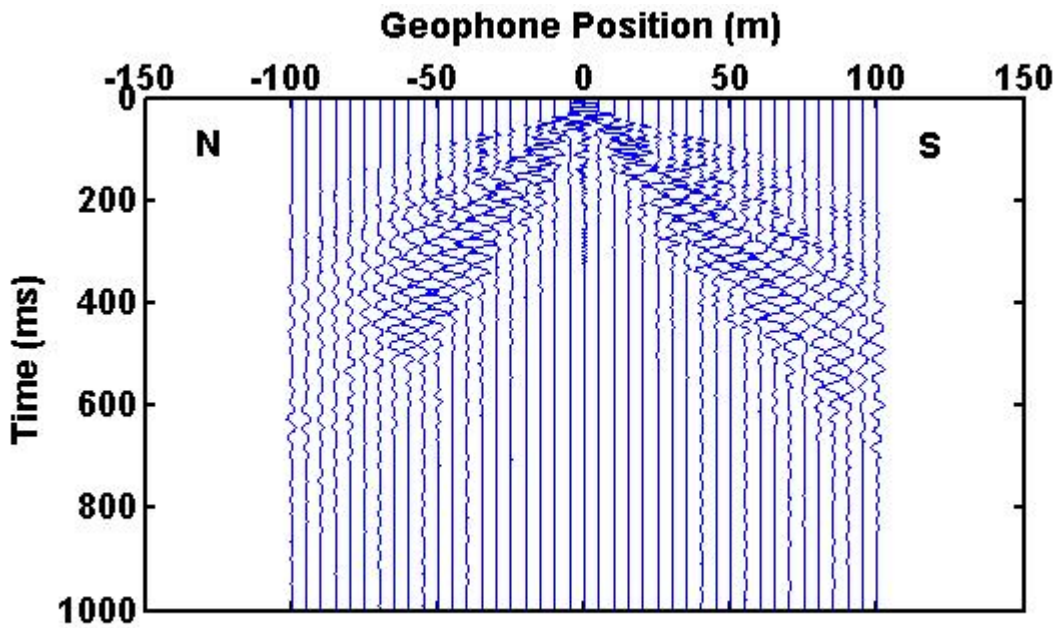

Figure 6.3.1: Trace plot for composite shots 106.dat to 109.dat (south line) and composite 207.dat to 210.dat (north line). Source is the accelerated weight drop producing a vertical force source F_z. Same plot scale was used for both halves of the line.

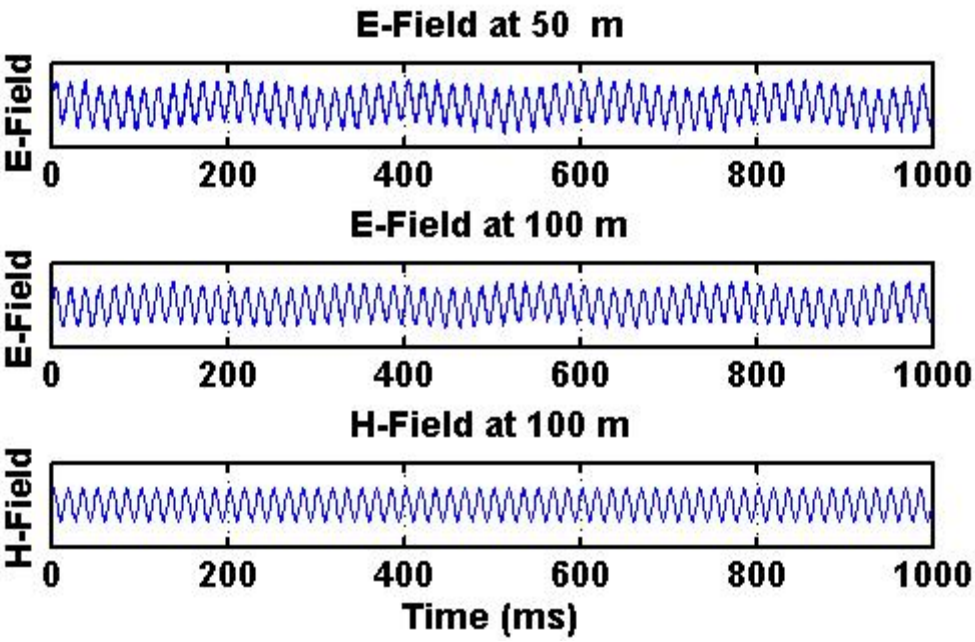

Figure 6.3.2: Electric and magnetic fields for shot gather 108.dat (see Appendix D).

We now compare results of applying the prediction error filter to seismic and electric field data. Figure 6.3.3 shows the prediction error filter applied to the seismic data at 50 *m* (south end of line) for the sum of shot gathers 106.dat, 107.dat, 108.dat, and 109.dat and Figure 6.3.4 shows the prediction error filter applied to the electric field data at 50 *m* (south end of line) for sum of shot gathers 106.dat, 107.dat, 108.dat, and 109.dat. The top panels are the "raw" prediction error filter results and the bottom panels are the results after filtering with a 15 term triangle window to reduce some of the extraneous spikes. The seismic data, Figure 6.3.4, clearly shows a P-wave arrival at 91 *ms* and what appears to be ground roll at 150 *ms*. The electric field data shown in Figure 6.3.4 is very noisy. To reduce this noise, the electric field data from the northern part of the line sum of gathers 207.dat, 208.dat, 209.dat, and 210.dat was subtracted from the data for the southern part of the line sum of gathers are 106.dat, 107.dat, 108.dat, and 109.dat. The subtraction cancels noise from a broad source, while adding the desired signal (see Section 5.2.4 and Appendix D). The comparison of the electric field data to the seismic data at 50 *m* and 100 *m* are shown in Figures 6.3.5 and 6.3.6. In the comparison at 50 *m*, Figure 6.3.5, there is some agreement for the seismic P-wave at 91 *ms* and some later agreement at 145 *ms* just prior to the seismic ground roll at 150 *ms*. In both figures, there is an early peak in the electric field data at 27 *ms* for the measurement at 50 *m* and 22 *ms* for the measurement at 100 *m*. These early arrivals do not appear to be tied directly to any seismic arrivals, which may indicate an electric field traveling at EM wave speed that is generated by a seismic wave as it impinges upon an electrokinetic active layer. The electric field that is closely tied to the seismic data at 91 *ms* and possibly 145 *ms* could be the electric field riding along with the seismic disturbance (see Figures 5.2.4.2 and 5.2.4.4). From the analysis of the data, there are no definitive responses that are clearly due to the seismo-electric effect. A reason for this is discussed in the next section.

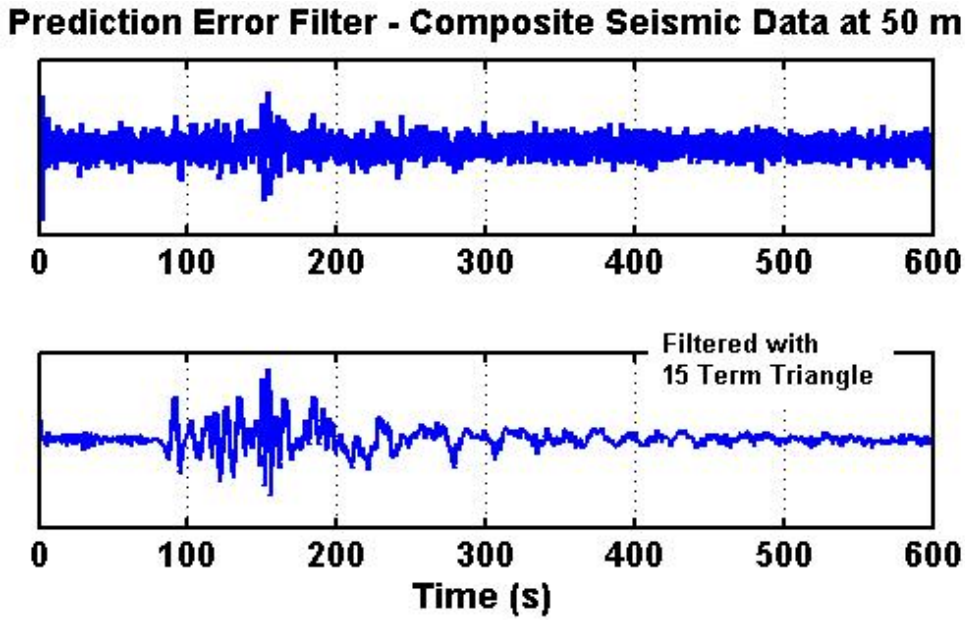

Figure 6.3.3: Prediction error filter applied to seismic data taken at 50 m. Upper panel is the "raw" prediction error filter results and the bottom panel are results filtered using a 15 term triangle window.

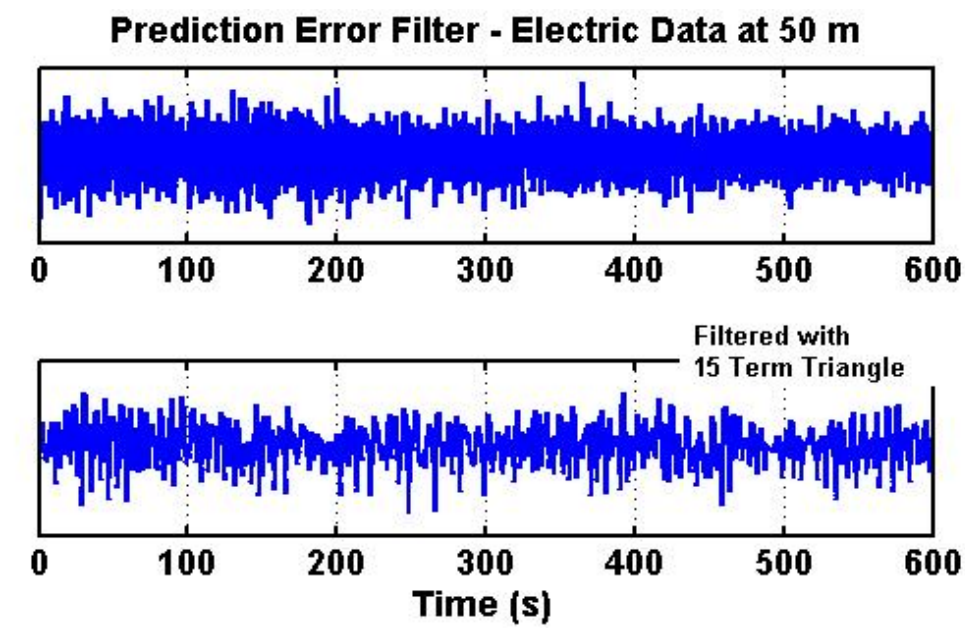

Figure 6.3.4: Prediction error filter applied to the electric field data taken at 50 m. Upper panel are the "raw" results and the bottom panel are the results filtered using a 15 term triangle window.

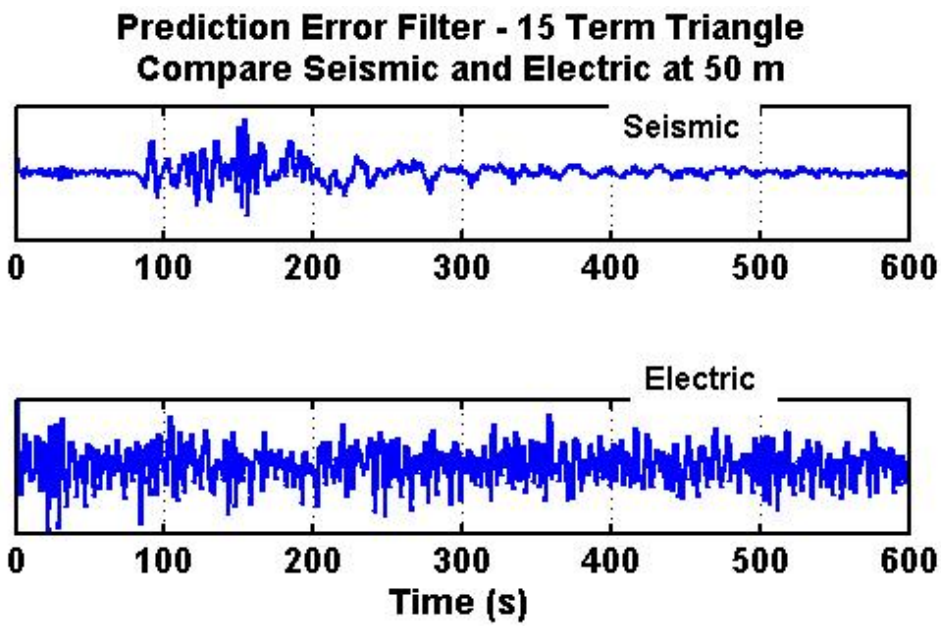

Figure 6.3.5: Comparison of the prediction error filter results (with 15 term triangle window) applied to seismic data at 50 *m* (upper panel) and to the electric field data (data at 50 *m* minus data at -50 *m*) (lower panel).

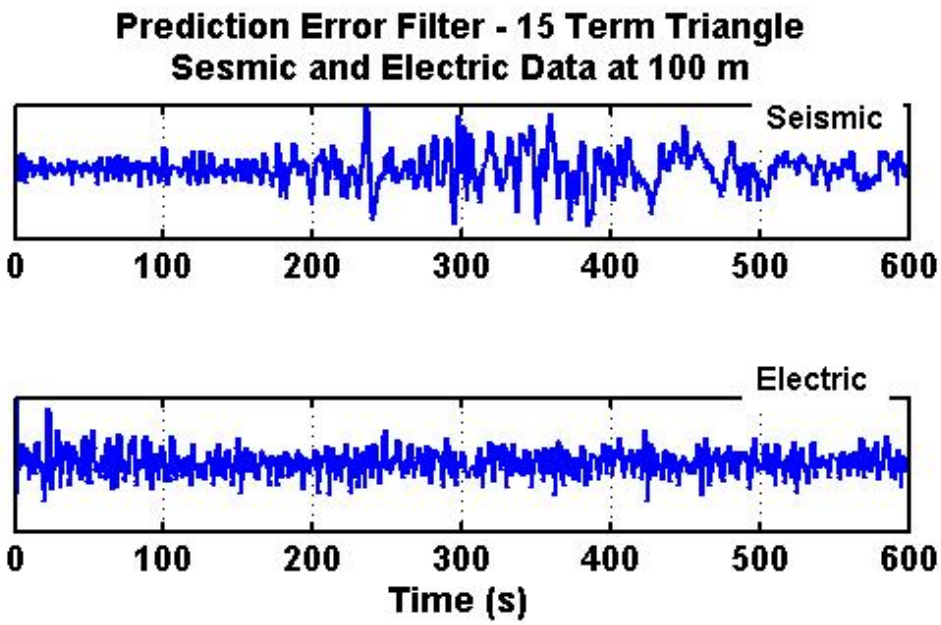

Figure 6.3.6: Comparison of the prediction error filter results (with 15 term triangle window) applied to seismic data at 100 *m* (upper panel) and to the electric field data (data at 100 *m* minus data at -100 *m*) (lower panel).

6.4 Seismic Tomography Results for the Tijeras Canyon Site

The tomographic inversion scheme, PRONTO (Aldridge and Oldenburg, 1993), uses the finite-difference travel-time method of Vidale (1988) and utilizes first break picks (travel-times of the first seismic wave arriving at each geophone) from shot profiles (location-ordered geophone trace data from the same source). First breaks were used in PRONTO to obtain a velocity model for the site and perform a two-dimensional tomographic inversion. The velocity model was calculated using refraction analysis of the first break travel-times and was iteratively compared to synthetic travel-times calculated from the velocity model until the synthetic results reasonably matched the travel-times picked from the data. The synthetic travel-time calculations used simple, homogeneous and isotropic horizontal layers. Output from the tomography analysis includes two-dimensional offset versus depth profiles of P-wave velocity and raypath density estimated from the tomography program. Figures 6.4.1 and 6.4.2 show the results of the seismic tomography analysis from PRONTO for the combined North and South and West line segments, respectively. Velocity images are shown in the left panel and raypath density images are shown in the right panel of the figures.

Tomography results show there is a reflective layer at about 10 *m* below ground surface. Because most of the seismic energy is being reflected from this layer, little energy is able to reach deeper depths to the perched aquifer (at least 67 *m* down). This means that the AWD seismic source used at Tijeras canyon for this experiment likely did not have enough energy to produce a strong EM field response at the perched water table. A field site without a strong reflecting layer above the water table and/or more energy induced by the seismic source should produce a stronger EM field response.

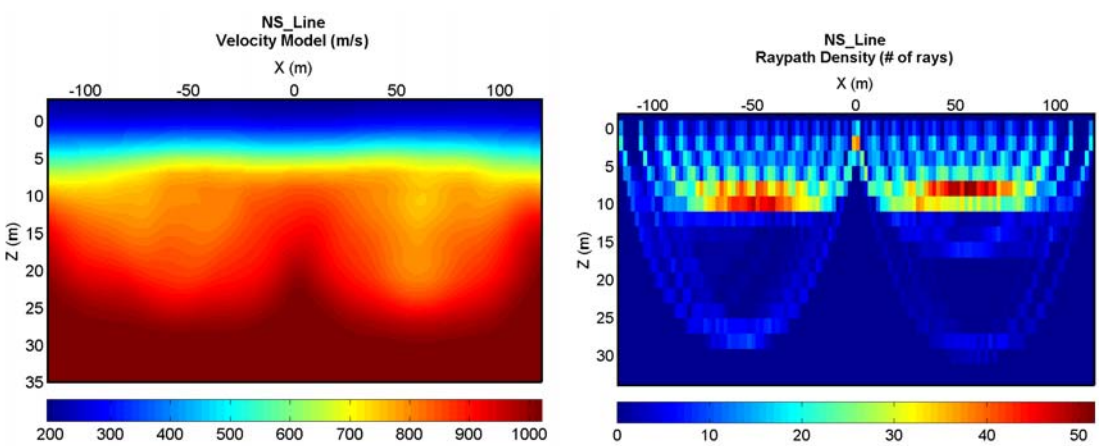

Figure 6.4.1: Results of the seismic tomography analysis from PRONTO for the combined North and South line segments. P-wave velocity is shown in the left panel and raypath density is shown in the right panel.

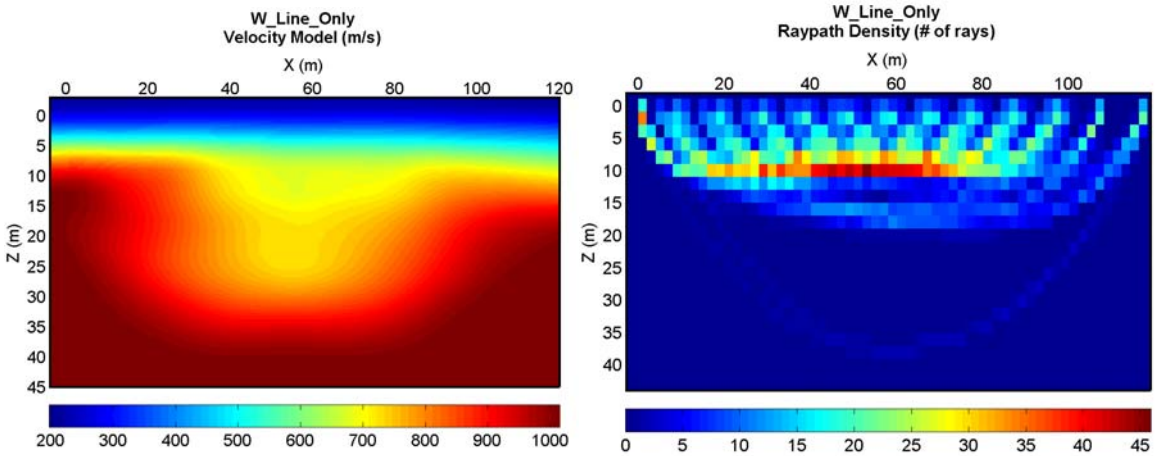

Figure 6.4.2: Results of the seismic tomography analysis from PRONTO for the West line segments. P-wave velocity is shown in the left panel and raypath density is shown in the right panel.

7.0 Conclusions

The research addressed the utilization of seismic and EM methods to characterize an aquifer. In numerical simulations we addressed the traditional use of seismic data to constrain the earth structure to develop an electrical conductivity structure to perform EM numerical simulations. For thin porous layers (20 *m* thick), use of RTM provided a clear image of the porosity variations. On the other hand, for this same model the EM calculations were not able to distinguish a relatively narrow high porosity slab in an otherwise low porosity layer. The EM simulations showed that the layer was detectable if it had a large value of pore water conductivity associated with 2000 *ppm* of NaCl. For a thicker layer (60 *m* thick), the EM numerical simulations could distinguish various values assigned to the pore water conductivity associated with 100, 750, and 2000 *ppm* of NaCl. In this later case, the combination of RTM imaging of the water reservoir and EM numerical modeling could be used to estimate the pore water conductivity.

We reviewed the development of the Gouy-Chapman theory of the electric double layer (EDL). We showed how the ς-potential properties of the EDL govern the magnitude of the SE and ES effects, whether the source is a seismic or an electric source. We developed a 1D analytic solution for the coupling of the pressure and the electric field. For a pressure source, two electric fields are generated one traveling at the EM wave speed for the host medium and one riding along with the pressure disturbance. For an electric source, two pressure responses are generated one traveling at seismic wave speeds and one riding along with the electric field disturbance. The pressure wave riding along with the electric field disturbance has not reported to our knowledge. From our numerical 2D simulations, we showed that the SE and ES effects depend not only upon the ς-potential, but on the electrical conductivity of the host medium as well.

As part of our development of the 2D SE/ES algorithm, we gave a recipe for determining the minimum and maximum value of a fictitious electric permittivity so that the EM finite-difference solutions are stable and the induction limit response is honored. The maximum fictitious value was determined through analytical 1D calculations of the electric and magnetic fields.

In our 2D algorithm we combined two different physical phenomena that are coupled through the electrokinetic effect. In finite-difference modeling of coupled seismic and EM wave propagation, these different physical phenomena have different spatial and temporal scales. For example, the seismic spatial grid spacing may be 1-10 *m* with a time step of 0.1 *ms*, while the EM spatial grid spacing may be 10-20 *m* with a time scale of 1-10 μs. We developed an interpolation scheme so that the seismic wave propagation is calculated on the appropriate seismic spatial and temporal grids and the EM wave propagation is calculated on the appropriate EM spatial and temporal grids. This methodology can be applied to other coupled physical phenomena that naturally have different spatial and temporal scales.

As part of this LDRD research, we conducted a small-scale experiment in Tijeras Arroyo to assess the conversion of seismic energy to electric energy (SE effect). The seismic source used was an accelerated weight drop providing a vertical body force. We analyzed the electric field data using a prediction error filter method to remove sinusoidal power line noise. The prediction error filtered results indicated “hints” of an electric field derived from the seismic source; however, the results were not definitive. The results are certainly a long way from estimating pore water salinity. A seismic P-wave tomogram was constructed from seismic data. The tomogram and raypath coverage indicates a strong shallow reflector ~10 *m* that prevented appreciable seismic energy from reaching the desired aquifer ~67 *m* deep. Even though the data were stacked, the accelerated weight drop did not have sufficient energy for this application.

References

Aldridge, D. F. and Oldenburg, D. W., 1993, Two-Dimensional tomographic inversion with finite-difference traveltimes: Journal of Seismic Exploration, v. **2**, pp. 257-274.

Aldridge, D.F., 2007, Time-domain finite-difference algorithm for simulating three-dimensional poroelastic wave propagation: Technical report SAND2007-1782, Sandia National Laboratories.

Bartel, L. C., 1990, Results from a controlled-source audiofrequency magnetotelluric survey to characterize an aquifer: Geotechnical and Environmental Geophysics, Volume II - Environmental and Groundwater, Society of Exploration Geophysicists.

Bartel, L. C., Aldridge, D. F., Symons, N. P., and Haney, M. M., 2008, Reverse-time seismic and acoustic wave propagation: high-fidelity subsurface imaging: Technical Report SAND2008-0159, Sandia National Laboratories.

Biot, M. A. (1956), Theory of propagation of elastic waves in a fluid-saturated porous solid: low-frequency range: J. Acoust. Soc Am., **28**, 168-178.

Deckman, H., Herbolzheimer, E., and Kushnick, A., 2005, Determination of electrokinetic coupling coefficients: Soc. Exploration Geophysicists Expanded Abstracts, **24**, 561-564.

DesJardin, P. E., Nelson, J. M., Gritzo, L. A., Lopez, A. R., Soo-Attila, J. M., Keyser, D. R., Ghee, T. A., Disimile, P. J., and Tucker, J. R., 2001, Towards subgrid scale modeling of suppressant flow in engine nacelle clutter, Technical Report, SAND2001-1972C, Sandia National Laboratories.

Devasenathipathy, S. and Santiago, J. G., 2003, Electrokinetic flow diagnostics: Micro and Nano-Scale Diagnostic Techniques, ed., Breuer, K. S., Springer Vertag.

Du Fort, E. C. and Frankel, S. P., 1953, Stability conditions in the numerical treatment of parabolic differential equations: Math tables and other aids to comput. (former title of Math Comput.), **7**, 135-152.

Geerits, T. W., 1996, Acoustic wave propagation through porous media revisited: J. Acoust. Soc. Am., **100**, 2949-2959.

Han, D-h. and Batzle, M. L., 2004, Gassmann's equation and fluid-saturation effects on seismic velocities: Geophysics, **60**, 398-405.

Katz, A. J. and Thompson, A. H., 1986, Quantitative prediction of permeability in porous rocks: Phys. Rev. B, **34**, 8179-8181.

Kirby, B. J. and Hasselbrink, Jr., E. F., 2004, Zeta potential of microfluidic substrates: 1. Theory, experiment techniques, and effects of separations: Eletrophoresis, **25**, 187-202.

Lorne, B., Perrier, F., and Avouac, J.-P., 1999, Streaming potential measurements 1. Properties of the electrical double layer from crushed rock samples: J. of Geophys. Res., **104**, 17857-17877.

Malaver, C. H., 2004, Statistical applications to quantitative seismic reservoir characterization and monitoring at West Pearl Queen Field, Lea County, New Mexico: Master of Science (Geophysical Engineering) Thesis, Colorado School of Mines.

Mikhailov, O. V., Queen, J., and Toksoz, M. N., 2000, Using borehole electroseismic measurements to detect and characterize fractured (permeable) zones: Geophysics, **65**, 1098-1112.

Moore, J. R., Glaser, S. D., Morrison, H. F., and Hoversten, G. M., 2004, The streaming potential of liquid carbon dioxide in Berea sandstone: Geophysical Res. Letters, **31**, L17610 (4 pages).

Neev, J. and Yeatts, F. R., 1989, Electrokinetic effects in fluid-saturated poroelastic media: Phys. Rev. B, **40**, 9135-9141.

Oristaglio, M. L. and Hohmann, G. W., 1984, Diffusion of electromagnetic fields into a two-dimensional earth: A finite-difference approach: Geophysics, **49**, 870-894.

Pride, S. 1994. Governing equations for the coupled electromagnetics and acoustics of porous media: Phys. Rev. B, **50**, 15678-15696.Thompson, A. H., and Gist, G. A., 1993, Geophysical applications of electrokinetic conversion: The Leading Edge, **12**, 1169-1173.

Sanchez, R., Koss, S., Gorman, S., and Cunningham, C., 2008, Annual Groundwater Monitoring Report, Sandia National Laboratories, Albuquerque, New Mexico, SANDIA REPORT, SAND2008-0972P.

Thompson, A. H. and Gist, G. A., 1991, Electroseismic prospecting: Soc. Exploration Geophysicists Expanded Abstracts **10**, 425-427.

Thompson, A. H., and Gist, G. A., 1993, Geophysical applications of electrokinetic conversion: The Leading Edge, **12**, 1169-1173.

Thompson, A. H., 2005, Electromagnetic-to-seismic conversion – successful developments suggest viable applications in exploration and production: Soc. of Exploration Geophysicists Expanded Abstracts, **24**, 554-556.Wang, T. and Hohmann, G. W., 1993, A finite-difference, time-domain solution for three-dimensional electromagnetic modeling: Geophysics, **58**, 797-809.

Vidale, J., 1988, Finite-difference calculation of travel times: Bulletin of the Seismological Society of America, v. **78**, no. 6, pp. 2062-2076.

Wang, Z., Cates, M.E., and Langan, R.T., 1998, Seismic monitoring of a CO_2 flood in a carbonate reservoir: a rock physics study: Geophysics, **63**, 1604-1617.

Ward, S. H. and Hohmann, G. W., 1987, Electromagnetic theory for geophysical applications, in Electromagnetic Methods in Applied Geophysics , M. N. Nabighian, ed.: Society of Exploration Geophysicists.

Appendix A

Coupled Pressure and EM Waves – Seismoelectric Wave Propagation

The purpose of this appendix is to examine the seismo-electric effect in one dimension so that an analytic solution can be obtained.

For the fluid, the 1D equations of motion are

$$\begin{aligned} \rho\frac{\partial v}{\partial t} &= -\frac{\partial p}{\partial z} + f \\ \frac{\partial p}{\partial t} &= -K_f\frac{\partial v}{\partial z} - \frac{1}{3}\frac{\partial m}{\partial t} \end{aligned}, \tag{A.1}$$

where f is a body force and m is a moment source. Taking the time derivative of the pressure equation and using the velocity equation, we get

$$\frac{\partial^2 p}{\partial z^2} - \frac{1}{\alpha^2}\frac{\partial^2 p}{\partial t^2} = \frac{\partial f}{\partial z} + \frac{1}{3\alpha^2}\frac{\partial^2 m}{\partial t^2}. \tag{A.2}$$

where α is the compressional wave speed in the fluid medium.

The electrokinetic equations are (e,g,, Moore, *et.al*,, 2004)

$$\begin{aligned} \mathbf{q} &= -L_{11}\nabla p + L_{12}\mathbf{e} \\ \mathbf{j} &= -L_{21}\nabla p + L_{22}\mathbf{e} \\ L_{21} &= L_{12} = -\frac{\varepsilon\varsigma}{\eta F} \\ L_{11} &= \frac{k_h}{\eta} \\ L_{22} &= \sigma \end{aligned}, \tag{A.3}$$

where **q** is the fluid flow due to a pressure gradient and an electric field, **j** is the electric current density due to a pressure gradient and an electric field. In the expressions for the coupling coefficients, ς is the zeta potential (which is a function of salinity and water quality), η is fluid viscosity, F is the formation factor, and k_h is the hydraulic permeability. The formation factor is the ratio of the pore water conductivity to the bulk apparent conductivity. In the static case where there is no fluid flow, the gradient of the pressure body force term is counterbalanced by the charge density times the electric field. Thus

$$f = \nabla p = \frac{L_{12}}{L_{11}}\mathbf{e} = \rho_c \mathbf{e}\,. \tag{A.4}$$

For the EM fields, Maxwell's equations that includes the electokinetic effects gives rise to an electrical current as a source term. Thus

$$\begin{aligned}
&\nabla \times \mathbf{e} = -\frac{\partial \mathbf{b}}{\partial t} \\
&\nabla \times \mathbf{h} = \frac{\partial \mathbf{d}}{\partial t} + \mathbf{j} \\
&\mathbf{j} = \sigma \mathbf{e} - L_{21}\nabla p + \mathbf{j}_{imp} \\
&\nabla \times \mathbf{b} = \varepsilon\mu \frac{\partial \mathbf{e}}{\partial t} + \mu\sigma\mathbf{e} - \mu L_{21}\nabla p + \mu \mathbf{j}^{imp} \\
&\mathbf{b} = \mu \mathbf{h} \\
&\mathbf{d} = \varepsilon \mathbf{e}
\end{aligned} \quad , \tag{A.5}$$

where μ is the magnetic permeability (usually taken to be that of free space), ε is the electric permittivity of the medium, σ is the electrical conductivity of the medium (L_{22} coefficient), and $\mathbf{j}^{imp}$ is the external impressed current density. Solving for a second order differential equation for the electric field we have

$$\begin{aligned}
&\nabla \times \frac{\partial \mathbf{b}}{\partial t} = \varepsilon\mu \frac{\partial^2 \mathbf{e}}{\partial t^2} + \mu\sigma \frac{\partial \mathbf{e}}{\partial t} - \mu L_{21}\nabla \frac{\partial p}{\partial t} + \mu \frac{\partial \mathbf{j}^{imp}}{\partial t} \\
&\nabla \times \mathbf{e} = -\frac{\partial \mathbf{b}}{\partial t} \\
&-\nabla \times \nabla \times \mathbf{e} - \varepsilon\mu \frac{\partial^2 \mathbf{e}}{\partial t^2} - \mu\sigma \frac{\partial \mathbf{e}}{\partial t} = -\mu L_{21}\nabla \frac{\partial p}{\partial t} + \mu \frac{\partial \mathbf{j}^{imp}}{\partial t} \\
&\nabla^2 \mathbf{e} - \nabla(\nabla \cdot \mathbf{e}) - \varepsilon\mu \frac{\partial^2 \mathbf{e}}{\partial t^2} - \mu\sigma \frac{\partial \mathbf{e}}{\partial t} = -\mu L_{21}\nabla \frac{\partial p}{\partial t} + \mu \frac{\partial \mathbf{j}^{imp}}{\partial t}
\end{aligned} \quad , \tag{A.6}$$

In 1D we have for the electric field in the *z*-direction (the direction of the pressure gradient) we have

$$\frac{\partial^2 e_z}{\partial z^2} - \varepsilon\mu \frac{\partial^2 e_z}{\partial t^2} - \mu\sigma \frac{\partial e_z}{\partial t} - = -\mu L_{21}\frac{\partial^2 p}{\partial z \partial t} + \mu \frac{\partial j_z^{imp}}{\partial t}\,. \tag{A.7}$$

The coupled equations are (dropping the *z* subscript)

$$
\begin{aligned}
&\frac{\partial^2 e}{\partial z^2} - \frac{1}{c^2}\frac{\partial^2 e}{\partial t^2} - \mu\sigma\frac{\partial e}{\partial t} = -\mu L_{21}\frac{\partial^2 p}{\partial z \partial t} + \mu\frac{\partial j^{imp}}{\partial t} \\
&\frac{\partial^2 p}{\partial z^2} - \frac{1}{\alpha^2}\frac{\partial^2 p}{\partial t^2} = \frac{\partial f}{\partial z} + \frac{1}{3\alpha^2}\frac{\partial^2 m}{\partial t^2} \\
&\rho_c = \frac{L_{12}}{L_{11}} \\
&c = \frac{1}{\sqrt{\varepsilon\mu}} \\
&\alpha = \sqrt{\frac{K_f}{\rho}}
\end{aligned}
\quad . \qquad \text{(A.8)}
$$

Assume 1D solutions of the type

$$
\begin{aligned}
p(x,t) &= \frac{1}{2\pi}\int_{-\infty}^{\infty} d\omega \frac{1}{2\pi}\int_{-\infty}^{\infty} dk\, P(k,\omega) exp(-ikz + i\omega t) \\
e(x,t) &= \frac{1}{2\pi}\int_{-\infty}^{\infty} d\omega \frac{1}{2\pi}\int_{-\infty}^{\infty} dk\, E(k,\omega) exp(-ikz + i\omega t)
\end{aligned}
\qquad \text{(A.9)}
$$

The moment source is of the form,

$$
\begin{aligned}
m(z,t) &= s(t)\delta(z - z_0) \\
&= \frac{1}{2\pi}\int_{-\infty}^{\infty} d\omega \frac{1}{2\pi}\int_{-\infty}^{\infty} dk S(k,\omega) exp[-ikz + i\omega t] \\
S(k,\omega) &= \frac{1}{2\pi}\int_{-\infty}^{\infty} dt \int_{-\infty}^{\infty} dz s(t)\delta(z - z_0) exp[ikz - i\omega t]' \\
&= \int_{-\infty}^{\infty} dt s(t) exp(ikz_0 - i\omega t) = S(\omega) exp(ikz_0)
\end{aligned}
\qquad \text{(A.10)}
$$

where the strength of the source is included in *S*. For now we will set the impressed current density equal to zero, we will examine a non zero current later.

This leads to expressions for the electric field and pressure

$$\frac{\partial^2 e}{\partial z^2}-\frac{1}{c^2}\frac{\partial^2 e}{\partial t^2}-\mu\sigma\frac{\partial e}{\partial t}=-\mu L_{21}\frac{\partial^2 p}{\partial z\partial t}$$

$$\frac{\partial^2 p}{\partial z^2}-\frac{1}{\alpha^2}\frac{\partial^2 p}{\partial t^2}=\frac{\partial f}{\partial z}+\frac{1}{3\alpha^2}\frac{\partial^2 m}{\partial t^2}$$

$$\left[-k^2+\frac{\omega^2}{c^2}-i\mu\sigma\omega\right]E(k,\omega)=\omega k\mu L_{21}P(k,\omega)$$

$$\left[-k^2+\frac{\omega^2}{\alpha^2}\right]P(k,\omega)=-\frac{\omega^2}{3\alpha^2}S(\omega)exp(ikz_0)-ik\rho_c E(k,\omega)$$

$$\left[k^2-\left(\frac{\omega^2}{c^2}-i\mu\sigma\omega\right)\right]E(k,\omega)=-\omega k\mu L_{21}P(k,\omega)$$

$$\left[k^2-\frac{\omega^2}{\alpha^2}\right]P(k,\omega)=\frac{\omega^2}{3\alpha^2}S(\omega)exp(ikz_0)+ik\rho_c E(k,\omega)$$

$$(k-\vartheta)(k+\vartheta)E(k,\omega)-\omega k\mu L_{21}P(k,\omega)=0$$

$$-ik\rho_c E(k,\omega)+(k-\varphi)(k+\varphi)P(k,\omega)=\frac{\omega^2}{3\alpha^2}S(\omega)exp(ikz_0)$$

$$\vartheta^2=\frac{\omega^2}{c^2}-i\mu\sigma\omega,\qquad \varphi^2=\frac{\omega^2}{\alpha^2}$$

$$E(k,\omega)=\frac{\begin{vmatrix}0 & -\omega k\mu L_{21}\\ \frac{\omega^2}{3\alpha^2}S(\omega)exp(ikz_0) & (k-\varphi)(k+\varphi)\end{vmatrix}}{(k-\vartheta)(k+\vartheta)(k-\varphi)(k+\varphi)+ik^2\omega\rho_c\mu L_{21}}$$

$$E(k,\omega)=\frac{\omega^3\mu L_{21}}{3\alpha^2}\frac{kS(\omega)exp(ikz_0)}{(k-\vartheta)(k+\vartheta)(k-\varphi)(k+\varphi)+ik^2\omega\rho_c\mu L_{21}}$$

$$P(k,\omega)=\frac{\begin{vmatrix}(k-\vartheta)(k+\vartheta) & 0\\ -ik\rho_c & \frac{\omega^2}{3\alpha^2}S(\omega)exp(ikz_0)\end{vmatrix}}{(k-\vartheta)(k+\vartheta)(k-\varphi)(k+\varphi)+ik^2\omega\rho_c\mu L_{21}}$$

$$P(k,\omega)=\frac{(k-\vartheta)(k+\vartheta)\frac{\omega^2}{3\alpha^2}S(\omega)exp(ikz_0)}{(k-\vartheta)(k+\vartheta)(k-\varphi)(k+\varphi)+ik^2\omega\rho_c\mu L_{21}}$$

$$P(k,\omega)=\frac{\omega^2}{3\alpha^2}\frac{(k-\vartheta)(k+\vartheta)S(\omega)exp(ikz_0)}{(k-\vartheta)(k+\vartheta)(k-\varphi)(k+\varphi)+ik^2\omega\rho_c\mu L_{21}}$$

Recapping

$$\begin{aligned}E(k,\omega)&=\frac{\omega^3\mu L_{21}}{3\alpha^2}\frac{kS(\omega)exp(ikz_0)}{(k-\vartheta)(k+\vartheta)(k-\varphi)(k+\varphi)+ik^2\omega\rho_c\mu L_{21}}\\ P(k,\omega)&=\frac{\omega^2}{3\alpha^2}\frac{(k-\vartheta)(k+\vartheta)S(\omega)exp(ikz_0)}{(k-\vartheta)(k+\vartheta)(k-\varphi)(k+\varphi)+ik^2\omega\rho_c\mu L_{21}}\end{aligned}\ . \qquad \text{(A.11)}$$

As a first "cut" for simplicity ignore term containing $\rho_c \mu L_{21}$. Thus

$$E(k,\omega) = \mu L_{21} \frac{\omega^3}{3\alpha^2} \frac{kS(\omega)exp(ikz_0)}{(k-\vartheta)(k+\vartheta)(k-\varphi)(k+\varphi)}$$
$$P(k,\omega) = \frac{(k-\vartheta)(k+\vartheta)\frac{\omega^2}{\alpha^2}S(k,\omega)}{(k-\varphi)(k+\varphi)(k-\vartheta)(k+\vartheta)} = \frac{\omega^2}{3\alpha^2}\frac{S(\omega)exp(ikz_0)}{(k-\varphi)(k+\varphi)} \quad . \qquad \text{(A.12)}$$

Pressure uncouples from the electric field, but the electric field depends upon the pressure as a sourcing function.

To solve for the electric and pressure, we move the poles off the axis

$$p(z,t) = \frac{1}{2\pi}\int_{-\infty}^{\infty} d\omega \frac{1}{2\pi}\int_{-\infty}^{\infty} dk \left[\frac{\omega^2}{3\alpha^2}\frac{S(\omega)exp(ikz_0)}{(k-\varphi+i\varepsilon)(k+\varphi-i\varepsilon)}\right] exp(-ikz+i\omega t)$$
$$= \frac{1}{2\pi}\int_{-\infty}^{\infty} d\omega \frac{1}{2\pi}\int_{-\infty}^{\infty} dk \left[\frac{\omega^2}{3\alpha^2}\frac{S(\omega)}{(k-\varphi+i\varepsilon)(k+\varphi-i\varepsilon)}\right] exp(-ik(z-z_0)+i\omega t) \quad . \qquad \text{(A.13)}$$

$$k = k' + ik''$$
$$-i(k'+ik'')(z-z_0) = -ik'(z-z_0) + k''(z-z_0) \quad .$$
(A.14)

In order for the solutions to remain finite, for $z < z_0$ close over the upper half-plane and for $z \geq z_0$ close over the bottom half-plane. Thus we have for the poles.

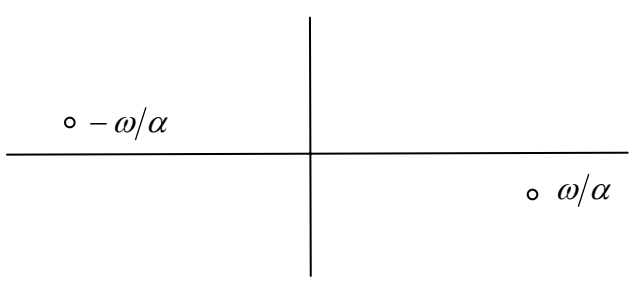

$$P(k,\omega)=\frac{\omega^2}{3\alpha^2}\frac{S(\omega)exp(ikz_0)}{(k-\varphi)(k+\varphi)}$$

$$p(z,t)=\begin{cases}\frac{1}{2\pi}\int_{-\infty}^{\infty}d\omega\frac{2\pi i}{2\pi}\left[\frac{\omega^2}{3\alpha^2}\frac{S(\omega)}{-2\varphi}\right]exp(i\varphi(z-z_0)+i\omega t) & , \quad z<z_0\\ \frac{-1}{2\pi}\int_{-\infty}^{\infty}d\omega\frac{2\pi i}{2\pi}\left[\frac{\omega^2}{3\alpha^2}\frac{S(\omega)}{2\varphi}\right]exp(-i\varphi(z-z_0)+i\omega t), \quad z\geq z_0\end{cases}$$

$$p(z,t)=\begin{cases}\frac{-i}{4\pi}\int_{-\infty}^{\infty}d\omega\frac{\omega}{3\alpha}S(\omega)exp\left[i\omega\left(t+\frac{z-z_0}{\alpha}\right)\right], & z<z_0\\ \frac{-i}{4\pi}\int_{-\infty}^{\infty}d\omega\frac{\omega}{3\alpha}S(\omega)exp\left[i\omega\left(t-\frac{z-z_0}{\alpha}\right)\right], & z\geq z_0\end{cases} \tag{A.15}$$

$$p(z,t)=-\frac{1}{3\alpha}\frac{i}{4\pi}\int_{-\infty}^{\infty}d\omega\omega S(\omega)exp\left[i\omega\left(t-sgn(z-z_0)\frac{|z-z_0|}{\alpha}\right)\right]$$

$$E(k,\omega)=-\mu L_{21}\frac{\omega^3}{3\alpha^2}\frac{kS(\omega)exp(ikz_0)}{(k-\vartheta)(k+\vartheta)(k-\varphi)(k+\varphi)} \tag{A.16}$$

$$e(z,t)=\frac{i\mu L_{21}}{4\pi}\int_{-\infty}^{\infty}d\omega\frac{\omega^3}{3\alpha^2}S(\omega)$$
$$\times\left[\frac{exp[-i\,sgn(z-z_0)\vartheta|(z-z_0)|+i\omega t]-exp[-i\,sgn(z-z_0)\varphi|(z-z_0)|+i\omega t]}{(\vartheta-\varphi)(\vartheta+\varphi)}\right] \tag{A.17}$$

From equations (A.15-A.17) it is clear that even though the pressure is decoupled, the electric field is not decoupled from the pressure.

We now focus our attention to retaining the $\rho_c\mu L_{21}$ term. The resulting coupled system of equations is

$$E(k,\omega)=\frac{\omega^3\mu L_{21}}{3\alpha^2}\frac{kS(\omega)exp(ikz_0)}{(k-\vartheta)(k+\vartheta)(k-\varphi)(k+\varphi)-ik^2\omega\rho_c\mu L_{21}}$$

$$P(k,\omega)=\frac{\omega^2}{3\alpha^2}\frac{(k-\vartheta)(k+\vartheta)S(\omega)exp(ikz_0)}{(k-\vartheta)(k+\vartheta)(k-\varphi)(k+\varphi)-ik^2\omega\rho_c\mu L_{21}}$$

From the above equations, there are four poles in the expressions for $E(k,\omega)$ and $P(k,\omega)$. Thus simplifying the equations

$$
\begin{aligned}
&(k-\vartheta)(k+\vartheta)(k-\varphi)(k+\varphi)-ik^2\rho_c\omega\mu L_{21}\\
&=\left(k^2-\vartheta^2\right)\left(k^2-\varphi^2\right)-ik^2\rho_c\omega\mu L_{21}\\
&=k^4-k^2\left(\vartheta^2+\varphi^2\right)+\vartheta^2\varphi^2-ik^2\rho_c\omega\mu L_{21}\\
&=k^4-k^2\left(\vartheta^2+\varphi^2+i\rho_c\omega\mu L_{21}\right)+\vartheta^2\varphi^2\\
&k^2=\frac{1}{2}\left[\vartheta^2+\varphi^2+i\rho_c\omega\mu L_{21}\pm\sqrt{\left(\vartheta^2+\varphi^2+i\rho_c\omega\mu L_{21}\right)^2-4\vartheta^2\varphi^2}\right]\\
&k^2=A\pm B\\
&k^2-A-B=k^2-(A+B)=\left(k-\sqrt{A+B}\right)\left(k+\sqrt{A+B}\right)=(k-M_1)(k+M_1)\\
&M_1=\sqrt{A+B}\\
&k^2-A+B=k^2-(A-B)\left(k-\sqrt{A-B}\right)\left(k+\sqrt{A-B}\right)=(k-M_2)(k+M_2)\\
&M_2=\sqrt{A-B}\\
&A=\frac{\vartheta^2+\varphi^2+i\rho_c\omega\mu L_{21}}{2},B=\frac{\sqrt{\left(\vartheta^2+\varphi^2+i\rho_c\omega\mu L_{21}\right)^2-4\vartheta^2\varphi^2}}{2}\\
&\varphi=\frac{\omega}{\alpha}\\
&\vartheta=\frac{\omega}{c}\sqrt{1-ic^2\mu_0\sigma/\omega}
\end{aligned}
\tag{A.18}
$$

Therefore

$$
\begin{aligned}
&E(k,\omega)=\frac{\omega^3\mu L_{21}}{3\alpha^2}\frac{kS(\omega)exp(ikz_0)}{(k-\vartheta)(k+\vartheta)(k-\varphi)(k+\varphi)-ik^2\omega\rho_c\mu L_{21}}\\
&E(k,\omega)=\frac{\omega^3\mu L_{21}}{3\alpha^2}\frac{kS(\omega)exp(ikz_0)}{(k-M_1)(k+M_1)(k-M_2)(k+M_2)}\\
&P(k,\omega)=\frac{\omega^2}{3\alpha^2}\frac{(k-\vartheta)(k+\vartheta)S(\omega)exp(ikz_0)}{(k-\vartheta)(k+\vartheta)(k-\varphi)(k+\varphi)-ik^2\omega\rho_c\mu L_{21}}\\
&P(k,\omega)=\frac{\omega^2}{3\alpha^2}\frac{(k-\vartheta)(k+\vartheta)S(\omega)exp(ikz_0)}{(k-M_1)(k+M_1)(k-M_2)(k+M_2)}
\end{aligned}
\tag{A.19}
$$

$$
\begin{aligned}
&E(k,\omega)=\frac{\omega^3\mu L_{21}}{3\alpha^2}\frac{kS(\omega)exp(ikz_0)}{(k-M_1)(k+M_1)(k-M_2)(k+M_2)}\\
&e(z,t)=\frac{\mu L_{21}}{2\pi}\int_{-\infty}^{\infty}d\omega\frac{1}{2\pi}\int_{-\infty}^{\infty}dk\frac{\omega^3}{3\alpha^2}\frac{kS(\omega)exp(-ik(z-z_0)+i\omega t)}{(k-M_1)(k+M_1)(k-M_2)(k+M_2)}
\end{aligned}
$$

$$e(z,t)=\frac{i\mu L_{21}}{4\pi}\int_{-\infty}^{\infty}d\omega\left(\frac{\omega^3}{3\alpha^2}S(\omega)\right)$$
$$\times\left[\frac{exp\left[-i\,sgn(z-z_0)M_1|z-z_0|+i\omega t\right]-exp\left[-i\,sgn(z-z_0)M_2|z-z_0|+i\omega t\right]}{(M_1-M_2)(M_1+M_2)}\right]$$

(A.20)

$$P(k,\omega)=\frac{\omega^2}{3\alpha^2}\frac{(k-\vartheta)(k+\vartheta)S(\omega)exp(ikz_0)}{(k-M_1)(k+M_1)(k-M_2)(k+M_2)}$$
$$p(z,t)=\frac{1}{2\pi}\int_{-\infty}^{\infty}d\omega\frac{1}{2\pi}\int_{-\infty}^{\infty}dkP(k,\omega)exp\left[-ikz+i\omega t\right]$$
$$=\frac{1}{2\pi}\int_{-\infty}^{\infty}d\omega\frac{1}{2\pi}\int_{-\infty}^{\infty}dk\frac{\omega^2}{3\alpha^2}\frac{(k-\vartheta)(k+\vartheta)S(\omega)exp\left[-ik(z-z_0)+i\omega t\right]}{(k-M_1)(k+M_1)(k-M_2)(k+M_2)}$$

$$p(z,t)=-i\frac{1}{4\pi}\int_{-\infty}^{\infty}d\omega\frac{\omega^2}{3\alpha^2}S(\omega)\frac{1}{(M_1-M_2)(M_1+M_2)}$$
$$\times\left[\begin{array}{c}\dfrac{(M_1-\vartheta)(M_1+\vartheta)exp\left[-i\,sgn(z-z_0)M_1|z-z_0|+i\omega t\right]}{M_1}\\ -\dfrac{(M_2-\vartheta)(M_2+\vartheta)exp\left[-i\,sgn(z-z_0)M_2|z-z_0|+i\omega t\right]}{M_2}\end{array}\right]$$

(A.21)

The equations for an electric source with no pressure source become

$$\frac{\partial^2 e}{\partial z^2}-\frac{1}{c^2}\frac{\partial^2 e}{\partial t^2}-\mu\sigma\frac{\partial e}{\partial t}=-\mu L_{21}\frac{\partial^2 p}{\partial z\partial t}+\mu\frac{\partial j^{imp}}{\partial t}$$
$$\frac{\partial^2 p}{\partial z^2}-\frac{1}{\alpha^2}\frac{\partial^2 p}{\partial t^2}=\frac{\partial f}{\partial z}$$

(A.22)

which become in Fourier space

$$\left(k^2-\frac{\omega^2}{c^2}+i\omega\mu\sigma\right)E(k,\omega)+\omega k\mu L_{12}P(k,\omega)=-i\omega\mu J(\omega)exp(ikz_0)$$

$$-ik\rho_c E(k,\omega)+\left(k^2-\frac{\omega^2}{\alpha^2}\right)P(k,\omega)=0$$

$$E(k,\omega)=\frac{\begin{vmatrix}-i\omega\mu J(\omega)exp(ikz_0) & \omega^2\mu L_{12}\\ 0 & (k-\varphi)(k+\varphi)\end{vmatrix}}{(k-\vartheta)(k+\vartheta)(k-\varphi)(k+\varphi)+ik^2\omega\rho_c\mu L_{12}}$$

$$E(k,\omega)=-i\omega\mu\frac{(k-\varphi)(k+\varphi)J(\omega)exp(ikz_0)}{(k-\vartheta)(k+\vartheta)(k-\varphi)(k+\varphi)+ik^2\omega\rho_c\mu L_{12}}$$

$$P(k,\omega)=\frac{\begin{vmatrix}(k-\vartheta)(k+\vartheta) & -i\omega\mu J(\omega)exp(ikz_0)\\ -ik\rho_c & 0\end{vmatrix}}{(k-\vartheta)(k+\vartheta)(k-\varphi)(k+\varphi)+ik^2\omega\rho_c\mu L_{12}}$$

$$P(k,\omega)=\frac{-\omega\mu k\rho_c J(\omega)exp(ikz_0)}{(k-\vartheta)(k+\vartheta)(k-\varphi)(k+\varphi)+ik^2\omega\rho_c\mu L_{12}}$$

$$E(k,\omega)=-i\omega\mu\frac{(k-\varphi)(k+\varphi)J(\omega)exp(ikz_0)}{(k-\vartheta)(k+\vartheta)(k-\varphi)(k+\varphi)+ik^2\omega\rho_c\mu L_{12}}$$

$$E(k,\omega)=-i\omega\mu\frac{(k-\varphi)(k+\varphi)J(\omega)exp(ikz_0)}{(k-M_1)(k+M_1)(k-M_2)(k+M_2)}$$

$$P(k,\omega)=\frac{-\omega\mu k\rho_c J(\omega)exp(ikz_0)}{(k-\vartheta)(k+\vartheta)(k-\varphi)(k+\varphi)+ik^2\omega\rho_c\mu L_{12}}$$

$$P(k,\omega)=-\mu\rho_c\frac{\omega kJ(\omega)exp(ikz_0)}{(k-M_1)(k+M_1)(k-M_2)(k+M_2)}$$

$$E(k,\omega)=-i\omega\mu\frac{(k-\varphi)(k+\varphi)J(\omega)exp(ikz_0)}{(k-M_1)(k+M_1)(k-M_2)(k+M_2)}$$

$$e(z,t)=\frac{1}{2\pi}\int_{-\infty}^{\infty}d\omega\frac{1}{2\pi}\int_{-\infty}^{\infty}dkE(k,\omega)exp(-ikz+i\omega t)$$

$$=-i\mu\frac{1}{2\pi}\int_{-\infty}^{\infty}d\omega\omega\frac{1}{2\pi}\int_{-\infty}^{\infty}dk\frac{(k-\varphi)(k+\varphi)J(\omega)exp[-ik(z-z_0)+i\omega t]}{(k-M_1)(k+M_1)(k-M_2)(k+M_2)}$$

$$e(z,t) = -\mathrm{sgn}(z - z_0)\mu \frac{1}{4\pi} \int_{-\infty}^{\infty} d\omega\omega \frac{1}{(M_1 - M_2)(M_1 + M_2)}$$
$$\times \left[\begin{array}{l} \dfrac{(M_1 - \varphi)(M_1 + \varphi)J(\omega)\exp[-iM_1(z - z_0) + i\omega t]}{M_1} \\ -\dfrac{(M_2 - \varphi)(M_2 + \varphi)J(\omega)\exp[-iM_2(z - z_0) + i\omega t]}{M_2} \end{array} \right] \quad \text{(A.23)}$$

We have $\vartheta = \frac{\omega}{c}\sqrt{1 - ic^2\mu_0\sigma/\omega}$, and for $z < z_0$, we have must take $\vartheta = \frac{\omega}{c}\sqrt{1 + ic^2\mu_0\sigma/\omega}$. Thus we can write $\vartheta = \frac{\omega}{c}\sqrt{1 - \mathrm{sgn}(z - z_0)ic^2\mu_0\sigma/\omega}$

$$P(k,\omega) = -\mu\rho_c \frac{\omega k J(\omega) exp(ikz_0)}{(k - M_1)(k + M_1)(k - M_2)(k + M_2)}$$

$$p(z,t) = \frac{1}{2\pi}\int_{-\infty}^{\infty} d\omega \frac{1}{2\pi}\int_{-\infty}^{\infty} dk P(k,\omega) exp(-ikz + i\omega t)$$
$$= -\mu\rho_c \frac{1}{2\pi}\int_{-\infty}^{\infty} d\omega \frac{1}{2\pi}\int_{-\infty}^{\infty} dk \frac{\omega k J(\omega) exp[-ik(z - z_0) + i\omega t]}{(k - M_1)(k + M_1)(k - M_2)(k + M_2)}$$

$$p(z,t) = i\mu\rho_c \frac{1}{4\pi}\int_{-\infty}^{\infty} d\omega\omega$$
$$\times \left[\frac{J(\omega) exp[-i\, sgn(z - z_0)M_1|z - z_0| + i\omega t] - J(\omega) exp[-i\, sgn(z - z_0)M_2|z - z_0| + i\omega t]}{(M_1 - M_2)(M_1 + M_2)} \right]$$
$$\text{(A.24)}$$

Appendix B

Analytic Solutions for 1D Plane Waves

The purpose of this note is to demonstrate how one can use a fictitious dielectric constant to increase the time step in a finite-difference algorithm where the displacement current term is retained. Here we restrict the calculations to 1D where we can obtain an analytic solution.

Maxwell's equations for an electrically conducting medium are:

$$\begin{aligned} \nabla \times \mathbf{e} &= -\partial_t \mathbf{b} \\ \nabla \times \mathbf{h} &= \partial_t \mathbf{d} + \mathbf{j} \end{aligned} \quad \text{(B.1)}$$

where constitutive relations are:

$$\begin{aligned}\mathbf{b} &= \mu_0 \mathbf{h} \\ \mathbf{d} &= \varepsilon \mathbf{e}\end{aligned} \quad . \tag{B.2}$$

where $\mu_0 = 4\pi \times 10^{-7}\, henrys/m$, the magnetic permeability of free space. The displacement current term comes from $\partial_t \mathbf{d}$. In the following we will restrict the magnetic permeability to that of free space. The current consists of Ohm's law conduction and the impressed current (here we are ignoring the seismo-electric effect)

$$\mathbf{j} = \sigma \mathbf{e} + \mathbf{j}^{imp} . \tag{B.3}$$

Thus we have from equations (B.1-B.3)

$$\begin{aligned}\varepsilon \partial_t \mathbf{e} + \sigma \mathbf{e} - \nabla \times \mathbf{h} &= -\mathbf{j}^{imp} \\ \mu_0 \partial_t \mathbf{h} + \nabla \times \mathbf{e} &= 0\end{aligned} \quad . \tag{B.4}$$

We have ignored the seismo-electric effect and have assumed ε and μ_0 independent of time; *i.e.*, independent of frequency.

Consider the plane-wave approximation for orthogonal **e** and **h**, e_x and h_y.

$$\begin{aligned}&\varepsilon \partial_t e_x + \sigma e_x - (\nabla \times \mathbf{h})_x = j_x^{imp} \\ &\varepsilon \partial_t e_x + \sigma e_x - \left[\partial_y h_z - \partial_z h_y\right] = j_x^{imp} \\ &\varepsilon \partial_t e_x + \sigma e_x + \partial_z h_y = j_x^{imp} \\ &\mu_0 \partial_t h_y + (\nabla \times \mathbf{e})_y = 0 \\ &\mu_0 \partial_t h_y + \left[\partial_z e_x - \partial_x e_z\right] = 0 \\ &\mu_0 \partial_t h_y + \partial_z e_x = 0\end{aligned} \quad . \tag{B.5}$$

Assume solutions of the form

$\sim \exp(-ikz + i\omega t)$

$$\begin{aligned}e_x(z,t) &= \frac{1}{2\pi}\int_{-\infty}^{\infty} d\omega \frac{1}{2\pi}\int_{-\infty}^{\infty} dk E(k,\omega)\exp(-ikz + i\omega t) \\ h_y(z,t) &= \frac{1}{2\pi}\int_{-\infty}^{\infty} d\omega \frac{1}{2\pi}\int_{-\infty}^{\infty} dk H(k,\omega)\exp(-ikz + i\omega t) \\ j_x^{imp}(z_0,t) &= \frac{1}{2\pi}\int_{-\infty}^{\infty} d\omega \frac{1}{2\pi}\int_{-\infty}^{\infty} dk J(k,\omega)\exp(-ikz_0 + i\omega t)\end{aligned} \quad . \tag{B.6}$$

Thus we have using equations (B.5) and (B.6)

$$\begin{bmatrix} i\varepsilon\omega+\sigma & -ik \\ -ik & i\mu_0\omega \end{bmatrix}\begin{bmatrix} E(k,\omega) \\ H(k,\omega) \end{bmatrix}=\begin{bmatrix} J(k,\omega) \\ 0 \end{bmatrix}$$

$$E(k,\omega)=\frac{\begin{vmatrix} J(k,\omega) & -ik \\ 0 & i\mu\omega \end{vmatrix}}{\begin{vmatrix} i\varepsilon\omega+\sigma & -ik \\ -ik & i\mu_0\omega \end{vmatrix}}=\frac{i\mu\omega J(k,\omega)}{-\varepsilon\mu_0\omega^2+i\mu_0\omega\sigma+k^2}=\frac{i\mu\omega J(k,\omega)}{k^2-\vartheta^2}=\frac{i\mu\omega J(k,\omega)}{(k-\vartheta)(k+\vartheta)}$$

$$\vartheta^2=\left(\varepsilon\mu_0\omega^2-i\mu_0\omega\sigma\right)\quad \vartheta=\sqrt{\varepsilon\mu_0\omega^2-i\mu_0\omega\sigma} \tag{B.7}$$

$$v=1\big/\sqrt{\varepsilon\mu_0}$$

$$H(k,\omega)=\frac{\begin{vmatrix} i\varepsilon\omega+\sigma & J(k,\omega) \\ -ik & 0 \end{vmatrix}}{(k-\vartheta)(k+\vartheta)}=\frac{ikJ(k,\omega)}{(k-\vartheta)(k+\vartheta)}$$

The $\varepsilon\mu_0\omega^2$ term in ϑ is the so-called displacement current term arising from $\partial_t\mathbf{d}$.

To solve for the electric and magnetic fields, we move the poles off the axis

$$\begin{aligned} e(z,t)&=\frac{1}{2\pi}\int_{-\infty}^{\infty}d\omega\frac{1}{2\pi}\int_{-\infty}^{\infty}dkE(k,\omega)exp(-ikz+i\omega t) \\ &=\frac{1}{2\pi}\int_{-\infty}^{\infty}d\omega\frac{1}{2\pi}\int_{-\infty}^{\infty}dk\frac{i\mu\omega J(k,\omega)exp(ikz_0)}{(k-\vartheta+i\delta)(k+\vartheta-i\delta)}exp(-ikz+i\omega t) \end{aligned}. \tag{B.8}$$

$$\begin{aligned} &k=k'+ik'' \\ &-i(k'+ik'')(z-z_0)=-ik'(z-z_0)+k''(z-z_0) \end{aligned} \tag{B.9}$$

In order for the solutions to remain finite, for $z<z_0$ close over the upper half-plane $(k''>0)$ and for $z\geq z_0$ $(k''<0)$ close over the bottom half-plane. Thus we have for the poles.

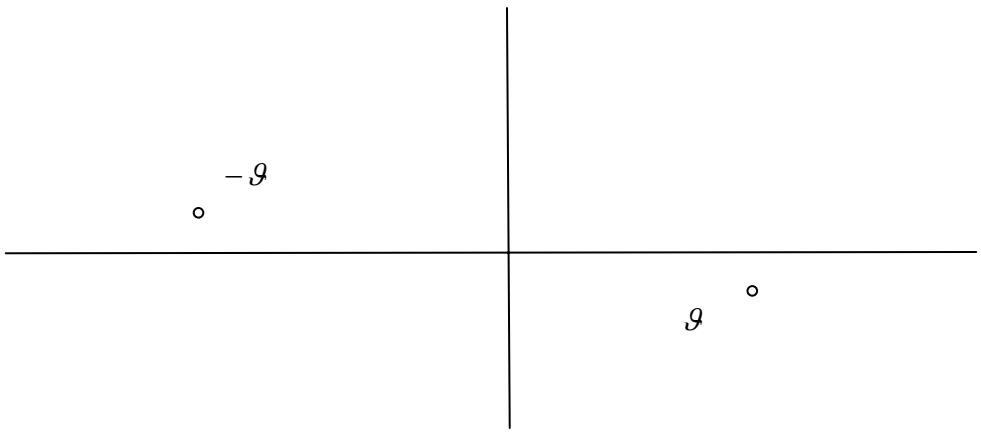

$$
\begin{aligned}
e(z,t) &= \frac{1}{2\pi}\int_{-\infty}^{\infty} d\omega \frac{1}{2\pi}\int_{-\infty}^{\infty} dk E(k,\omega) exp(-ikz + i\omega t) \\
&= \frac{1}{2\pi}\int_{-\infty}^{\infty} d\omega \frac{1}{2\pi}\int_{-\infty}^{\infty} dk \frac{i\mu_0 \omega J(k,\omega) exp(ikz_0)}{(k-\varphi-i\delta)(k+\vartheta+i\delta)} exp(-ikz + i\omega t) \\
e(z,t) &= \frac{1}{2\pi}\int_{-\infty}^{\infty} d\omega \frac{2\pi i}{2\pi} \frac{i\mu_0 \omega J(\omega)}{-2\vartheta} exp[i\vartheta(z-z_0) + i\omega t] \\
e(z,t) &= \frac{\mu_0}{4\pi}\int_{-\infty}^{\infty} d\omega \vartheta exp[i\vartheta(z-z_0) + i\omega t], \quad z < z_0 \\
e(z,t) &= \frac{-1}{2\pi}\int_{-\infty}^{\infty} d\omega \frac{2\pi i}{2\pi} \frac{i\mu_0 \omega J(\omega)}{2\vartheta} exp[-i\vartheta(z-z_0) + i\omega t] \\
e(z,t) &= \frac{\mu_0}{4\pi}\int_{-\infty}^{\infty} d\omega \frac{\omega J(\omega)}{\vartheta} exp[-i\vartheta(z-z_0) + i\omega t], \quad z \geq z_0
\end{aligned}
\tag{B.10}
$$

We have

$$
e(z,t) = \frac{\mu_0}{4\pi}\int_{-\infty}^{\infty} d\omega \frac{\omega J(\omega)}{\vartheta} exp[-i\, sgn(z-z_0)\vartheta|z-z_0| + i\omega t], \; -\infty < z < \infty
$$

$$h(z,t)=\frac{1}{2\pi}\int_{-\infty}^{\infty}d\omega\frac{1}{2\pi}\int_{-\infty}^{\infty}dkH(k,\omega)exp(-ikz+i\omega t)$$

$$H(k,\omega)=\frac{ikJ(k,\omega)}{(k-\vartheta)(k+\vartheta)}$$

$$h(z,t)=\frac{1}{2\pi}\int_{-\infty}^{\infty}d\omega\frac{2\pi i}{2\pi}\frac{i(-\vartheta)J(\omega)}{-2\vartheta}exp(i\vartheta(z-z_0)+i\omega t)$$

$$h(z,t)=\frac{-1}{4\pi}\int_{-\infty}^{\infty}d\omega J(\omega)exp(i\vartheta(z-z_0)+i\omega t),\ z<z_0 \qquad \text{(B.11)}$$

$$h(z,t)=\frac{-1}{2\pi}\int_{-\infty}^{\infty}d\omega\frac{2\pi i}{2\pi}\frac{i\vartheta J(\omega)}{2\Theta}exp(-i\vartheta(z-z_0)+i\omega t)$$

$$h(z,t)=\frac{1}{4\pi}\int_{-\infty}^{\infty}d\omega J(\omega)exp(-i\vartheta(z-z_0)+i\omega t),\ z\geq z_0$$

We have

$$h(z,t)=\frac{sgn(z-z_0)}{4\pi}\int_{-\infty}^{\infty}d\omega J(\omega)exp\left[-i\,sgn(z-z_0)\vartheta|z-z_0|+i\omega t\right],-\infty<z<\infty$$

Equations (B.10) and (B.11) give us expressions for $e(z,t)$ and $h(z,t)$ where the impressed current waveform band limits the frequencies affecting ϑ (equation (B.7)). The band-limited waveform is particularly true for the seismo-electric effect where the seismic input wavelet is band limited.

Generally in EM exploration, we are interested in the so-called diffusion limit or quasi-static limit where from the expression for ϑ, $\varepsilon\omega << \sigma$. In order to use a reasonable time step in a finite-difference algorithm where we include the displacement current term ($\varepsilon\mu\omega^2$), we can decrease the wave speed given by $1/\sqrt{\varepsilon\mu_0}$ by increasing the electric permittivity, ε to a fictitious value without significantly altering the results. In terms of the dielectric constant κ, $\varepsilon=\kappa\varepsilon_0$ where ε_0 is the permittivity of free space with a value of $8.8540\times10^{-12}\ farads/m$. Using the notation of Wang and Hohmann (1993), we set γ to the fictitious value of ε. From actual calculations, we have found that a reasonable maximum value of γ is given by

$$\gamma_{\max}\leq\frac{\sigma}{2\pi f_{\max}}, \qquad \text{(B.12)}$$

where $f_{\max}$ is the frequency at 1% of the peak amplitude of the Fourier transform of the input waveform. The time step determined from equation (B.12) is the 3D Courant-Friedrichs-Levy (CFL) stability condition

$$\Delta t=\frac{\Delta x}{\sqrt{3}\times v}=\frac{\Delta x}{\sqrt{3}\times 1/\sqrt{\mu_0\gamma_{\max}}}=\frac{\Delta x\sqrt{\mu_0\gamma_{\max}}}{\sqrt{3}}. \qquad \text{(B.13)}$$

From equation (13) the minimum value of γ is given by

$$\gamma_{\min} = (3/\mu_0)(\Delta t/\Delta x)^2 . \tag{B.14}$$

agreeing with Wang and Hohmann (1993).

Appendix C

Air-Earth Interface in EM Modeling

The purpose of this document is to demonstrate the upward-continuation method at the air-earth interface used by Wang and Hohmann (1993). A simple upward-continuation boundary condition is implemented at the surface of the earth (Oristaglio and Hohmann, 1984). With this method it is not necessary to time-step the EM field in air, which would require a very small time step. To apply the upward-continuation to the staggered grid, the grid is extended by one grid level into the air. For the EM staggered grid, the electric fields reside on the edges of the fundamental cubic volume and the **b**-fields reside on the faces of the fundamental cubic volume. Thus b_x and b_y are computed at a level of half a grid spacing above the surface of the earth using b_z on the face of the cubic volume at the surface.

The divergence of **b** is zero and in air with no current sources,

$$\nabla \cdot \mathbf{b} = 0$$
$$\nabla \times \mathbf{b} = \mu_0 \varepsilon_0 \partial_t \mathbf{e}$$

Now take the curl of the second equation

$$\nabla \times (\nabla \times \mathbf{b}) = \mu_0 \varepsilon_0 \partial_t \nabla \times \mathbf{e} = -\mu_0 \varepsilon_0 \partial_t^2 \mathbf{b}$$
$$\nabla^2 \mathbf{b} = \mu_0 \varepsilon_0 \partial_t^2 \mathbf{b}$$

In the so-called quasi-static limit one takes $\nabla \times \mathbf{b} = 0$ resulting in $\nabla^2 \mathbf{b} = 0$. We will return to the case when we do not take the quasi static limit.

Gauss's law for scalar quantities *A* and *B*

$$\int dV \left[A \nabla^2 B - B \nabla^2 A \right] = \int dS \left[A \partial_n B - B \partial_n A \right]$$

Neglecting displacement currents in air, we have for the **b**-field,

$$\nabla^2 \mathbf{b} = 0, \quad \nabla \cdot \mathbf{b} = 0, \quad \nabla \times \mathbf{b} = 0$$

In the equation for scalars, let $b_i = B$ and $A = g(\mathbf{x},\mathbf{x}')$ satisfying the equation

$$\nabla^2 g(\mathbf{x},\mathbf{x}') = -\delta(\mathbf{x}-\mathbf{x}')$$

Thus we have when $\nabla^2 b_i = 0$

$$b_i(\mathbf{x}) = \int dS'\left[g(\mathbf{x},\mathbf{x}')\partial_{n'} b_i(\mathbf{x}') - b_i(\mathbf{x}')\partial_{n'} g(\mathbf{x},\mathbf{x}')\right]$$

We can choose the green's function $g(\mathbf{x},\mathbf{x}')$ or it's normal derivative to vanish on the surface S.

$$g_\pm(\mathbf{x},\mathbf{x}') = \frac{1}{\sqrt{(x-x')^2 + (y-y')^2 + (z \pm z')^2}} = \frac{1}{R_\pm}$$

For

$$g(\mathbf{x},\mathbf{x}')\big|_{z'=0} = \frac{1}{2}\left[g_-(\mathbf{x},\mathbf{x}') - g_+(\mathbf{x},\mathbf{x}')\right]\Big|_{z'=0} = 0$$

$$\partial_{n'} g(\mathbf{x},\mathbf{x}')\big|_{z'=0} = -\partial_{z'} g(\mathbf{x},\mathbf{x}')\big|_{z'=0} = \frac{1}{2}\left[-\frac{(z'-z)}{R_-^3} + \frac{(z'+z)}{R_+^3}\right]\Bigg|_{z'=0}$$

$$= \frac{z}{R^3}$$

$$R = \sqrt{(x-x')^2 + (y-y')^2 + z^2}$$

Or for

$$g(\mathbf{x},\mathbf{x}')\big|_{z'=0} = \frac{1}{2}\left[g_-(\mathbf{x},\mathbf{x}') + g_+(\mathbf{x},\mathbf{x}')\right]\Big|_{z'=0} = \frac{1}{R}$$

$$\partial_{n'} g(\mathbf{x},\mathbf{x}')\big|_{z'=0} = -\partial_{z'} g(\mathbf{x},\mathbf{x}')\big|_{z'=0} = \frac{1}{2}\left[-\frac{(z'-z)}{R_-^3} - \frac{(z'+z)}{R_+^3}\right]\Bigg|_{z'=0} = 0$$

$$R = \sqrt{(x-x')^2 + (y-y')^2 + z^2}$$

Thus we have for the components of **b**,

$$b_i(\mathbf{x}) = \int dS' \left[g(\mathbf{x},\mathbf{x}')\partial_{n'} b_i(\mathbf{x}') - b_i(\mathbf{x}')\partial_{n'} g(\mathbf{x},\mathbf{x}') \right]$$

$$b_i(\mathbf{x}) = \int dS' g(\mathbf{x},\mathbf{x}')\partial_{n'} b_i(\mathbf{x}')\Big|_{z'=0}, \quad g = g_- + g_+$$

or

$$b_i(\mathbf{x}) = -\int dS' \frac{1}{R(x,x')}\Bigg|_{z'=0} \partial_{z'} b_i(\mathbf{x}')$$

Define transform pairs in **x-k** space as

$$\mathbf{A}(\mathbf{k}) = \int d^3\mathbf{x}\, \mathbf{a}(\mathbf{x}) \exp(-i\mathbf{k}\cdot\mathbf{x})$$

$$\mathbf{a}(\mathbf{x}) = \frac{1}{(2\pi)^3} \int d^3\mathbf{k}\, \mathbf{A}(\mathbf{k}) \exp(i\mathbf{k}\cdot\mathbf{x})$$

In 2D we have

$$\mathbf{A}(k_x, k_y, z) = \int dx' \int dy'\, \mathbf{a}(x',y',z) \exp\left[-i(k_x x' + k_y y')\right]$$

$$\mathbf{a}(x,y,z) = \frac{1}{(2\pi)^2} \int dk_x \int dk_y\, \mathbf{A}(k_x, k_y, z) \exp\left[i(k_x x' + k_y y')\right]$$

Suppose we have

$$\nabla^2 g(\mathbf{x},\mathbf{x}') = -\delta(\mathbf{x}-\mathbf{x}')$$

$$G(k_x, k_y, z-z') = \frac{1}{2\pi} \int_{-\infty}^{\infty} dk_z \frac{e^{ik_z z}}{k_x^2 + k_y^2 + k_z^2} = \frac{e^{-u|z-z'|}}{2u}$$

$$u = \sqrt{k_x^2 + k_y^2}$$

$$g(\mathbf{x},\mathbf{x}') = \frac{1}{(2\pi)^2} \int_{-\infty}^{\infty} dk_x \int_{-\infty}^{\infty} dk_y \frac{e^{-u|z-z'|}}{2u} e^{ik_x x} e^{ik_y y}$$

$$\partial_{n'} g(\mathbf{x},\mathbf{x}') = -\partial_{z'} g(\mathbf{x},\mathbf{x}') = \frac{1}{2}\frac{1}{(2\pi)^2} \int_{-\infty}^{\infty} dk_x \int_{-\infty}^{\infty} dk_y e^{-u|z-z'|} e^{ik_x x} e^{ik_y y}$$

$$\frac{d|x|}{dx} = \begin{cases} -1, & x < 0 \\ undefined & x = 0 \\ +1, & x > 0 \end{cases}$$

Thus we have

$$b_i(\mathbf{x}) = \int dS' \left[g(\mathbf{x},\mathbf{x}')\partial_{n'} b_i(\mathbf{x}') - b_i(\mathbf{x}')\partial_{n'} g(\mathbf{x},\mathbf{x}') \right]$$

$$b_i(\mathbf{x}) = \int dS' g(\mathbf{x},\mathbf{x}')\partial_{n'} b_i(\mathbf{x}')\Big|_{z'=0}, \quad g = g_- + g_+$$

$$b_i(\mathbf{x}) = \int dx'dy' \frac{1}{(2\pi)^2} \int dk_x dk_y \left. \frac{e^{-\sqrt{(k_x^2+k_y^2)}|z-z'|}}{\sqrt{k_x^2+k_y^2}} \right|_{z'=0} e^{i(k_x x' + k_y y')}$$

$$\times \frac{1}{(2\pi)^2} \int dk_x' dk_y' \partial_{n'} B_i(k_x, k_y, z' \to 0) e^{i(k_x' x' + k_y' y')}$$

$$b_i(\mathbf{x}) = \frac{1}{(2\pi)^2} \int dk_x dk_y \frac{e^{-\sqrt{(k_x^2+k_y^2)}|z|}}{\sqrt{k_x^2+k_y^2}} \partial_{n'} B_i(k_x, k_y, z' \to 0)$$

$$or \;\; g = g_- - g_+$$

$$b_i(\mathbf{x}) = -z \int dx'dy' \frac{1}{(2\pi)^2} \int dk_x dk_y B_i(k_x, k_y, z' \to 0) e^{i(k_x x' + k_y y')}$$

$$\times \frac{1}{(2\pi)^2} \int dk_x' dk_y' \partial_{n'} \frac{e^{-\sqrt{(k_x'^2+k_y'^2)}|z|}}{\sqrt{k_x'^2+k_y'^2}} e^{i(k_x' x' + k_y' y')}$$

$$b_i(\mathbf{x}) = -z \frac{1}{(2\pi)^2} \int dk_x dk_y B_i(k_x, k_y, z' \to 0) \partial_{n'} \left. \frac{e^{-\sqrt{(k_x^2+k_y^2)}|z-z'|}}{\sqrt{k_x^2+k_y^2}} \right|_{z'=0}$$

$$= z \frac{1}{(2\pi)^2} \int dk_x dk_y B_i(k_x, k_y, z' \to 0) e^{-\sqrt{(k_x^2+k_y^2)}|z|}$$

We have

$$\nabla \cdot \mathbf{b} = \partial_x b_x + \partial_y b_y + \partial_z b_z = 0 \to -ik_x B_x - ik_y B_y + \partial_z B_z = 0$$

$$\nabla^2 b_i \to -k_x^2 B_i - k_y^2 B_i + \partial_{zz} B_i = 0$$

$$\nabla \times \mathbf{b} = 0, \Rightarrow \partial_y b_z = \partial_z b_y, \; \partial_z b_x = \partial_x b_z, \quad \partial_x b_y = \partial_y b_x$$

$$\partial_x \partial_y b_x + \partial_{yy} b_y + \partial_z \partial_y b_z = 0$$

$$\partial_{xx} b_y + \partial_{yy} b_y + \partial_{zz} b_y = 0$$

Thus

$$b_i(\mathbf{x}) = \int dS' g(\mathbf{x},\mathbf{x}')\partial_{n'} b_i(\mathbf{x}')\Big|_{z'=0}, \quad g = g_- + g_+$$

$$b_x(\mathbf{x}) = -\int dS' g(\mathbf{x},\mathbf{x}')\partial_{z'} b_x(\mathbf{x}') = -\int dS' g(\mathbf{x},\mathbf{x}')\partial_x b_z(\mathbf{x}')$$

$$b_y(\mathbf{x}) = -\int dS' g(\mathbf{x},\mathbf{x}')\partial_{z'} b_y(\mathbf{x}') = -\int dS' g(\mathbf{x},\mathbf{x}')\partial_y b_z(\mathbf{x}')$$

$$\partial_i b_z(\mathbf{x}) = \partial_i \frac{1}{(2\pi)^2}\int dk_x dk_y B_z(k_x, k_y, z' \to 0) e^{i(k_x x + k_y y)}$$

$$= \frac{1}{(2\pi)^2}\int dk_x dk_y (ik_i) B_z(k_x, k_y, z' \to 0) e^{i(k_x x + k_y y)}$$

$$b_x(\mathbf{x}) = -\int dx' dy' \frac{1}{(2\pi)^2}\int dk_x dk_y \frac{e^{-(k_x^2+k_y^2)|z-z'|}}{\sqrt{k_x^2+k_y^2}}\Bigg|_{z'=0} e^{i(k_x x + k_y y)}$$

$$\times \frac{1}{(2\pi)^2}\int dk'_x dk'_y \partial_{n'} B_x(k_x, k_y, z' \to 0) e^{i(k'_x x' + k'_y y')}$$

$$b_x(\mathbf{x}) = \frac{1}{(2\pi)^2}\int dk_x dk_y \frac{e^{-(k_x^2+k_y^2)|z-z'|}}{\sqrt{k_x^2+k_y^2}}\Bigg|_{z'=0} ik_x B_z(k_x, k_y, z' \to 0)$$

$$b_y(\mathbf{x}) = \frac{1}{(2\pi)^2}\int dk_x dk_y \frac{e^{-(k_x^2+k_y^2)|z-z'|}}{\sqrt{k_x^2+k_y^2}}\Bigg|_{z'=0} ik_y B_z(k_x, k_y, z' \to 0)$$

$$B_x(k_x, k_y, z = -h) = \frac{ik_x e^{-(k_x^2+k_y^2)h}}{\sqrt{k_x^2+k_y^2}} B_z(k_x, k_y, z' \to 0)$$

$$B_y(k_x, k_y, z = -h) = \frac{ik_y e^{-(k_x^2+k_y^2)h}}{\sqrt{k_x^2+k_y^2}} B_z(k_x, k_y, z' \to 0)$$

Agreeing with Wang & Hohmann (1993). Knowledge of b_z on the air-earth surface gives us b_x and b_y in the air.

The implementation of the equations for b_x and b_y for Wang and Hohmann (1993) required interpolating a non-uniform grid spanned by b_z onto a constant grid with spacing δ. The 2D Fourier transform of b_z, B_z, is then used to determine B_x and B_y in air. The resultant components are then Fourier transformed into the spatial *x*-*y* domain. Wang and Hohmann (1993) did not discuss what they did with the electric field components.

The electric fields reside on the edges of the fundamental volume and thus at the air-earth interface e_x and e_y are on the surface. e_z resides half a grid spacing below the surface. The components of the electric field that are tangential to the surface are continuous

across the air-earth interface. This means that for a full grid spacing above the air-earth interface, the tangential components have the same value as at the surface. Since in the quasi-static limit, no current traverses the air-earth interface, the value of e_z at the half grid spacing above the air-earth interface must be zero.

For the 2D case, Oristaglio and Hohmann (1984) assumed that the electric field in are obeyed

$$\partial_{xx} e_y + \partial_{zz} e_y = 0$$
$$\partial_y e_y = 0$$

The single component of the electric field is invariant in the *y*-direction.

Using

$$g(x,x')\big|_{z'=0} = \frac{1}{2}\left[g_-(x,x') - g_+(x,x')\right]\Big|_{z'=0} = 0$$
$$\partial_{n'} g(x,x')\big|_{z'=0} = -\partial_{z'} g(x,x')\big|_{z'=0} = \frac{1}{2}\left[-\frac{(z'-z)}{R_-^3} + \frac{(z'+z)}{R_+^3}\right]\Bigg|_{z'=0}$$
$$= \frac{z}{R^3}$$
$$R = \sqrt{(x-x')^2 + z^2}$$

$$(\partial_{xx}+\partial_{zz})g=-\delta(x-x')\delta(z-z')$$
$$(\partial_{xx}+\partial_{zz})\frac{1}{2\pi}\int dk_x G(k_x;z,z')exp(ik_x x)=-\frac{1}{2\pi}\int dk_x\, exp[ik_x(x-x')]\delta(z-z')$$
$$(-k_x^2+\partial_{zz})G(k_x;z,z')=-exp[-ik_x x']\delta(z-z')$$
$$(-k_x^2+\partial_{zz})G(k_x;z,z')=$$

$$G=\frac{e^{-k_x|z-z'|}}{k_x}$$
$$g=\frac{1}{2\pi}\int dk_x\frac{e^{-k_x|z-z'|}}{k_x}e^{ik_x(x-x')}$$
$$G(k_x,z,z')=\int dxg(x,x';z,z')e^{-ik_x(x-x')}=\int dx\frac{1}{2\pi}\int dk_x'\frac{e^{-k_x'|z-z'|}}{k_x'}e^{ik_x'(x-x')}e^{-ik_x(x-x')}$$
$$=\frac{e^{-k_x|z-z'|}}{k_x}$$
$$G(k_x,k_y,z-z')=\frac{1}{2\pi}\int_{-\infty}^{\infty}dk_z\frac{e^{ik_z z}}{k_x^2+k_y^2+k_z^2}=\frac{e^{-u|z-z'|}}{2u}$$
$$u=\sqrt{k_x^2+k_y^2}$$

$$\mathbf{A}(k_x,k_y,z)=\int dx'\int dy'\,\mathbf{a}(x',y',z)\exp[-i(k_x x'+k_y y')]$$
$$\mathbf{a}(x,y,z)=\frac{1}{(2\pi)^2}\int dk_x\int dk_y\mathbf{A}(k_x,k_y,z)\exp[i(k_x x+k_y y)]$$

Vector form of Gauss's theorem

$$\int dV[\mathbf{b}\cdot\nabla\times\nabla\mathbf{a}-\mathbf{a}\cdot\nabla\times\nabla\mathbf{b}]=\int dS[(\mathbf{n}\times\mathbf{a})\cdot\nabla\times\mathbf{b}-(\mathbf{n}\times\mathbf{b})\cdot\nabla\times\mathbf{a}]$$

$$\nabla\times e=0\ \Rightarrow\partial_y e_z=\partial_z e_y,\ \partial_z e_x=\partial_x e_z,\ \partial_x e_y=\partial_y e_x$$

For my 2D case we are solving for e_x, e_z, h_y. We have $\partial_z e_x=\partial_x e_z$. We have e_x calculated at the surface. We can upward continue e_x up to next half grid point and calculate e_z

If we assume $\nabla\cdot\mathbf{e}=0$, $\partial_z e_z=-\partial_x e_x$ in air; *i.e.*, no polarization charges

Thus from $\nabla^2 e_i = 0$

$$e_i(\mathbf{x}) = \int dS' g(\mathbf{x},\mathbf{x}')\partial_{n'} e_i(\mathbf{x}')\Big|_{z'=0}, \quad g = g_- + g_+$$
$$e_z(\mathbf{x}) = -\int dS' g(\mathbf{x},\mathbf{x}')\partial_{z'} e_z(\mathbf{x}') = \int dS' g(\mathbf{x},\mathbf{x}')\partial_x e_x(\mathbf{x}')$$
$$e_z(\mathbf{x}) = \int dx' \frac{1}{2\pi}\int dk_x \frac{e^{-k_x|z-z'|}}{k_x}\Bigg|_{z'=0} e^{ik_x(x-x')}\frac{1}{2\pi}\int dk_x' ik_x' E_x(k_x', z'=0)e^{ik_x' x'}$$
$$\frac{1}{2\pi}\int dk_x E_z(k_x, z)e^{ik_x x} = \frac{1}{2\pi}\int dk_x \frac{e^{-k_x|z|}}{k_x} ik_x E_x(k_x, z'=0)e^{ik_x x}$$
$$E_z(k_x, z) = ie^{-k_x|z|}E_x(k_x, z'=0)$$

From $\nabla\times\mathbf{e} = 0$

$$e_i(\mathbf{x}) = \int dS' g(\mathbf{x},\mathbf{x}')\partial_{n'} e_i(\mathbf{x}')\Big|_{z'=0}, \quad g = g_- + g_+$$
$$e_x(\mathbf{x}) = -\int dS' g(\mathbf{x},\mathbf{x}')\partial_{z'} e_x(\mathbf{x}') = \int dS' g(\mathbf{x},\mathbf{x}')\partial_x e_z(\mathbf{x}')$$
$$e_x(\mathbf{x}) = \int dx' \frac{1}{2\pi}\int dk_x \frac{e^{-k_x|z-z'|}}{k_x}\Bigg|_{z'=dz/2} e^{ik_x(x-x')}\frac{1}{2\pi}\int dk_x' ik_x' E_z(k_x', z'=dz/2)e^{ik_x' x'}$$
$$\frac{1}{2\pi}\int dk_x E_x(k_x, z)e^{ik_x x} = \frac{1}{2\pi}\int dk_x \frac{e^{-k_x|z-dz/2|}}{k_x} ik_x E_z(k_x, z'=dz/2)e^{ik_x x}$$
$$E_x(k_x, z) = ie^{-k_x|z-dz/2|}E_z(k_x, z'=dz/2)$$

From $(\nabla\times\mathbf{h}) = 0, (\nabla\times\mathbf{h})_x = -\partial_z h_y, (\nabla\times\mathbf{h})_z = \partial_x h_y$ adding we get
$(\nabla\times\mathbf{h})_x + (\nabla\times\mathbf{h})_z = -\partial_z h_y + \partial_x h_y \Rightarrow \partial_z h_y = \partial_x h_y$ in air

$$h_i(\mathbf{x}) = \int dS' g(\mathbf{x},\mathbf{x}')\partial_{n'} h_i(\mathbf{x}')\Big|_{z'=0}, \quad g = g_- + g_+$$
$$h_y(\mathbf{x}) = -\int dS' g(\mathbf{x},\mathbf{x}')\partial_{z'} h_y(\mathbf{x}') = -\int dS' g(\mathbf{x},\mathbf{x}')\partial_x h_y(\mathbf{x}')$$
$$h_y(\mathbf{x}) = -\int dx' \frac{1}{2\pi}\int dk_x \frac{e^{-k_x|z-z'|}}{k_x}\Bigg|_{z'=dz/2} e^{ik_x(x-x')}\frac{1}{2\pi}\int dk_x' ik_x' H_y(k_x', z'=dz/2)e^{ik_x' x'}$$
$$\frac{1}{2\pi}\int dk_x H_y(k_x, z)e^{ik_x x} = -\frac{1}{2\pi}\int dk_x \frac{e^{-k_x|z-dz/2|}}{k_x} ik_x H_y(k_x, z'=dz/2)e^{ik_x x}$$
$$H_y(k_x, z) = -ie^{-k_x|z-dz/2|}H_y(k_x, z'=dz/2)$$

Let $g = g_- - g_+$, then

$$g(x,x')\big|_{z'=0} = \frac{1}{2}\left[g_-(x,x') - g_+(x,x')\right]\Big|_{z'=0} = 0$$

$$\partial_{n'} g(x,x')\big|_{z'=0} = -\partial_{z'} g(x,x')\big|_{z'=0} = \frac{1}{2}\left[-\frac{(z'-z)}{R_-^3} + \frac{(z'+z)}{R_+^3}\right]\Bigg|_{z'=0}$$

$$= \frac{z}{R^3}$$

$$R = \sqrt{(x-x')^2 + z^2}$$

$$G = \frac{e^{-k_x|z-z'|}}{k_x}$$

$$g = \frac{1}{2\pi}\int dk_x \frac{e^{-k_x|z-z'|}}{k_x} e^{ik_x(x-x')}$$

$$G(k_x,z,z') = \int dx g(x,x';z,z') e^{-ik_x(x-x')} = \int dx \frac{1}{2\pi}\int dk_x' \frac{e^{-k_x'|z-z'|}}{k_x'} e^{ik_x'(x-x')} e^{-ik_x(x-x')}$$

$$= \frac{e^{-k_x|z-z'|}}{k_x}$$

$$G(k_x,z,z') = \frac{e^{-k_x|z-z'|}}{k_x}$$

$$g(x,z,z') = \frac{1}{2\pi}\int dk_x \frac{e^{-k_x|z-z'|}}{k_x} e^{ik_x x}$$

$$\partial_{n'} g(x,z,z') = -\partial_{z'} g(x,z,z') = -\frac{1}{2\pi}\int dk_x \frac{1}{k_x}\frac{\partial\left[e^{-k_x|z-z'|}\right]}{\partial|z-z'|}\frac{\partial|z-z'|}{\partial z'} e^{ik_x x}$$

$$= \frac{1}{2\pi}\int dk_x e^{-k_x|z-z'|}\frac{(-)(z-z')}{\sqrt{(z-z')^2}} e^{ik_x x} = -\frac{1}{2\pi}\int dk_x e^{-k_x|z-z'|} e^{ik_x x}$$

$$G(k_x,k_y,z-z') = \frac{1}{2\pi}\int_{-\infty}^{\infty} dk_z \frac{e^{ik_z z}}{k_x^2 + k_y^2 + k_z^2} = \frac{e^{-u|z-z'|}}{2u}$$

$$u = \sqrt{k_x^2 + k_y^2}$$

$$g(x,y,z,z') = \frac{1}{(2\pi)^2}\int_{-\infty}^{\infty} dk_x \int_{-\infty}^{\infty} dk_y \frac{e^{-u|z-z'|}}{2u} e^{i(k_x x + k_y y)}$$

$$g(x,z,z') = \frac{1}{2\pi}\int dk_x \frac{e^{-k_x|z-z'|}}{k_x} e^{ik_x x}$$

$$\partial_x\partial_x g + \partial_z\partial_z g = \frac{1}{2\pi}\int dk_x \left[\frac{-k_x^2}{k_x} e^{-k_x|z-z'|} + \frac{1}{k_x}\frac{\partial}{\partial z}\left(\frac{\partial e^{-k_x|z-z'|}}{\partial|z-z'|} \right) \frac{\partial|z-z'|}{\partial z} \right] e^{ik_x x}$$

$$= \frac{1}{2\pi}\int dk_x \left[-k_x e^{-k_x|z-z'|} - \frac{\partial}{\partial z}\left(\frac{z-z'}{\sqrt{(z-z')^2}} e^{-k_x|z-z'|} \right) \right] e^{ik_x x}$$

$$= \frac{1}{2\pi}\int dk_x \left[-k_x + k_x \right] e^{-k_x|z-z'|} e^{ik_x x} = 0,\ x \neq 0\ z \neq z'$$

$$z = z', x = 0$$

$$\partial_x\partial_x g + \partial_z\partial_z g = \frac{1}{2\pi}\int dk_x (-k_k) \to -\infty$$

$$\partial_x\partial_x g + \partial_z\partial_z g = -\delta(x)\delta(z-z')$$

$$g(x,z,z') = \frac{1}{2\pi}\int dk_x \frac{e^{-k_x|z-z'|}}{k_x} e^{ik_x x}$$

$$\partial_{n'} g(x,z,z') = -\partial_{z'} g(x,z,z') = \frac{1}{2\pi}\int dk_x e^{-k_x|z-z'|} e^{ik_x x}$$

$$f(x,z) = \int dx' f(x', z'=0)\partial_{z'} g(x,z,z')$$

$$= \int dx' \frac{1}{(2\pi)^2}\int dk_x \int dk_x' F(k_x z'=0) e^{ik_x x} e^{-k_x'|z-z'|} e^{ik_x' x}$$

$$f(x,z) = \frac{1}{2\pi}\int dk_x F(k_x z'=0) e^{-k_x|z|}$$

Appendix D

Field notes

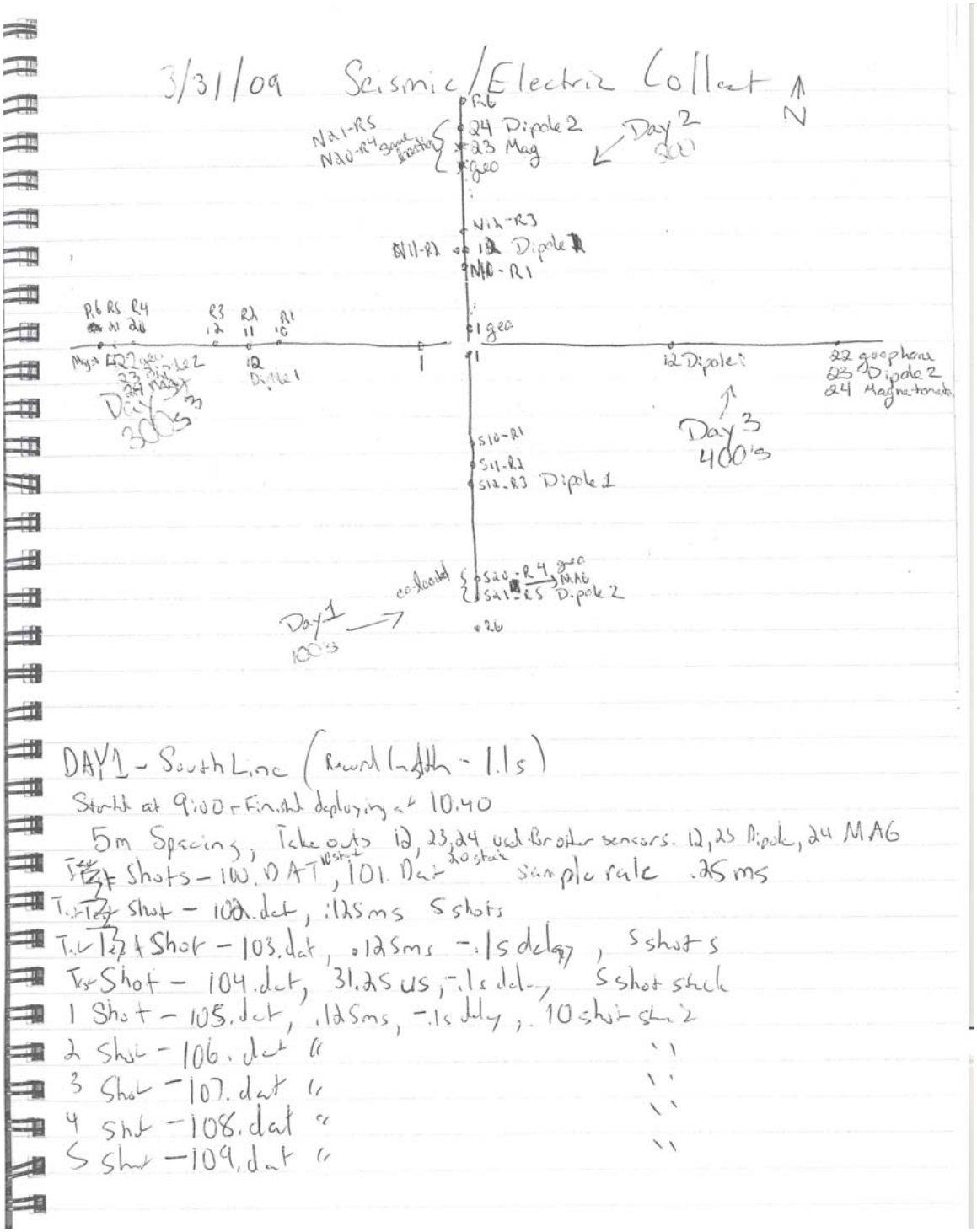

3 shots [illegible] Plate prior to recording

South Line Tomography Curves

Shot 1 - between geophones 2/3 @ 7.5m - 110.dat
Shot 2 - " 4/5 @ 17.5m - 111.dat
Shot 3 - " 6/7 @ 27.5m - 112.dat
Shot 4 - " 8/9 @ 37.5m - 113.dat
Shot 5 - " 10/11/12 @ 47.5m - 114.dat
Shot 6 - " 13/14 ~~12/13~~ @ 57.5m - 115.dat truck upslope weight start
Shot 7 - " 15/16 ~~14/15~~ @ 67.5m - 116.dat winds picking up again
Shot 8 - " 17/18 ~~16/17~~ @ 77.5m - 117.dat
Shot 9 - " 19/20 ~~18/19~~ @ 87.5m - 118.dat
Shot 10 - " 21/22 ~~20/21~~ @ 97.5m - 119.dat Truck approached on 1 of 10 stacks
Shot 11 - " 22 ~~21+~~ off end @ 107.5m - 120.dat
Shot 12 - " 22 ~~21++~~ off end @ 117.5m - 121.dat

Noise Data 8.192s 0 122 Trigger Delay = 0s
" 123 "
" 124 "

Day 2 North Line

Same setup as South Line, 5m spacing 12, 23, 34 not gros, -12, 24 dipoles 23, 1kg
start at 8:30am finished deployment at 9:45am

1) 201.dat single stack data to look at dipoles
2) 202.dat " "
3) 203.dat " " Change geophone @ channel "
1) 204.dat " "
2) 205.dat " "
3) 206.dat " "

winds picking up to 15-20 mph

1) 207.dat 10 stacks in each file -0.1s delay, 1.1s record length 0.125ms sample rate "
2) 208.dat " "
3) 209.dat " "
4) 210.dat " "
5) 211.dat " "

North Line Tomography Survey

Shot 1 - between geophones 2/3 @ 7.5m - 212.dat

Shot 2 - " 4/5 @ 17.5m - 213.dat on incline, less force

Shot 3 - " 6/7 @ 27.5m - 214.dat

Shot 4 - " 8/9 @ 37.5m - 215.dat

Shot 5 - " 10/11 @ 47.5m - 216.dat

Shot 6 - " 13/14 ~~12/13~~ @ 57.5m - 217.dat

Shot 7 - " 15/16 @ 67.5m - 218.dat

Shot 8 - " 17/18 @ 77.5m - 219.dat wires pickel up more

Shot 9 - " 19/20 @ 87.5m - 220.dat

Shot 10 - " 21/22 @ 97.5m - 221.dat

Shot 11 - " 22+ off end @ 107.5m - 222.dat

Shot 12 - " 22++ off end @ 117.5m - 223.dat

Day 3 West Line

Same set up as N-S line, 5m spacing, channel 12 & 24 are dipoles
channel 23 is magnetometer; started deployment at 8:45 finished 9:45
sunny and slight breeze, no clouds

1) 301.dat single stack data to look at dipoles
2) 302.dat " "
3) 303.dat " "
4) 304.dat " "
5) 305.dat " "
6) 306.dat " "
1) 307.dat 10 stacks in each file, -0.1 trigger delay, 1.1s record length 0.125m sampling rate
2) 308.dat " "
3) 309.dat " "
4) 310.dat " "
5) 311.dat " "

West Line Tomogram

Shot 1 - between geophones 2/3 @ 7.5m - 312.dat
Shot 2 - " 4/5 @ 17.5m - 313.dat
Shot 3 - " 6/7 @ 27.5m - 314.dat
Shot 4 - " 8/9 @ 37.5m - 315.dat
Shot 5 - " 10/11/12 @ 47.5m - 316.dat
Shot 6 - " 13/14 @ 57.5m - 317.dat
Shot 7 - " 15/16 @ 67.5m - 318.dat
Shot 8 - " 17/18 @ 77.5m - 319.dat
Shot 9 - " 19/20 @ 87.5m - 320.dat /Shut for lunch (battery) Start ~12:30
Shot 10 - " 21/22 @ 97.5m - 321.dat 707 overhead SW slight loading wind picking up
Shot 11 - " 22+ @ 107.5m - 322.dat
Shot 12 - " 22++ @ 117.5m - 323dat

East Line

same parameters as previous

Appendix E

Weather Data

This appendix provides detailed weather conditions on the days data were collected. This weather information is from station C0082, near the field acquisition site but outside Tijeras canyon. All weather-related information contained in was found at http://raws.wrh.noaa.gov/cgi-bin/roman/meso_base.cgi?stn=C0082.

Table 1: Location information about weather station C0082.

ID: C0082	**COUNTY:** Bernalillo
NAME: CW0082 Albuquerque	**STATE:** NEW MEXICO
LATITUDE: 35.0465	**COUNTRY:** US
LONGITUDE: -106.4921	**TIMEZONE:** Mountain
ELEVATION: 5801 ft	**CWA:** ABQ
MNET: APRSWXNET/CWOP	**NWS ZONE:** NM009 Middle Rio Grande Valley/Albuquerque Metro Area
	NWS FIRE ZONE: ABQ106
	GACC: SWCC Southwest
	SUBGACC: SWA PSA-11
	MESOWEST INSERT DATE: 2003-09-10
	LAST CHANGED: 2007-10-28
	WMO or other ID: 9999999

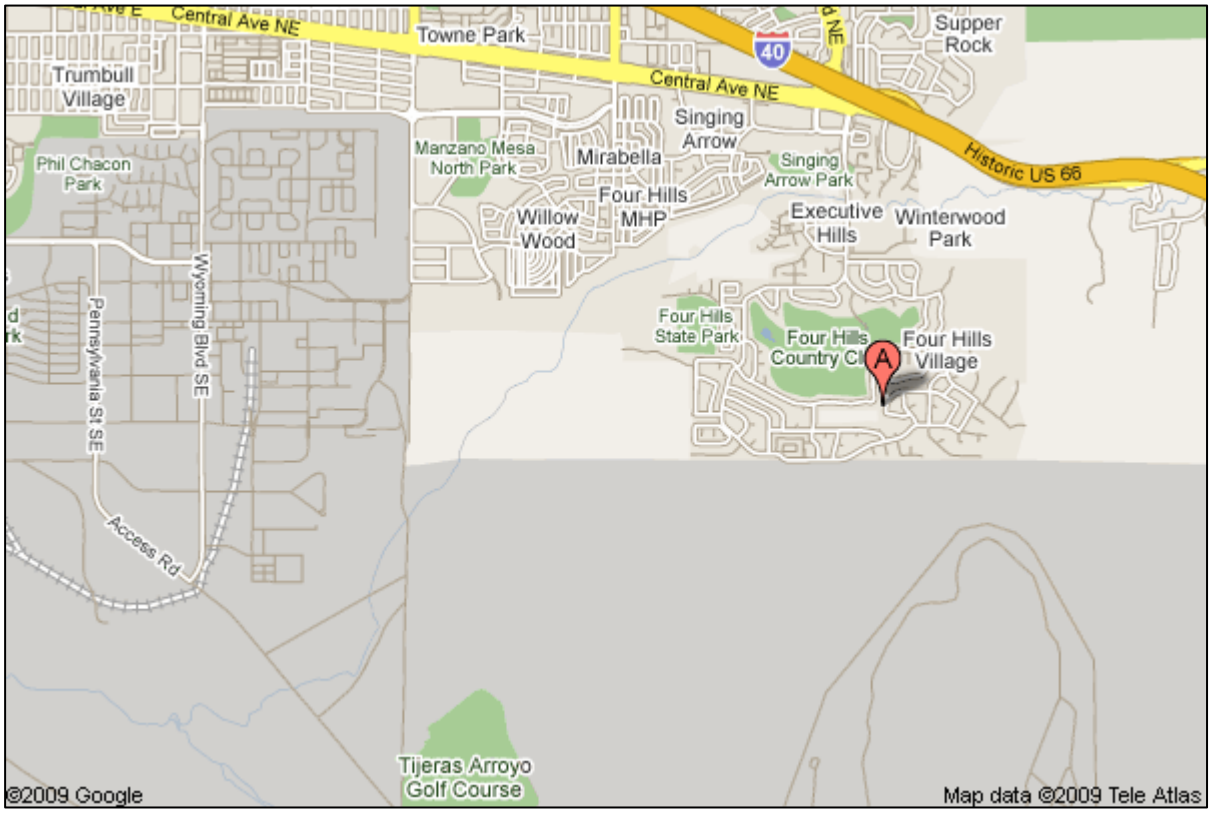

Figure 1: Map indicating location of weather station C0082 (red marker "A") relative to the study site (unmarked).

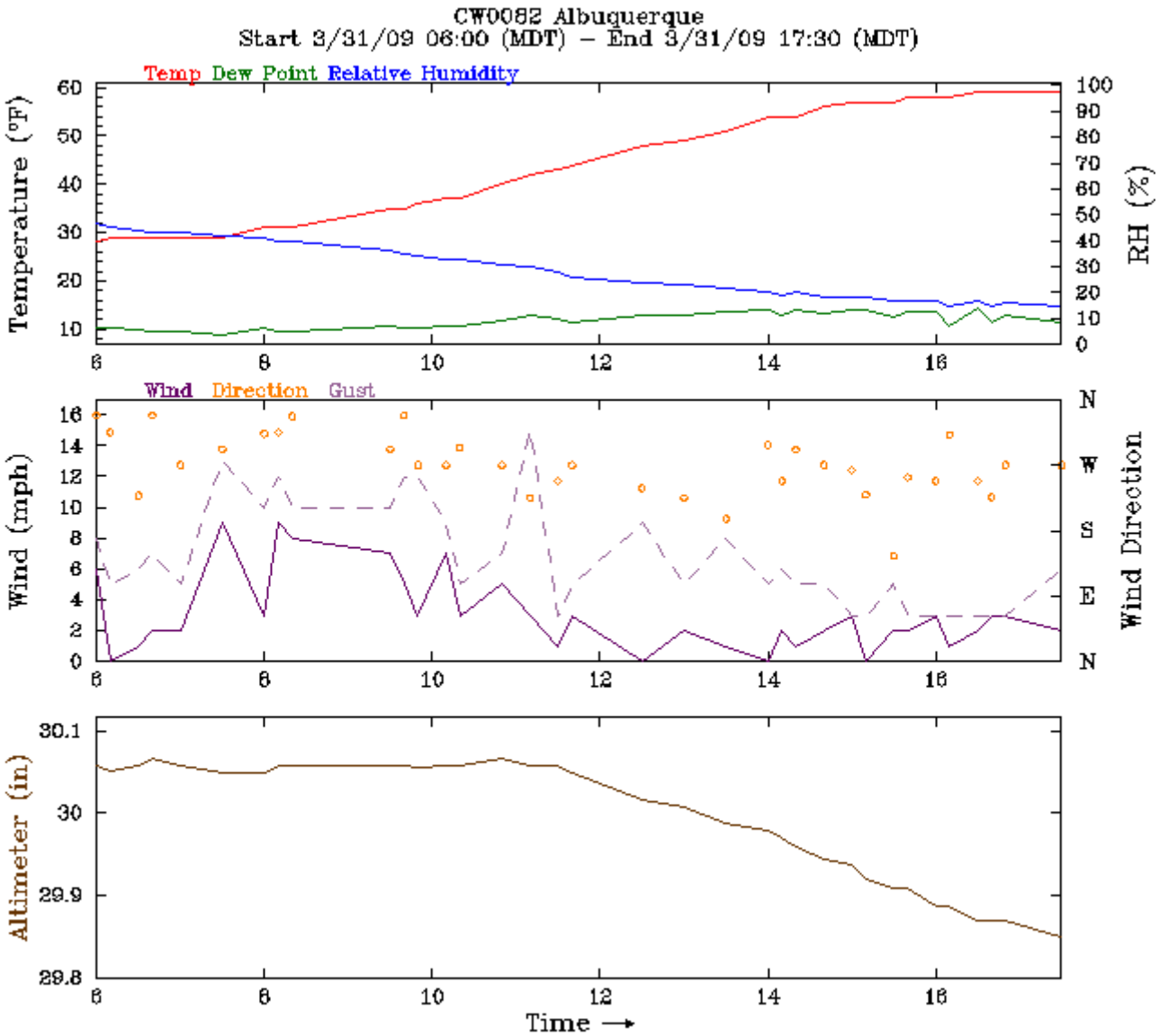

Most Recent Observations at March 31, 2009 - 16:50 MDT

	16:50	Max since Midnight	Min since Midnight	24 Hour Max	24 Hour Min
Temperature	59.0° F	59.0 at 16:30	24.0 at 4:30	59.0 at 16:30	24.0 at 4:30
Dew Point	12.9° F	14.3 at 16:30	6.7 at 4:30	14.3 at 16:30	4.5 at 21:00
Relative Humidity	16%	48 at 5:00	15 at 16:10	48 at 5:00	15 at 16:10
Wind Speed	3 mph from W	9 at 7:30	0 at 0:10	14 at 20:00	0 at 21:30
Wind Gust	3 mph	15 at 11:10	0 at 2:10	17 at 18:00	0 at 2:10
Pressure	24.11 in	24.27 at 6:40	24.11 at 16:30	24.27 at 6:40	24.11 at 16:30

Sea Level Pressure	29.61 in	30.22 at 5:10	29.61 at 16:30	30.22 at 5:10	29.61 at 16:30
Altimeter	29.87 in	30.07 at 6:40	29.87 at 16:30	30.07 at 6:40	29.87 at 16:30

Tabular Listing: March 30, 2009 - 16:37 through March 31, 2009 - 17:37 MDT

Time(MDT)	Temperature ° F	Dew Point ° F	Relative Humidity %	Wind Speed mph	Wind Gust mph	Wind Direction	Quality check	Pressure in	Sea Level Pressure in	Altimeter in	Precipitation 24hr in
16:50	59	12.9	16	3	3	W	OK	24.11	29.61	29.87	0
16:40	59	11.4	15	3	3	SW	OK	24.11	29.61	29.87	0
16:30	59	14.3	17	2	3	WSW	OK	24.11	29.61	29.87	0
16:10	58	10.6	15	1	3	NW	OK	24.13	29.64	29.89	0
16:00	58	13.5	17	3	3	WSW	OK	24.13	29.64	29.89	0
15:40	58	13.5	17	2	3	WSW	OK	24.15	29.66	29.91	0
15:30	57	12.7	17	2	5	SE	OK	24.15	29.67	29.91	0
15:10	57	13.9	18	0	3	SW	OK	24.15	29.68	29.92	0
15:00	57	13.9	18	3	3	W	OK	24.17	29.7	29.94	0
14:40	56	13.1	18	2	5	W	OK	24.17	29.72	29.94	0
14:20	54	13.9	20	1	5	WNW	OK	24.19	29.75	29.96	0
14:10	54	12.7	19	2	6	WSW	OK	24.2	29.77	29.97	0
14:00	54	13.9	20	0	5	WNW	OK	24.2	29.78	29.98	0
13:30	51	13.5	22	1	8	SSW	OK	24.21	29.82	29.99	0
13:00	49	12.9	23	2	5	SW	OK	24.23	29.86	30.01	0
12:30	48	13	24	0	9	WSW	OK	24.23	29.88	30.02	0
11:40	44	11.4	26	3	5	W	OK	24.26	29.97	30.05	0
11:30	43	12.2	28	1	3	WSW	OK	24.27	29.99	30.06	0
11:10	42	12.9	30	3	15	SW	OK	24.27	30	30.06	0
10:50	40	11.9	31	5	7	W	OK	24.27	30.03	30.07	0
10:20	37	10.6	33	3	5	WNW	OK	24.27	30.06	30.06	0
10:10	37	10.6	33	7	9	W	OK	24.27	30.06	30.06	0

9:50	36	10.4	34	3	12	W	OK	24.26	30.07	30.05	0
9:40	35	10.2	35	5	12	NNW	OK	24.27	30.09	30.06	0
9:30	35	10.8	36	7	10	WNW	OK	24.27	30.09	30.06	0
8:20	31	9.6	40	8	10	NNW	OK	24.27	30.14	30.06	0
8:10	31	9.6	40	9	12	NW	OK	24.27	30.14	30.06	0
8:00	31	10.1	41	3	10	NW	OK	24.26	30.13	30.05	0
7:30	29	8.8	42	9	13	WNW	OK	24.26	30.16	30.05	0
7:00	29	9.4	43	2	5	W	OK	24.27	30.17	30.06	0
6:40	29	9.4	43	2	7	NNW	OK	24.27	30.18	30.07	0
6:30	29	9.9	44	1	6	SW	OK	24.27	30.17	30.06	0
6:10	29	10.4	45	0	5	NW	OK	24.26	30.16	30.05	0
6:00	28	10.4	47	6	8	NNW	OK	24.27	30.18	30.06	0
5:40	26	8.6	47	0	0		OK	24.26	30.2	30.05	0
5:30	25	8.1	48	0	1	NNE	OK	24.26	30.21	30.05	0
5:10	24	7.2	48	0	1	S	OK	24.26	30.22	30.05	0
5:00	24	7.2	48	1	1	SSE	OK	24.25	30.21	30.04	0
4:30	24	6.7	47	0	0		OK	24.24	30.2	30.03	0
4:00	25	7.2	46	0	0		OK	24.24	30.19	30.03	0
3:40	26	7.6	45	0	1	SSW	OK	24.23	30.17	30.02	0
3:30	26	7.6	45	0	0		OK	24.23	30.17	30.02	0
3:10	28	9	44	0	6	WSW	OK	24.22	30.12	30	0
3:00	28	9	44	1	2	W	OK	24.22	30.12	30	0
2:40	28	9	44	0	5	NW	OK	24.23	30.13	30.01	0
2:30	27	8	44	4	5	NNW	OK	24.23	30.14	30.01	0
2:10	27	7.5	43	0	0		OK	24.23	30.15	30.02	0
1:40	29	7.8	40	0	3	W	OK	24.23	30.13	30.02	0
1:30	30	8.7	40	1	3	NNW	OK	24.23	30.11	30.02	0
1:10	29	7.2	39	2	2	NNE	OK	24.23	30.12	30.01	0

1:01	29	7.2	39	2	2	NNE	OK	24.23	30.12	30.01	0
0:30	30	7.5	38	2	3	NNW	OK	24.23	30.11	30.02	0
0:10	30	7.5	38	0	7	WNW	OK	24.23	30.11	30.02	0
0:00	30	6.9	37	1	1	NW	OK	24.23	30.11	30.02	0
23:20	31	6.6	35	1	5	W	OK	24.23	30.11	30.01	0
23:10	32	7.5	35	1	5	WSW	OK	24.23	30.08	30.01	0
23:00	32	7.5	35	1	2	WNW	OK	24.22	30.07	30	0
22:20	33	7.1	33	4	7	NW	OK	24.22	30.06	30	0
22:10	33	7.1	33	2	5	NW	OK	24.21	30.05	29.99	0
22:00	33	6.4	32	1	3	NE	OK	24.21	30.04	29.99	0
21:40	34	5.9	30	2	6	W	OK	24.2	30.02	29.98	0
21:30	34	5.9	30	0	3	WSW	OK	24.2	30.02	29.98	0
21:10	35	6	29	5	7	W	OK	24.2	30.01	29.98	0
21:00	35	4.5	27	2	5	NNW	OK	24.2	30.01	29.98	0
20:00	37	6.2	27	14	15	ENE	OK	24.17	29.94	29.94	0
19:20	39	7.1	26	2	6	N	OK	24.16	29.91	29.93	0
19:10	39	7.1	26	5	14	SSE	OK	24.15	29.9	29.92	0
19:00	40	7.9	26	6	14	N	OK	24.15	29.89	29.92	0
18:30	41	9.6	27	13	15	NE	OK	24.15	29.87	29.92	0
18:10	42	9.6	26	5	16	W	OK	24.15	29.85	29.91	0
18:00	42	8.8	25	9	17	WSW	OK	24.15	29.85	29.91	0
17:40	43	9.6	25	3	14	W	OK	24.14	29.83	29.9	0
17:20	43	8.7	24	2	16	W	OK	24.14	29.83	29.9	0
17:10	44	8.6	23	14	16	NNW	OK	24.14	29.82	29.9	0
17:00	44	8.6	23	5	6	SSW	OK	24.14	29.82	29.9	0

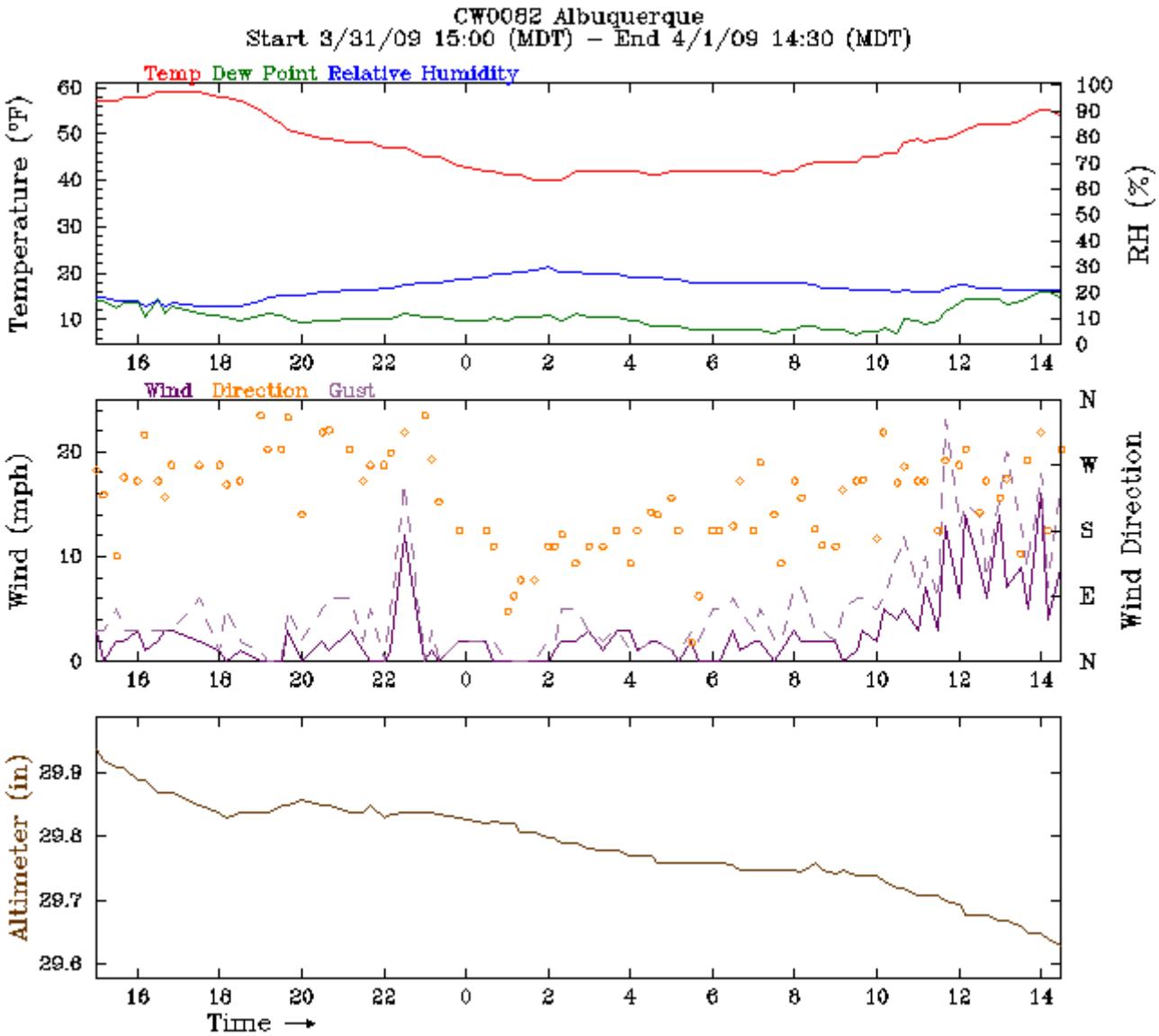

Most Recent Observations at April 1, 2009 - 14:30 MDT

	14:30	Max since Midnight	Min since Midnight	24 Hour Max	24 Hour Min
Temperature	54.0° F	55.0 at 14:00	40.0 at 1:40	59.0 at 16:30	40.0 at 1:40
Dew Point	15.0° F	15.8 at 14:00	6.6 at 9:30	15.8 at 14:00	6.6 at 9:30
Relative Humidity	21%	30 at 2:00	20 at 10:30	30 at 2:00	15 at 16:10
Wind Speed	9 mph from WNW	16 at 14:00	0 at 0:40	16 at 14:00	0 at 15:10
Wind Gust	18 mph	23 at 11:40	0 at 1:01	23 at 11:40	0 at 19:1

					0
Pressure	23.92 in	24.08 at 0:40	23.92 at 14:30	24.17 at 15:00	23.92 at 14:30
Sea Level Pressure	29.42 in	29.77 at 1:40	29.42 at 14:10	29.77 at 1:40	29.42 at 14:10
Altimeter	29.63 in	29.82 at 0:40	29.63 at 14:30	29.94 at 15:00	29.63 at 14:30

Tabular Listing: March 31, 2009 - 13:46 through April 1, 2009 - 14:46 MDT

Time(MDT)	Temperature	Dew Point	Relative Humidity	Wind Speed	Wind Gust	Wind Direction	Quality check	Pressure	Sea Level Pressure	Altimeter	Precipitation 24hr
	° F	° F	%	mph	mph			in	in	in	in
14:30	54	15	21	9	18	WNW	OK	23.92	29.42	29.63	0
14:10	55	15.8	21	4	7	S	OK	23.93	29.42	29.64	0
14:00	55	15.8	21	16	18	NW	OK	23.94	29.43	29.65	0
13:40	54	15	21	5	9	W	OK	23.94	29.45	29.65	0
13:30	53	14.1	21	9	13	SSE	OK	23.95	29.47	29.66	0
13:10	52	13.3	21	7	20	WSW	OK	23.95	29.49	29.67	0
13:00	52	14.4	22	14	16	SW	OK	23.95	29.49	29.67	0
12:40	52	14.4	22	6	8	WSW	OK	23.96	29.5	29.68	0
12:30	52	14.4	22	9	14	SSW	OK	23.96	29.5	29.68	0
12:10	51	14.5	23	14	15	WNW	OK	23.96	29.51	29.68	0
12:00	50	13.7	23	6	13	W	OK	23.97	29.54	29.69	0
11:40	49	11.9	22	13	23	W	OK	23.98	29.56	29.7	0
11:30	49	9.7	20	3	6	S	OK	23.98	29.57	29.71	0
11:10	48	8.9	20	7	10	WSW	OK	23.98	29.58	29.71	0
11:00	49	9.7	20	3	7	WSW	OK	23.98	29.57	29.71	0
10:40	48	10	21	5	12	W	OK	23.99	29.59	29.72	0
10:30	46	7.2	20	4	10	WSW	OK	23.99	29.61	29.72	0
10:10	46	8.3	21	5	6	NW	OK	24	29.63	29.73	0
10:00	45	7.5	21	2	5	S	OK	24.01	29.65	29.74	0

9:40	45	7.5	21	3	6	WSW	OK	24.01	29.65	29.74	0
9:30	44	6.6	21	1	6	WSW	OK	24.01	29.66	29.74	0
9:10	44	7.6	22	0	5	SW	OK	24.02	29.67	29.75	0
9:00	44	7.6	22	2	2	SSE	OK	24.01	29.66	29.74	0
8:40	44	7.6	22	2	3	SSE	OK	24.02	29.67	29.75	0
8:30	44	8.6	23	2	3	S	OK	24.02	29.68	29.76	0
8:10	43	8.7	24	2	7	SW	OK	24.01	29.68	29.75	0
8:00	42	7.9	24	3	7	WSW	OK	24.02	29.69	29.75	0
7:40	42	7.9	24	1	2	SE	OK	24.02	29.69	29.75	0
7:30	41	7	24	0	2	SSW	OK	24.02	29.7	29.75	0
7:10	42	7.9	24	2	5	W	OK	24.02	29.69	29.75	0
7:00	42	7.9	24	2	3	S	OK	24.02	29.69	29.75	0
6:40	42	7.9	24	1	5	WSW	OK	24.02	29.69	29.75	0
6:30	42	7.9	24	3	6	S	OK	24.02	29.7	29.75	0
6:10	42	7.9	24	0	5	S	OK	24.02	29.7	29.76	0
6:00	42	7.9	24	0	5	S	OK	24.02	29.7	29.76	0
5:40	42	7.9	24	0	2	E	OK	24.02	29.7	29.76	0
5:30	42	7.9	24	2	3	NNE	OK	24.02	29.7	29.76	0
5:10	42	8.8	25	0	1	S	OK	24.02	29.7	29.76	0
5:00	42	8.8	25	1	1	SW	OK	24.02	29.7	29.76	0
4:40	41	8.8	26	2	2	SSW	OK	24.02	29.71	29.76	0
4:30	41	8.8	26	2	2	SSW	OK	24.03	29.72	29.77	0
4:10	42	9.6	26	1	1	S	OK	24.03	29.71	29.77	0
4:00	42	9.6	26	3	1	SE	OK	24.03	29.71	29.77	0
3:40	42	10.5	27	3	3	S	OK	24.04	29.72	29.78	0
3:20	42	10.5	27	1	2	SSE	OK	24.04	29.72	29.78	0
3:00	42	10.5	27	3	3	SSE	OK	24.04	29.72	29.78	0
2:40	42	11.3	28	2	5	SE	OK	24.05	29.73	29.79	0

2:20	40	9.6	28	2	5	S	OK	24.05	29.76	29.79	0
2:10	40	10.4	29	1	2	SSE	OK	24.06	29.77	29.8	0
2:00	40	11.1	30	0	2	SSE	OK	24.06	29.76	29.8	0
1:40	40	10.4	29	0	0		OK	24.06	29.77	29.81	0
1:20	41	10.4	28	0	0		OK	24.06	29.76	29.81	0
1:10	41	10.4	28	0	0		OK	24.07	29.77	29.82	0
1:01	41	9.6	27	0	0		OK	24.07	29.77	29.82	0
0:40	42	10.5	27	0	2	SSE	OK	24.08	29.76	29.82	0
0:30	42	9.6	26	2	2	S	OK	24.07	29.76	29.82	0
23:50	43	9.6	25	2	2	S	OK	24.08	29.76	29.83	0
23:20	45	10.4	24	0	0		OK	24.09	29.74	29.83	0
23:10	45	10.4	24	1	3	W	OK	24.09	29.74	29.84	0
23:00	45	10.4	24	0	0		OK	24.09	29.74	29.84	0
22:30	47	11.2	23	12	17	NW	OK	24.09	29.72	29.84	0
22:10	47	10.2	22	1	5	WNW	OK	24.09	29.72	29.83	0
22:00	47	10.2	22	0	0		OK	24.08	29.71	29.83	0
21:40	48	10	21	0	5	W	OK	24.1	29.72	29.85	0
21:30	48	10	21	1	2	WSW	OK	24.09	29.71	29.84	0
21:10	48	10	21	3	6	WNW	OK	24.09	29.71	29.84	0
20:40	49	9.7	20	1	6	NW	OK	24.1	29.71	29.85	0
20:30	49	9.7	20	2	5	NW	OK	24.1	29.71	29.85	0
20:00	50	9.4	19	0	2	SSW	OK	24.1	29.7	29.86	0
19:40	51	10.2	19	3	5	NNW	OK	24.1	29.68	29.85	0
19:30	52	11.1	19	0	0		OK	24.1	29.67	29.85	0
19:10	54	11.5	18	0	0		OK	24.09	29.63	29.84	0
19:00	55	11	17	0	1	NNW	OK	24.09	29.62	29.84	0
18:30	57	9.8	15	1	2	WSW	OK	24.09	29.6	29.84	0
18:10	58	10.6	15	0	5	WSW	OK	24.08	29.58	29.83	0

18:00	58	10.6	15	1	1	W	OK	24.09	29.59	29.84	0
17:30	59	11.4	15	2	6	W	OK	24.1	29.59	29.85	0
16:50	59	12.9	16	3	3	W	OK	24.11	29.61	29.87	0
16:40	59	11.4	15	3	3	SW	OK	24.11	29.61	29.87	0
16:30	59	14.3	17	2	3	WSW	OK	24.11	29.61	29.87	0
16:10	58	10.6	15	1	3	NW	OK	24.13	29.64	29.89	0
16:00	58	13.5	17	3	3	WSW	OK	24.13	29.64	29.89	0
15:40	58	13.5	17	2	3	WSW	OK	24.15	29.66	29.91	0
15:30	57	12.7	17	2	5	SE	OK	24.15	29.67	29.91	0
15:10	57	13.9	18	0	3	SW	OK	24.15	29.68	29.92	0
15:00	57	13.9	18	3	3	W	OK	24.17	29.7	29.94	0
14:40	56	13.1	18	2	5	W	OK	24.17	29.72	29.94	0
14:20	54	13.9	20	1	5	WNW	OK	24.19	29.75	29.96	0
14:10	54	12.7	19	2	6	WSW	OK	24.2	29.77	29.97	0
14:00	54	13.9	20	0	5	WNW	OK	24.2	29.78	29.98	0

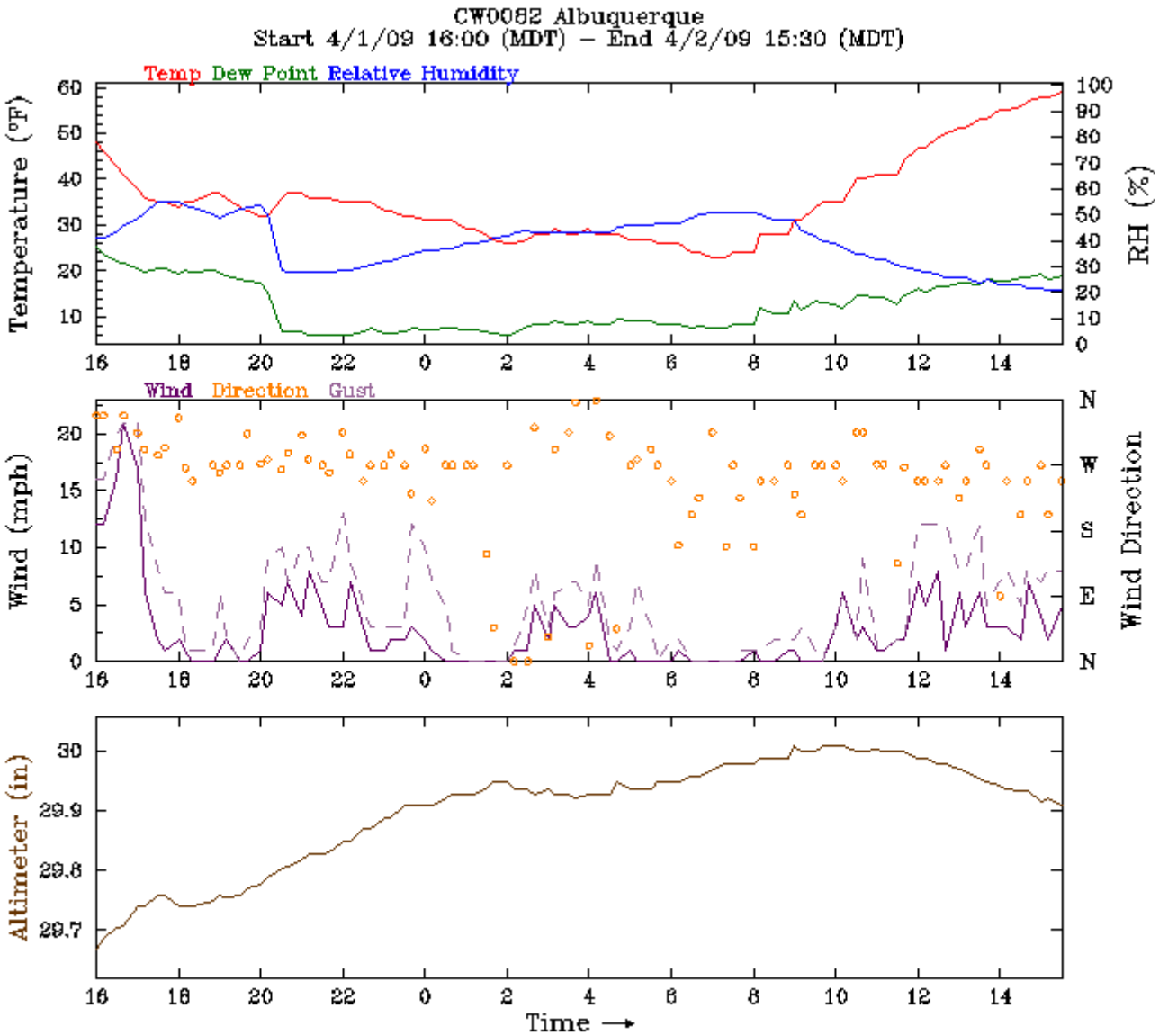

Most Recent Observations at April 2, 2009 - 15:40 MDT

	15:40	Max since Midnight	Min since Midnight	24 Hour Max	24 Hour Min
Temperature	59.0° F	59.0 at 15:30	23.0 at 7:00	59.0 at 15:30	23.0 at 7:00
Dew Point	19.1° F	19.4 at 15:00	6.1 at 2:00	23.7 at 16:10	6.0 at 22:00
Relative Humidity	21%	51 at 7:00	21 at 15:10	55 at 17:30	21 at 15:10
Wind Speed	4 mph from W	8 at 12:30	0 at 0:30	21 at 16:40	0 at 18:20

Wind Gust	6 mph	12 at 12:00	0 at 1:01	21 at 16:40	0 at 19:30
Pressure	24.15 in	24.23 at 9:00	24.15 at 0:00	24.23 at 9:00	23.97 at 16:10
Sea Level Pressure	29.64 in	30.17 at 7:20	29.64 at 15:30	30.17 at 7:20	29.57 at 16:10
Altimeter	29.91 in	30.01 at 9:00	29.91 at 0:00	30.01 at 9:00	29.69 at 16:10

Tabular Listing: April 1, 2009 - 15:01 through April 2, 2009 - 16:01 MDT

Time(MDT)	Temperature ° F	Dew Point ° F	Relative Humidity %	Wind Speed mph	Wind Gust mph	Wind Direction	Quality check	Pressure in	Sea Level Pressure in	Altimeter in	Precipitation 24hr in
15:40	59	19.1	21	4	6	W	OK	24.15	29.64	29.91	0
15:30	59	19.1	21	5	8	WSW	OK	24.15	29.64	29.91	0
15:10	58	18.3	21	2	8	SSW	OK	24.15	29.67	29.92	0
15:00	58	19.4	22	4	7	W	OK	24.15	29.66	29.91	0
14:40	57	18.6	22	7	8	WSW	OK	24.17	29.69	29.93	0
14:30	56	18.8	23	2	5	SSW	OK	24.17	29.71	29.93	0
14:10	55	17.9	23	3	8	WSW	OK	24.17	29.72	29.94	0
14:00	55	17.9	23	3	7	E	OK	24.17	29.73	29.94	0
13:40	53	18.2	25	3	5	W	OK	24.18	29.76	29.95	0
13:30	53	17.2	24	6	12	WNW	OK	24.18	29.76	29.95	0
13:10	51	17.4	26	3	8	WSW	OK	24.19	29.8	29.97	0
13:00	51	17.4	26	6	8	SW	OK	24.2	29.8	29.97	0
12:40	50	16.5	26	1	12	W	OK	24.2	29.82	29.98	0
12:30	49	16.5	27	8	12	WSW	OK	24.2	29.83	29.98	0
12:10	47	15.6	28	5	12	WSW	OK	24.21	29.87	29.99	0
12:00	47	16.4	29	7	12	WSW	OK	24.21	29.87	29.99	0
11:40	44	14.6	30	2	2	W	OK	24.22	29.91	30	0

11:30	41	12.7	31	2	2	SE	OK	24.22	29.95	30	0
11:10	41	14.1	33	1	1	W	OK	24.22	29.95	30	0
11:00	41	14.1	33	1	1	W	OK	24.22	29.96	30	0
10:40	40	14.6	35	3	9	NW	OK	24.22	29.96	30	0
10:30	40	14.6	35	2	2	NW	OK	24.22	29.96	30	0
10:10	35	12	38	6	6	WSW	OK	24.23	30.04	30.01	0
10:00	35	12.6	39	3	3	W	OK	24.23	30.04	30.01	0
9:40	35	13.2	40	0	0		OK	24.23	30.04	30.01	0
9:30	34	13.4	42	0	1	W	OK	24.22	30.04	30	0
9:10	31	11.7	44	0	3	SSW	OK	24.22	30.08	30	0
9:00	31	13.7	48	1	2	SW	OK	24.23	30.09	30.01	0
8:50	28	10.9	48	1	2	W	OK	24.21	30.11	29.99	0
8:30	28	10.9	48	0	2	WSW	OK	24.21	30.11	29.99	0
8:10	28	11.8	50	0	1	WSW	OK	24.21	30.11	29.99	0
8:00	24	8.5	51	1	1	SSE	OK	24.2	30.15	29.98	0
7:40	24	8.5	51	0	1	SW	OK	24.2	30.15	29.98	0
7:30	24	8.5	51	0	0		OK	24.2	30.15	29.98	0
7:20	23	7.6	51	0	0		OK	24.2	30.17	29.98	0
7:00	23	7.6	51	0	0		OK	24.2	30.16	29.97	0
6:40	24	8.1	50	0	0		OK	24.19	30.13	29.96	0
6:30	24	7.7	49	0	0		OK	24.19	30.13	29.96	0
6:10	26	8.6	47	1	2	SSE	OK	24.18	30.1	29.95	0
6:00	26	8.6	47	0	2	WSW	OK	24.18	30.1	29.95	0
5:40	26	8.6	47	0	0		OK	24.18	30.1	29.95	0
5:30	27	9	46	0	3	WNW	OK	24.17	30.07	29.94	0
5:10	27	9	46	0	7	W	OK	24.17	30.07	29.94	0
5:00	27	9	46	1	3	W	OK	24.17	30.07	29.94	0
4:40	28	9.5	45	0	1	NE	OK	24.18	30.07	29.95	0

4:30	28	8.4	43	0	2	NW	OK	24.16	30.05	29.93	0
4:10	28	8.4	43	6	9	N	OK	24.16	30.05	29.93	0
4:00	29	9.4	43	4	5	NNE	OK	24.16	30.04	29.93	0
3:40	28	8.4	43	3	7	N	OK	24.15	30.04	29.92	0
3:30	28	8.4	43	3	7	NW	OK	24.16	30.05	29.93	0
3:10	29	9.4	43	5	6	WNW	OK	24.16	30.04	29.93	0
3:00	28	8.4	43	2	3	NE	OK	24.17	30.06	29.94	0
2:40	28	8.4	43	5	8	NW	OK	24.16	30.05	29.93	0
2:30	27	8	44	1	5	N	OK	24.17	30.07	29.94	0
2:10	26	6.6	43	1	1	N	OK	24.17	30.09	29.94	0
2:00	26	6.1	42	0	0		OK	24.18	30.1	29.95	0
1:40	27	6.5	41	0	0		OK	24.18	30.08	29.95	0
1:30	28	6.9	40	0	0		OK	24.17	30.06	29.94	0
1:10	29	7.2	39	0	0		OK	24.16	30.04	29.93	0
1:01	29	7.2	39	0	0		OK	24.16	30.04	29.93	0
0:40	31	7.8	37	0	1	W	OK	24.16	30.01	29.93	0
0:30	31	7.8	37	0	5	W	OK	24.15	30	29.92	0
0:10	31	7.2	36	1	7	SW	OK	24.15	29.99	29.91	0
0:00	31	7.2	36	2	10	WNW	OK	24.15	29.99	29.91	0
23:40	32	7.5	35	3	12	SW	OK	24.15	29.98	29.91	0
23:30	32	6.9	34	2	3	W	OK	24.15	29.98	29.91	0
23:10	33	6.4	32	2	3	WNW	OK	24.13	29.94	29.89	0
23:00	33	6.4	32	1	3	W	OK	24.13	29.94	29.89	0
22:40	35	7.5	31	1	3	W	OK	24.11	29.9	29.87	0
22:30	35	6.8	30	3	5	WSW	OK	24.11	29.9	29.87	0
22:10	35	6	29	7	9	WNW	OK	24.1	29.88	29.85	0
22:00	35	6	29	3	13	NW	OK	24.1	29.88	29.85	0
21:40	36	6.1	28	3	7	W	OK	24.08	29.85	29.83	0

21:30	36	6.1	28	5	7	W	OK	24.08	29.85	29.83	0
21:10	36	6.1	28	8	10	W	OK	24.08	29.85	29.83	0
21:00	37	7	28	4	10	NW	OK	24.07	29.82	29.82	0
20:40	37	7	28	7	7	WNW	OK	24.06	29.81	29.81	0
20:30	36	6.9	29	5	10	W	OK	24.06	29.82	29.8	0
20:10	32	15.5	50	6	9	W	OK	24.05	29.86	29.79	0
20:00	32	17.3	54	1	3	W	OK	24.04	29.84	29.78	0
19:40	33	17.8	53	0	2	NW	OK	24.03	29.82	29.77	0
19:30	34	18.3	52	0	0		OK	24.02	29.8	29.76	0
19:10	36	19.2	50	2	2	W	OK	24.02	29.77	29.75	0
19:00	37	19.7	49	1	6	W	OK	24.02	29.76	29.76	0
18:50	37	20.1	50	0	1	W	OK	24.02	29.75	29.75	0
18:20	35	19.6	53	0	1	WSW	OK	24.01	29.77	29.74	0
18:10	35	20.1	54	1	1	W	OK	24.01	29.77	29.74	0
18:00	34	19.6	55	2	6	NNW	OK	24.01	29.78	29.74	0
17:40	35	20.5	55	1	6	WNW	OK	24.02	29.78	29.76	0
17:30	35	20.5	55	2	8	WNW	OK	24.02	29.78	29.76	0
17:10	36	19.7	51	6	13	WNW	OK	24.01	29.75	29.74	0
17:00	38	20.6	49	17	21	NW	OK	24.01	29.73	29.74	0
16:40	41	21.8	46	21	21	NNW	OK	23.98	29.66	29.71	0
16:30	43	22.1	43	16	20	WNW	OK	23.98	29.63	29.7	0
16:10	46	23.7	41	12	16	NNW	OK	23.97	29.57	29.69	0
16:00	48	25.5	41	12	16	NNW	OK	23.95	29.53	29.67	0
15:40	52	23.8	33	7	8	NW	OK	23.94	29.47	29.65	0
15:30	54	19.9	26	7	12	W	OK	23.92	29.43	29.63	0
15:10	53	15.2	22	15	17	WSW	OK	23.92	29.43	29.62	0

Appendix F

GPS Coordinates of Source and Sensor Location for Field Experiment

This appendix contains aerial photographs of the survey area with GPS-surveyed positions of all sensor and source locations and details of the GPS data in table format. The East segment of the survey contains sensor locations but no source locations because the sensors were deployed and in place when the AWD source failed. Therefore no data was collected for the East segment of the survey.

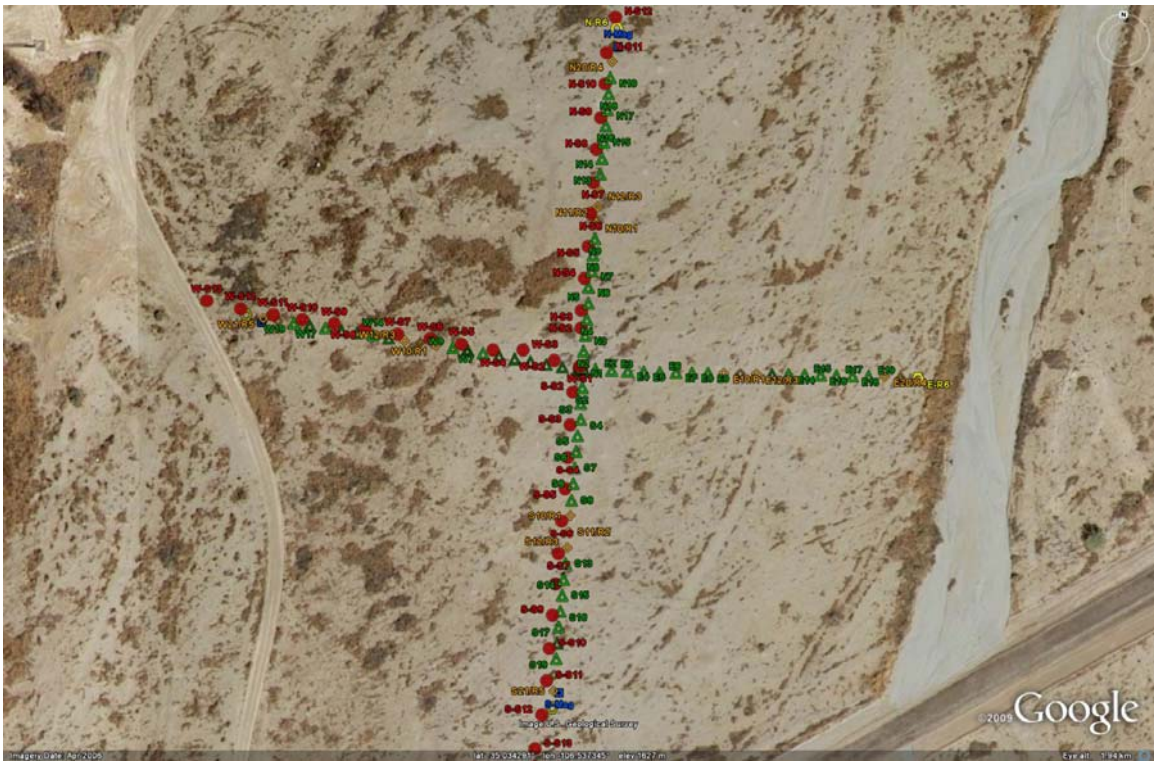

Figure 2: View of all surveyed source and sensor locations on an aerial photograph of the site.

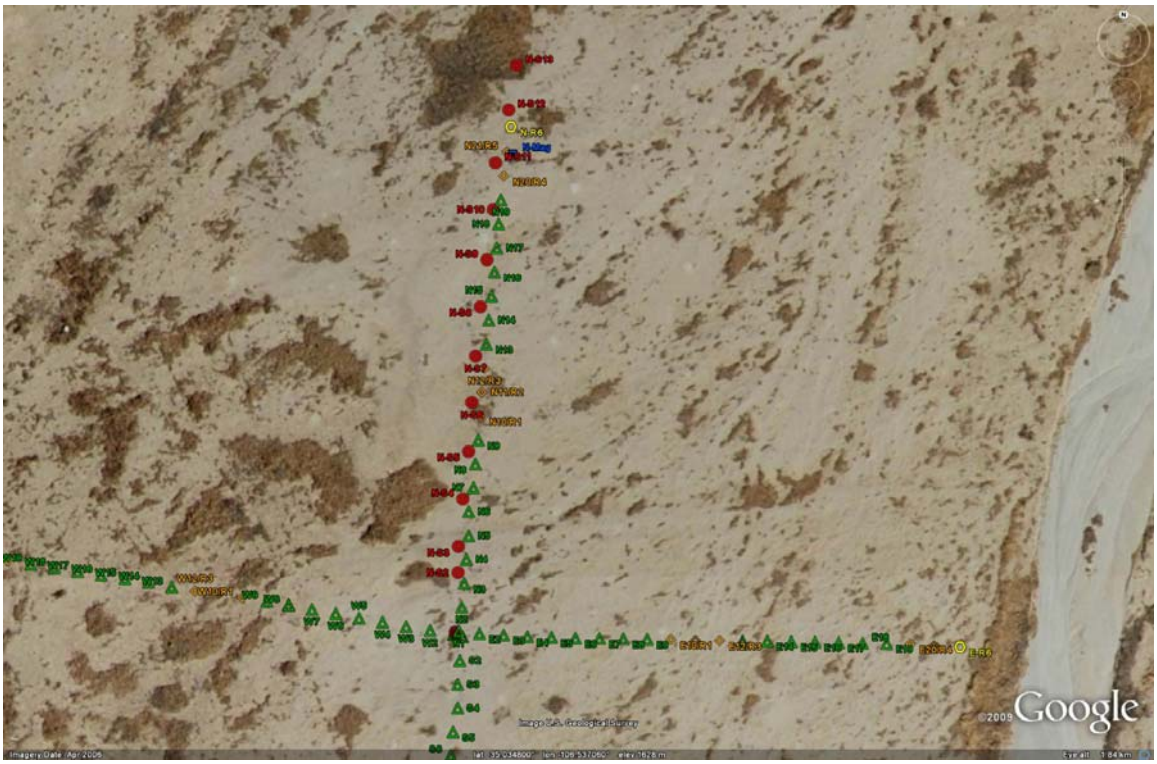

Figure 3: Enlarged view of the surveyed source and sensor locations for the North segment on an aerial photograph of the site.

North Sensor Line Geometrics				
Station #	**Sensor Type**	**Lattitude**	**Longitude**	**Comments**
N1	4.5 Hz Vert Geo.	35.034335234	-106.537333168	
N2	4.5 Hz Vert Geo.	35.034380373	-106.537326713	
N3	4.5 Hz Vert Geo.	35.034424780	-106.537320860	
N4	4.5 Hz Vert Geo.	35.034469730	-106.537315833	
N5	4.5 Hz Vert Geo.	35.034513972	-106.537310362	
N6	4.5 Hz Vert Geo.	35.034559021	-106.537304579	
N7	4.5 Hz Vert Geo.	35.034603811	-106.537299503	
N8	4.5 Hz Vert Geo.	35.034648153	-106.537295024	
N9	4.5 Hz Vert Geo.	35.034692973	-106.537288090	
N10	4.5 Hz Vert Geo.	35.034737526	-106.537283787	
N11	4.5 Hz Vert Geo.	35.034782047	-106.537279873	
N12	4.5 Hz Vert Geo.	35.034826486	-106.537274336	Using takeout 13, takeout 12 used for dipole
N13	4.5 Hz Vert Geo.	35.034871781	-106.537269824	
N14	4.5 Hz Vert Geo.	35.034916471	-106.537264206	
N15	4.5 Hz Vert Geo.	35.034961257	-106.537258061	
N16	4.5 Hz Vert Geo.	35.035006312	-106.537251395	
N17	4.5 Hz Vert Geo.	35.035050768	-106.537246139	
N18	4.5 Hz Vert Geo.	35.035095584	-106.537241679	
N19	4.5 Hz Vert Geo.	35.035140319	-106.537236502	
N20	4.5 Hz Vert Geo.	35.035184775	-106.537230026	
N21	4.5 Hz Vert Geo.	35.035229700	-106.537222924	

North Sensor Line Other Sensors				
Station #	Sensor Type	Lattitude	Longitude	Comments
N-R1	Dipole	35.034737526	-106.537283787	Using takeout 12
N-R2	Dipole	35.034782047	-106.537279873	Using takeout 12
N-R3	Dipole	35.034826486	-106.537274336	Using takeout 12
N-R4	Dipole	35.035184775	-106.537230026	Using takeout 23
N-R5	Dipole	35.035229700	-106.537222924	Using takeout 23
N-R6	Dipole	35.035276610	-106.537213504	Using takeout 23
N-Mag	Magnetometer	35.035226942	-106.537208664	Using takeout 24

North Line Shots			
Shot #	Latitude	Longitude	Comments
N-Shot 1	35.034333092	-106.537341544	
N-Shot 2	35.034444769	-106.537334913	
N-Shot 3	35.034493588	-106.537334132	
N-Shot 4	35.034582491	-106.537323934	
N-Shot 5	35.034671205	-106.537310514	
N-Shot 6	35.034762610	-106.537303140	
N-Shot 7	35.034849053	-106.537294338	
N-Shot 8	35.034941219	-106.537283232	
N-Shot 9	35.035028797	-106.537268444	
N-Shot 10	35.035122402	-106.537253780	
N-Shot 11	35.035209323	-106.537248984	
N-Shot 12	35.035307563	-106.537218757	
N-Shot 13	35.035390594	-106.537201128	

Figure 4: Enlarged view of the surveyed source and sensor locations for the South segment on an aerial photograph of the site.

South Sensor Line Geometrics				
Station #	Sensor Type	Lattitude	Longitude	Comments
S1	4.5 Hz Vert Geo.	35.034324488	-106.537324622	
S2	4.5 Hz Vert Geo.	35.034279546	-106.537331349	
S3	4.5 Hz Vert Geo.	35.034234412	-106.537336323	
S4	4.5 Hz Vert Geo.	35.034190375	-106.537336323	
S5	4.5 Hz Vert Geo.	35.034145424	-106.537347101	
S6	4.5 Hz Vert Geo.	35.034101056	-106.537352350	
S7	4.5 Hz Vert Geo.	35.034054991	-106.537356639	
S8	4.5 Hz Vert Geo.	35.034010945	-106.537361789	
S9	4.5 Hz Vert Geo.	35.033964636	-106.537367715	
S10	4.5 Hz Vert Geo.	35.033921260	-106.537371788	
S11	4.5 Hz Vert Geo.	35.033875344	-106.537378350	
S12	4.5 Hz Vert Geo.	35.033831552	-106.537382386	Using takeout 13, takeout 12 used for dipole
S13	4.5 Hz Vert Geo.	35.033787665	-106.537388170	
S14	4.5 Hz Vert Geo.	35.033742884	-106.537394738	
S15	4.5 Hz Vert Geo.	35.033697873	-106.537399904	

S16	4.5 Hz Vert Geo.	35.033653153	-106.537406460	
S17	4.5 Hz Vert Geo.	35.033609822	-106.537411659	
S18	4.5 Hz Vert Geo.	35.033564187	-106.537416315	
S19	4.5 Hz Vert Geo.	35.033520143	-106.537420226	
S20	4.5 Hz Vert Geo.	35.033474734	-106.537427375	
S21	4.5 Hz Vert Geo.	35.033429979	-106.537429132	

South Sensor Line Other Sensors				
Station #	**Sensor Type**	**Lattitude**	**Longitude**	**Comments**
S-R1	Dipole	35.033921260	-106.537371788	Using takeout 12
S-R2	Dipole	35.033875344	-106.537378350	Using takeout 12
S-R3	Dipole	35.033831552	-106.537382386	Using takeout 12
S-R4	Dipole	35.033474734	-106.537427375	Using takeout 23
S-R5	Dipole	35.033429979	-106.537429132	Using takeout 23
S-R6	Dipole	35.033382529	-106.537434002	Using takeout 23
S-Mag	Magnetometer	35.033426395	-106.537409294	Using takeout 24

South Line Shots			
Shot #	**Latitude**	**Longitude**	**Comments**
S-Shot 1	35.034331099	-106.537334921	
S-Shot 2	35.034266238	-106.537363289	
S-Shot 3	35.034174956	-106.537372179	
S-Shot 4	35.034083363	-106.537380901	
S-Shot 5	35.033996571	-106.537390022	
S-Shot 6	35.033905734	-106.537401654	
S-Shot 7	35.033815266	-106.537412568	
S-Shot 8	35.033729243	-106.537422832	
S-Shot 9	35.033641947	-106.537433251	
S-Shot 10	35.033548752	-106.537444093	
S-Shot 11	35.033458392	-106.537453506	
S-Shot 12	35.033362653	-106.537469932	
S-Shot 13	35.033267090	-106.537492639	

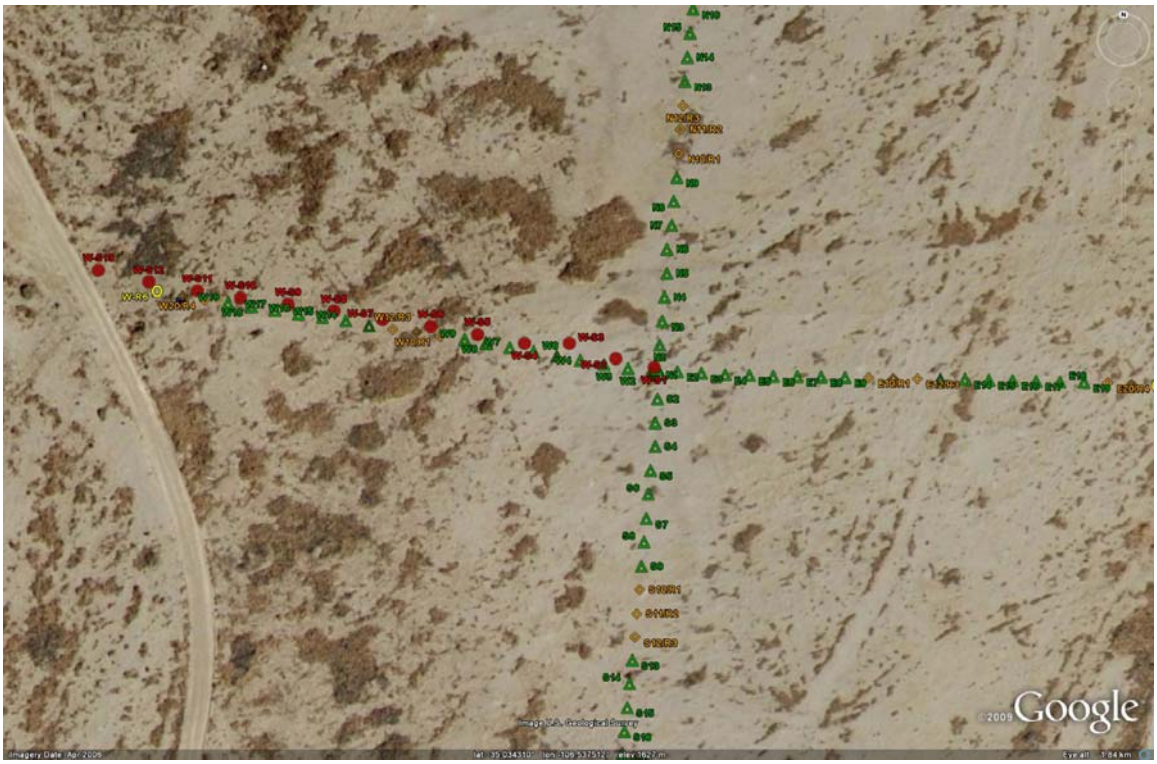

Figure 5: Enlarged view of the surveyed source and sensor locations for the South segment on an aerial photograph of the site.

West Sensor Line Geometrics				
Station #	Sensor Type	Lattitude	Longitude	Comments
W1	4.5 Hz Vert Geo.	35.034328579	-106.537346322	
W2	4.5 Hz Vert Geo.	35.034336302	-106.537398831	
W3	4.5 Hz Vert Geo.	35.034343684	-106.537453661	
W4	4.5 Hz Vert Geo.	35.034351641	-106.537507757	
W5	4.5 Hz Vert Geo.	35.034359319	-106.537561312	
W6	4.5 Hz Vert Geo.	35.034367827	-106.537614634	
W7	4.5 Hz Vert Geo.	35.034375281	-106.537668956	
W8	4.5 Hz Vert Geo.	35.034383580	-106.537722544	
W9	4.5 Hz Vert Geo.	35.034390631	-106.537777211	
W10	4.5 Hz Vert Geo.	35.034397306	-106.537828761	
W11	4.5 Hz Vert Geo.	35.034404704	-106.537882511	
W12	4.5 Hz Vert Geo.	35.034409638	-106.537936956	Using takeout 13, takeout 12 used for dipole
W13	4.5 Hz Vert Geo.	35.034416912	-106.537990744	
W14	4.5 Hz Vert Geo.	35.034425776	-106.538044343	
W15	4.5 Hz Vert Geo.	35.034432336	-106.538098200	

W16	4.5 Hz Vert Geo.	35.034438566	-106.538152778	
W17	4.5 Hz Vert Geo.	35.034445444	-106.538206896	
W18	4.5 Hz Vert Geo.	35.034452433	-106.538260689	
W19	4.5 Hz Vert Geo.	35.034459264	-106.538314997	
W20	4.5 Hz Vert Geo.	35.034465297	-106.538369224	
W21	4.5 Hz Vert Geo.	35.034472476	-106.538419940	

West Sensor Line Other Sensors

Station #	Sensor Type	Lattitude	Longitude	Comments
W-R1	Dipole	35.034397306	-106.537828761	Using takeout 12
W-R2	Dipole	35.034404704	-106.537882511	Using takeout 12
W-R3	Dipole	35.034409638	-106.537936956	Using takeout 12
W-R4	Dipole	35.034465297	-106.538369224	Using takeout 23
W-R5	Dipole	35.034472476	-106.538419940	Using takeout 23
W-R6	Dipole	35.034482051	-106.538478267	Using takeout 23
W-Mag	Magnetometer	35.034462146	-106.538423653	Using takeout 24

West Line Shots

Shot #	Latitude	Longitude	Comments
W-Shot 1	35.034338020	-106.537339250	
W-Shot 2	35.034354647	-106.537426731	
W-Shot 3	35.034369620	-106.537532937	
W-Shot 4	35.034383439	-106.537635345	
W-Shot 5	35.034400058	-106.537742561	
W-Shot 6	35.034414721	-106.537849439	
W-Shot 7	35.034427807	-106.537960790	
W-Shot 8	35.034443943	-106.538071618	
W-Shot 9	35.034456542	-106.538176819	
W-Shot 10	35.034468998	-106.538286157	
W-Shot 11	35.034482238	-106.538385506	
W-Shot 12	35.034499286	-106.538497492	
W-Shot 13	35.034521406	-106.538613044	

East Sensor Line Geometrics

Station #	Sensor Type	Lattitude	Longitude	Comments

E1	4.5 Hz Vert Geo.	35.034328768	-106.537339986	
E2	4.5 Hz Vert Geo.	35.034330316	-106.537286213	
E3	4.5 Hz Vert Geo.	35.034327681	-106.537231184	
E4	4.5 Hz Vert Geo.	35.034324725	-106.537176752	
E5	4.5 Hz Vert Geo.	35.034323318	-106.537121704	
E6	4.5 Hz Vert Geo.	35.034321660	-106.537067154	
E7	4.5 Hz Vert Geo.	35.034321299	-106.537012209	
E8	4.5 Hz Vert Geo.	35.034320451	-106.536957773	
E9	4.5 Hz Vert Geo.	35.034319670	-106.536903086	
E10	4.5 Hz Vert Geo.	35.034319122	-106.536849156	
E11	4.5 Hz Vert Geo.	35.034317440	-106.536793056	
E12	4.5 Hz Vert Geo.	35.034317159	-106.536738091	Using takeout 13, takeout 12 used for dipole
E13	4.5 Hz Vert Geo.	35.034316119	-106.536685375	
E14	4.5 Hz Vert Geo.	35.034316270	-106.536628646	
E15	4.5 Hz Vert Geo.	35.034314582	-106.536573611	
E16	4.5 Hz Vert Geo.	35.034313594	-106.536518947	
E17	4.5 Hz Vert Geo.	35.034312351	-106.536464747	
E18	4.5 Hz Vert Geo.	35.034311083	-106.536409879	
E19	4.5 Hz Vert Geo.	35.034310600	-106.536354742	
E20	4.5 Hz Vert Geo.	35.034309587	-106.536300576	
E21	4.5 Hz Vert Geo.	35.034306560	-106.536245595	

East Sensor Line Other Sensors

Station #	Sensor Type	Lattitude	Longitude	Comments
E-R1	Dipole	35.034319122	-106.536849156	Using takeout 12
E-R2	Dipole	35.034317440	-106.536793056	Using takeout 12
E-R3	Dipole	35.034317159	-106.536738091	Using takeout 12
E-R4	Dipole	35.034309587	-106.536300576	Using takeout 23
E-R5	Dipole	35.034306560	-106.536245595	Using takeout 23
E-R6	Dipole	35.034303701	-106.536185882	Using takeout 23
E-Mag	Magnetometer	NA	NA	Using takeout 24

Distribution List

Sandia National Laboratories

R. E. Abbott	6734
D. F. Aldridge	6734
L. C. Bartel	6734
N. Bonal	6734
G. J. Elbring	6734
B. P. Engler	6734
J. E. Heath	6734
L. Preston	6734
D. J. Borns	6732
P. V. Brady	6730
L. S. Costin	6731
L. Criscenti	6736
R. T. Cygan	6736
R. L. Everett	6735
R. E. Finley	6733
K. N. Gaither	6735
D. J. Holcomb	6735
J. A. Merson	6730
T. Pfeifle	6735
M. J. Rigali	6736
A. R. Sattler	6732

LDRD Office	dchavez@sandia.gov
Technical Library	sanddocs@sandia.gov

Other

Victor F. Labson	USGS